

Doctoral Dissertation (Shinshu University)

**Fabrication of functional micro/nano-carbon composites based on
structural design for electromagnetic shielding**

構造設計による機能性マイクロ・ナノコンポジットの開発および電
磁波遮蔽への応用

September 2019

Yan Yongjie

ABSTRACT

Presently, increasing demand for advanced electromagnetic (EM) shielding devices brought on the development of smart EM shielding materials. In this doctoral research, by using shape memorable polyurethane (SMPU) as supporting matrix, varieties of nano/micro-carbon based composites with different three dimensional structures were designed and fabricated for stimuli-responsive adjustable electromagnetic shielding. These functional shielding composites include thickness-adjustable graphite micro-flakes@SMPU sponge (G@SMPU), vapor grown carbon fiber (VGCF) based polyurethane foam (VGCF@PUF), gradient VGCF based shape memory polyurethane foam (VGCF@SMPUF), and unidirectional nonwoven VGCF based polyurethane fibrous membrane (VGCF@PUFM). Shape memory effect was mainly utilized for thickness fixing and bending actuation of those functional shielding composites.

To better understand the memory effect of SMPU on shape actuation, multi-layer graphene oxide (MLGO) coated shape memory polyurethane (MLGO@SMPU) was fabricated for adjustable shape memory switching devices. The MLGO, which stacked together in parallel, evenly covered the surface of the SMPU. Stress strain testing indicated that the coating of GO improved the mechanical strength of these MLGO@SMPU composites in the stretching stage below the strain of approximately 6 %. Adhesive force testing suggested that the first GO layer could adhere well to the SMPU surface, but the interaction force between GO layers was weak. The angle recovery ratio and time, bending recovery force, and angle fixity ratio of these MLGO@SMPU composites were evaluated using homemade evaluation apparatus. Results indicated that with the increase of GO layers from one to five layers, the MLGO@SMPU gave an angle recovery ratio reduced to 83.2 %, recovery time decreased to 7.6 s, bending recovery force increased to 18.3 mN, and angle fixity ratio decreased to 83.3 %. This novel and straightforward approach of dipping graphene oxide onto shape memory substrates for adjustable recovery ratio, time and force, has the potential to be applied to smart switching devices such as sensors and actuators.

Then, by using shape memory effect as driving force, thickness adjustable graphite (G) micro-flakes@shape memory polyurethane (G@SMPU) sponge was fabricated by two-step dipping separately in G-dispersed aqueous solution and SMPU/THF solution for high-performance microwave shielding. The sponge exhibited an ultrahigh G loading ratio (G/sponge, wt/wt) up to 490 wt.%. For the first time, dipping coating of SMPU onto the sponge was proposed, and the obtained G@SMPU sponge exhibited a good recovery effect at least above 90 % after thorough compression. And also, the thickness could be adjusted by utilizing its shape memory property. For microwave shielding, G-9@SMPU and G-18@SMPU sponges achieved the shielding effectiveness over 20 and 30 dB, respectively. Moreover, varying thickness or compressing repeatedly even up to 100 times would not obviously decrease the shielding effect of

the G@SMPU sponge. This suggests the steady distribution and adhesion of G micro-flakes inside the three-dimensional sponge substrate due to the fixing of SMPU. This shape memory driving thickness-adjustable G@SMPU sponge could be expected for use in compressible electromagnetic shielding devices.

After that, VGCFs having higher electrical conductivity was used as carbon fillers of polyurethane instead of graphite micro-flakes. By way of dipping coating, VGCF based polyurethane foam was fabricated based on H₂O-DMF solvent exchange for compression-adjusted high-performance microwave shielding. The obtained VGCF@PUF specimens with different thicknesses were obtained by hot compression at 120 °C in the pressure range of 0-20 MPa. The tensile test indicated that the hot compression enhanced both the mechanical strength and elongation of the VGCF@PUF. Moreover, with increasing compression, the electrical conductivity of the VGCF@PUF was improved for orders of magnitude. This indicated that the effective inter-connection of VGCFs, achieved by hot compression, is vital for enhancing the electrical conductivity of the VGCF@PUF. In the end, microwave shielding of the VGCF@PUF specimens with different degrees of compression was evaluated by coaxial transmission line method in the frequency range of 0.5-18 GHz. The shielding result showed that increasing compression greatly improved the microwave shielding performance of the VGCF@PUF. For example, the VGCF@PUF specimen with the weight content of approximately 25 %, which had the thicknesses of 1.96 mm and 0.45 mm before and after hot-compression, revealed the difference of shielding effectiveness from 10-15 dB to 35-50 dB. As for the reason, the hot-compression was considered to be able to efficiently improve the electrical inter-connection of the nanoscale carbon fibers in the VGCF@PUF. This research demonstrated the structure optimization of shielding materials is of great importance for improvement of electrical conductivity and microwave shielding performance.

Continually, gradient VGCF based shape memory polyurethane foam (VGCF@SMPUF) was fabricated by alternative dipping in a gradually diluted VGCF@SMPU/DMF solution and distilled water for directional microwave shielding. Shape memory performance for this VGCF@SMPUF was achieved by heat transfer of thermal conductive VGCF. Shielding effectiveness was adjusted through different degrees of angle recovery. A consistent shielding effect from either side indicated that electromagnetic reflection may take place at both the surface and inside of the non-homogeneous composite shield. For shape memory effect, hot compression made VGCF@SMPUF achieve a faster recovery time and higher recovery ratio owing to improved thermal conductivity. Moreover, the VGCF@SMPUF, which was bent to the positive side (PS) with a higher VGCF content, showed shorter recovery time and higher recovery ratio than that bent to the negative side (NS) with a lower VGCF content. We attribute this result to the relatively small mechanical compression strength of the negative side with the lower VGCF content at the bending point when expanding from the positive side. Furthermore, hot compression obviously improved the shielding effectiveness (SE) of the VGCF@SMPUF, mainly through a considerable

increase of the electrical conductivity. The VGCF@SMPUF hot compressed to a thickness of 0.11 mm achieved a SE value of ~30 dB, corresponding to a shielding efficiency of ~99.9 %.

Following with gradient carbon composites, anisotropic structure was designed for direction-dependent EM shielding. In this section, unidirectional nonwoven VGCF based polyurethane (PU) fibrous membrane (VGCF@PUFM) was fabricated by rotation spinning based on DMF-H₂O exchange for directional microwave shielding. This VGCF@PUFM showed obviously different electrical conductivity and mechanical strength in parallel and perpendicular directions. Variational microwave shielding effectiveness (SE) could be observed by changing the crossing angles of VGCF@PUFM with vibrational direction of EM wave. There was the shielding difference more than 10 dB (above 20 dB in 0°, below 8 dB in 90°). Greater shielding effectiveness could be expected by enhancing the anisotropy of electrical conductivity of the VGCF@PUFM. In addition, oriented alignment of VGCF in fibre is promising for further improvement of the electrical conductivity in fibre direction.

In summary, three types of carbon based composite structures, foam structure, gradient structure, and unidirectional structure were successfully designed by using graphite micro-flakes or VGCF as fillers, and SMPU as filling matrix. Shape memory effect played the role of thickness fixing and bending actuation. By varying thickness or angles, the micro/nano-composites showed adjustable EM shielding in the decibel range of 0-40 dB. These functional EM shielding composites with unique structures opened up a new insight for development of smart EM shielding devices.

Table of Contents

1 General introduction	1
1.1 Electromagnetic shielding	2
1.1.1 Background	2
1.1.2 Electromagnetic shielding theory	4
1.1.2.1 Electromagnetic shielding mechanism	4
1.1.2.2 Measurement of shielding effectiveness	8
1.1.2.3 Characterization methods	9
1.1.3 Electromagnetic shielding materials	11
1.1.3.1 Conventional metals	12
1.1.3.2 Conductive polymers	13
1.1.3.3 Carbon nanomaterials	15
1.1.3.4 Electromagnetic shielding composites	17
1.2 Shape memory switches	18
1.2.1 Background	18
1.2.2 Shape memory theory	19
1.2.3 Stimulus-responsive shape memory materials	21
1.2.4 Different ways of shape recovery	23
1.2.5 Shape memory actuation	25
1.3 Purpose, proposal and significance of research	27
1.4 Outline of dissertation	29
References	33
2 Multi-layer graphene oxide coated shape memory polyurethane for adjustable smart switches	49
2.1 Introduction	50
2.2 Experimental	53
2.2.1 Materials	53
2.2.2 Preparation of GO	53
2.2.3 Preparation of SMPU film	54
2.2.4 Fabrication of MLGO@SMPU	54
2.2.5 Characterization	55
2.3 Results and discussion	56
2.3.1 Morphology and structure analysis	56
2.3.2 Mechanical properties	59
2.3.3 Water resistance of GO layer	60

2.3.4 Adhesive properties of GO layer	62
2.3.5 Shape memory recovery	63
2.3.6 Shape memory switching evaluation	65
2.3.7 Angle fixity ratio of shape memory	68
2.4 Conclusionss	69
References	71
3 Graphite micro-flakes and shape memory polyurethane filled sponge for shape memory driving thickness-adjustable microwave shielding.....	77
3.1 Introduction	78
3.2 Experimental	79
3.2.1 Materials	79
3.2.2 Preparation of G@SMPU sponge	79
3.2.3 Characterization and evaluation	80
3.3 Results and discussion.....	80
3.3.1 Morphology and structure	80
3.3.2 Shape memory effect.....	82
3.3.3 Electromagnetic shielding effect	83
3.4 Conclusions	84
References	85
4 Vapor grown carbon fiber structured polyurethane foam for compression adjusted microwave shielding.....	86
4.1 Introduction	87
4.2 Experimental	88
4.2.1 Materials	88
4.2.2 Fabrication of VGCF@PUF.....	89
4.2.3 Characterization	90
4.3 Results and discussion.....	91
4.3.1 VGCF@PUF with different weight contents.....	91
4.3.2 VGCF@PUF with different compression.....	93
4.3.3 Microwave Shielding of VGCF@PUF.....	95
4.4 Conclusions	98
References	100
5 Fabrication of gradient vapor grown carbon fiber based polyurethane foam for shape memory driven microwave shielding	104
5.1 Introduction	105
5.2 Experimental	107
5.2.1 Materials	107

5.2.2 Fabrication of gradient VGCF@SMPUF	107
5.2.3 Characterization	108
5.3 Results and discussion.....	109
5.3.1 Morphology and structure	109
5.3.2 Conductive and mechanical properties.....	111
5.3.3 Microwave shielding based on different angle recovery	112
5.3.4 Microwave shielding with different compression	114
5.3.5 Different recovery efficiency on two sides.....	116
5.3.6 Mechanism for different recovery	118
5.4 Conclusions	120
References	121
6 Aligned nonwoven vapor grown carbon fiber based polyurethane fibrous membrane for direction-dependent microwave shielding	128
6.1 Introduction	129
6.2 Experimental	130
6.2.1 Materials	130
6.2.2 Fabrication of gradient VGCF@SMPUF	130
6.2.3 Characterization	131
6.3 Results and discussion.....	132
6.3.1 Morphology and structure	132
6.3.2 Microwave shielding, conductive and mechanical properties	133
6.3.3 Microwave shielding variation with different anisotropy	134
6.4 Conclusions	136
References	138
7 Conclusions	139
Accomplishments.....	144
Acknowledgements	147

Chapter 1

General introduction

1 General introduction

1.1 Electromagnetic shielding

1.1.1 Background

Over past decades, electromagnetic waves are extremely utilized with rapid development of information industrialization. Electromagnetic wave is transverse in nature, and includes electric and magnetic fields at the same time [1]. The wave propagates with the two fields perpendicular to each other, as illustrated in **Fig. 1.1**. At present, broad electromagnetic waves ranging from radio wave to gamma rays have been well used in various fields such as in wireless communication, navigation, household appliances, and medical instruments [2]. However, lots of electromagnetic radiation also caused some problems such as human health, electromagnetic interference (EMI) and leakage.

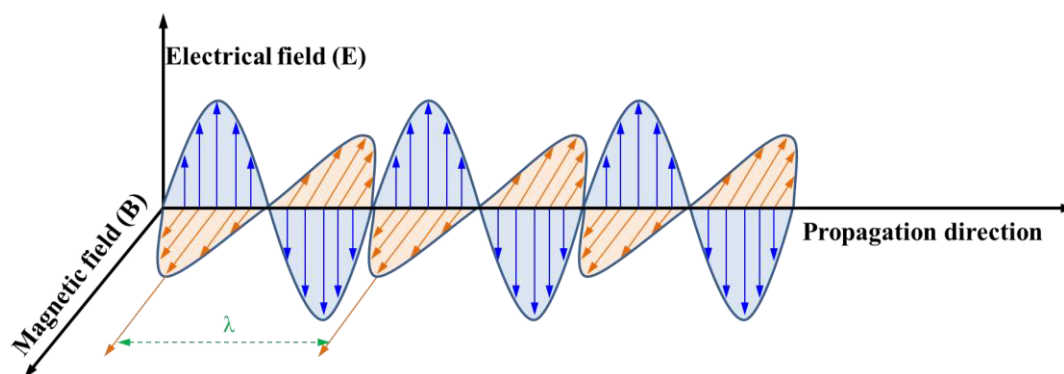


Fig. 1.1 Structure of electromagnetic wave.

In recent years, lots of use of electromagnetic devices has made human and other creatures exposed in an electromagnetic wave-filled environment. Particularly, radio and microwave equipments are frequently used in our everyday life [3]. Nervous systems of creatures have relatively high sensitivity to radio and microwave. Long-term exposure would possibly lead to some chronic diseases related to nervous and cardiovascular systems [4]. In addition,

electromagnetic interference (EMI) and leakage problems have also been serious issues due to its affection to precise control of electronic devices. Some important industries such as in aerospace fields need every part to work well and not interfered by other internal parts or external devices. Thereby, researches have been attempting to find efficient materials to prevent those electromagnetic radiations.

Up to now, there are mainly two types of materials, electromagnetic shielding and absorption materials, which have been proposed. As illustrated in **Fig. 1.2**, electromagnetic shielding materials try their best to prevent incident wave going out from the other side by reflection (R) and absorption (A), while electromagnetic absorption materials try their best to absorb incident wave by decreasing reflection and transmittance as much as possible [5]. Compared to electromagnetic shielding materials, electromagnetic absorption materials have higher requirement for interaction with electromagnetic wave. It needs to remove electromagnetic wave only by absorption, and both reflection and transmittance should occur as less as possible. Aviation and military field seems to have more demand for this kind of materials. Present electromagnetic absorption materials such as dielectric materials and carbon based materials mainly convert the absorbed electromagnetic wave into heat energy. Thus, other problems could possibly happen to electromagnetic devices especially for heat sensitive electronic components. Therefore, in terms of preventing electromagnetic radiation affecting human health, and interferences of electronic devices, electromagnetic shielding materials seems more direct and efficient. The following part would focus on the introduction of electromagnetic shielding materials.

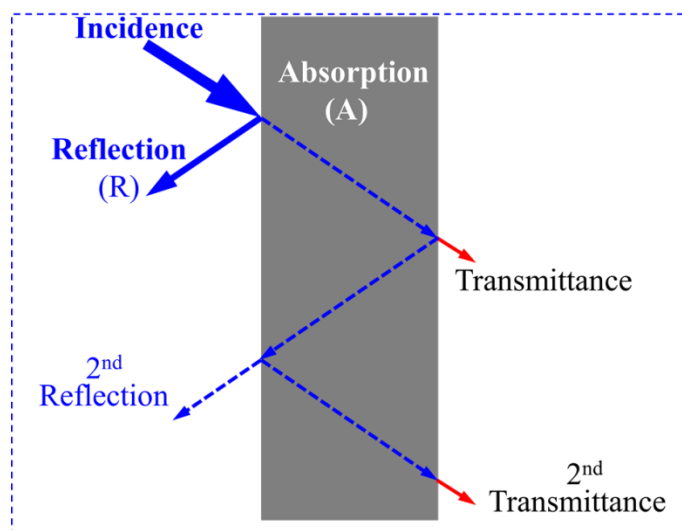


Fig. 1.2 Electromagnetic shielding and absorption.

1.1.2 Electromagnetic shielding theory

1.1.2.1 Electromagnetic shielding mechanism

To develop efficient electromagnetic shielding materials, it is necessary to know the mechanism of electromagnetic shielding. The shielding ability of a shielding material can be expressed by the term electromagnetic shielding effectiveness (SE). SE represents how well a shielding material can block the electromagnetic energy. It is generally accepted that the SE below 10 dB has very little or no shielding effect. From the point view of commercial applications, the SE in 10–30 dB is thought to be the minimum effective range of shielding. $SE \geq 20$ dB can be acceptable for industrial and commercial applications because it attenuates 99% of electromagnetic waves. $SE \geq 30$ dB (a shielding efficiency above 99.9 %) is considered to possess high shielding ability [6].

SE refers to the ratio between incident field energy and transmitted field energy. It can be expressed by **Equations (1-3)**:

$$SE_P = 10 \log P_{in}/P_{out} \quad (1)$$

$$SE_E = 20 \log E_{in}/E_{out} \quad (2)$$

$$SE_H = 20 \log H_{in}/H_{out} \quad (3)$$

where P , E , and H are the power, electric and magnetic intensities of electromagnetic wave, respectively. The subscripts *in* and *out* represent the incidence and transmittance, respectively. Electromagnetic wave impedance is the ratio between the electric field strength and the magnetic field strength. According to the distance (r) of the electromagnetic shielding material from an emitting wave source, the region of measurement can be separated into far-field and near-field region. For far-field region, r is greater than $\lambda/2\pi$ (λ : wavelength), the ratio of the E to H (electromagnetic wave impedance) is equal to the intrinsic impedance of free space ($Z_0 = 377 \Omega$). Thereby, there exist plane wave, and SE_E equals to SE_H . For near-field region r is less than $\lambda/2\pi$. Thus, the electromagnetic wave impedance is not equal to Z_0 . In this measurement region, the electromagnetic wave is either electrical field dominant or magnetic field dominant. This depends on wave source and measurement distance [7].

Schelkunoffs theory is often taken into consideration for electromagnetic shielding. This theory is based on the vertical incidence of plane wave onto an infinite homogenous shielding material. According to the Schelkunoffs theory, total shielding effectness (SE_T) can be defined as the sum of attenuation (loss) of electromagnetic waves. It consists of three shielding mechanisms, reflection (SE_R), absorption (SE_A), and multiple reflections (SE_M) [6], as shown in **Equation (4)**:

$$SE_T = SE_R + SE_A + SE_M \quad (4)$$

1) Reflection loss (SE_R)

Reflection loss (SE_R) is related to the relative impedance mismatching between the surface of the shielding material and the electromagnetic waves. There are different equations to express loss reflection loss, but generally, it is related to conductivity (σ), dielectric properties (ϵ), and

permeability (μ) of the shielding material. One typical equation based on the plane wave under far field conditions is shown as below:

$$SE_R = 10 \log_{10} \left(\frac{\sigma}{16f\epsilon_0\mu} \right) \quad (5)$$

where f and ϵ_0 are frequency and free space permittivity, respectively [5, 6]. What is more, SE_R is recognized to be proportional to the ratio of conductivity and permeability (σ/μ). Consequently, efficient shielding materials are supposed to have mobile charge carriers (electrons or holes) for electromagnetic reflection [8].

2) Absorption loss (SE_A)

Absorption loss (SE_A) does not rely on the type of the used source field. When incident wave goes through a shielding material, the amplitude of the electromagnetic wave reduces exponentially. SE_A mainly results from ohmic loss and dielectric loss. Ohmic loss is because of induced current in the shielding medium, while dielectric loss mostly comes from polarization and relaxation of dielectric materials. These losses result in the heating of the shielding material. For electrically conductive materials, SE_A can be expressed as in **Equation (6)**:

$$SE_A = 20 \log e^{d/\delta} = 8.686d/\delta = 8.686d\sqrt{\pi f\sigma\mu} \quad (6)$$

where d and δ are the thickness and the skin depth of the shielding material, respectively. It can be seen that SE_A is proportional to d , f , σ , and μ of the shielding material [6-9].

As illustrated in **Fig. 1. 3**, when a plane wave penetrates an electrically conductive shielding material, its field strength reduces exponentially with increasing transmittance depth into the conductor [9]. Skin depth represents the attenuation distance at which the field strength becomes equal to $1/e$ or $\sim 37\%$ of its original strength (e refers to Euler's number). For a good conductor (i.e., when $\sigma/2\pi f\epsilon \gg 1$), the skin depth can be expressed by **Equation (7)**:

$$\delta = \sqrt{\frac{1}{\pi f \sigma \mu}} \quad (7)$$

It can be observed from the Equation that the skin depth will vary obviously with respect to conductivity, permeability, and frequency. This indicates that the increase in conductivity, permeability, and frequency will enhance the reflection rather than absorption.

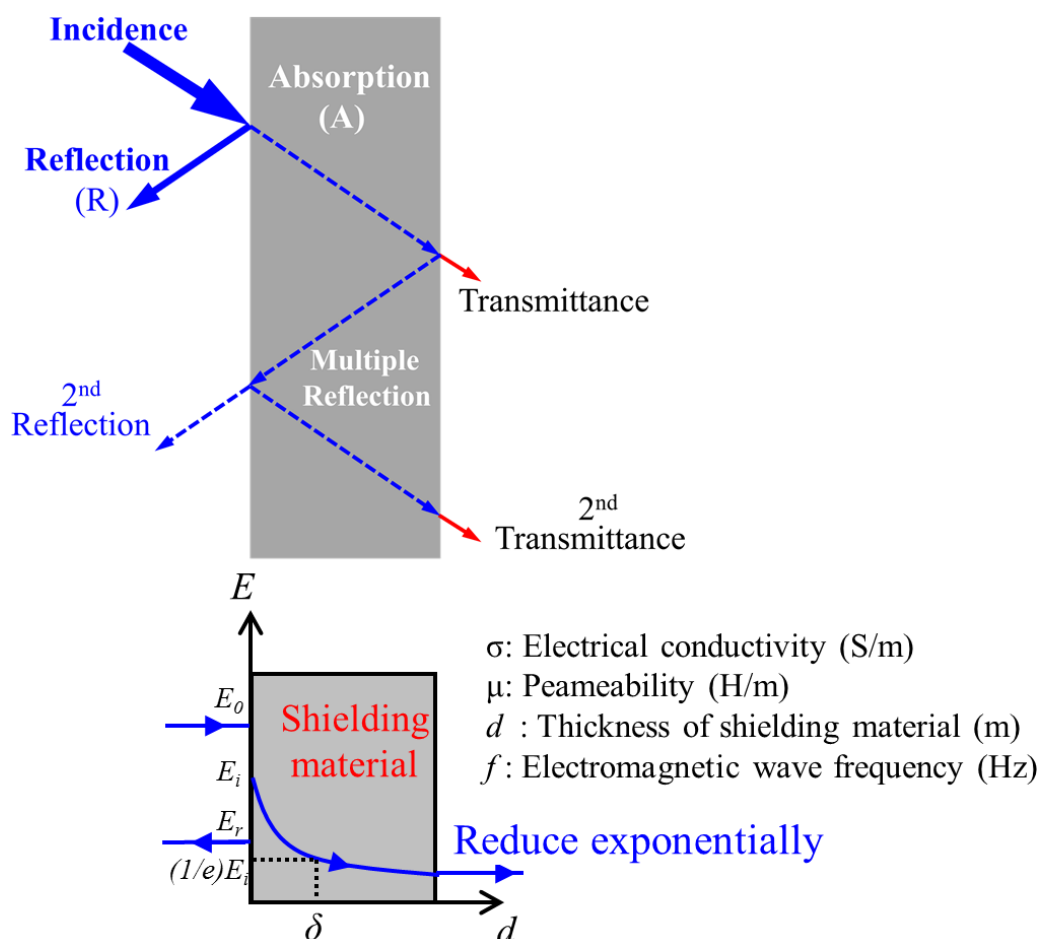


Fig. 1.3 Electromagnetic propagation.

3) Multiple internal reflection (SE_M)

When the transmitted electromagnetic wave reaches the other surface of the shielding material, part of it will get re-reflected, which is called multiple-internal reflection (SE_M), and the other part will get transmitted. The re-reflected wave will bounce again and again between the front and backside (two boundaries) of the shielding material. Especially for thin shielding material, it occurs more easily between the two boundaries. The attenuation which results from these multiple

internal reflections can be mathematically expressed as in **Equation (8)**:

$$SE_M = 20 \log_{10} \left(1 - e^{-\frac{2t}{\sigma}} \right) = 20 \log_{10} \left(1 - e^{-\frac{SE_A}{10}} \right) \quad (8)$$

It can be seen from the **Equation (8)** that SE_M has a close relation with SE_A . SE_M plays an important role in porous structures, composites materials and designed morphologies or geometries. For shielding composites, multiple scattering promotes both absorption and shielding efficiency. However, for thick shielding materials, SE_M can be ignored because the amplitude of the transmitted waves becomes negligible by the time it reaches the other boundary. In other word, SE_M can be considered to be neglected when the shielding material has a high SE_A (i.e., $SE_A \geq 10$ dB). SE_M is important in thin shielding materials or at low electromagnetic band frequencies (i.e., \sim kHz range.). For thick shielding materials with good absorption ability, or for shielding at high frequency (\sim GHz or higher), or simply for shielding materials with $SE_A \geq 10$, neglecting SE_M can be taken into account.

1.1.2.2 Measurement of shielding effectiveness

Electromagnetic shielding effect comes from the surface reflection, internal absorption, and multiple reflection, as illustrated in **Fig. 1.4a**. Shielding effectiveness (SE) can be calculated based on the scattering parameters (S_{11} , S_{22} , S_{12} , S_{21}) of the sample. S_{11} , S_{22} , and S_{12} , S_{21} symbolize the reflection and transmission coefficient data, respectively, as presented in **Fig. 1.4b**.

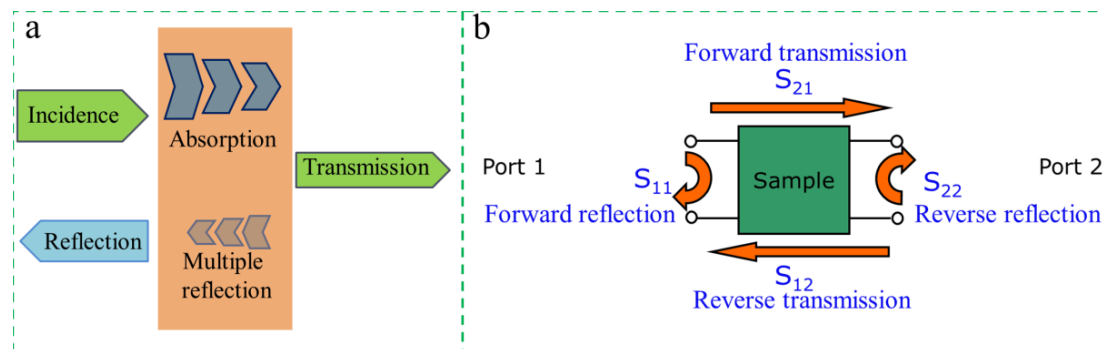


Fig. 1.4 (a) Microwave shielding mechanism; (b) The scattering parameters for microwave.

To evaluate the shielding effectiveness, different shielding contributions are needed to be considered. The power coefficients of reflection (R), transmission (T), and absorption (A) could be determined using the scattering parameters with the following equations:

$$R = |S_{11}|^2 = |S_{22}|^2 \quad (9)$$

$$T = |S_{12}|^2 = |S_{21}|^2 \quad (10)$$

$$R + T + A = 1 \quad (11)$$

Due to the reflection of microwave on the sample surface, effective incident wave entering the material is $(1-R)$. Therefore, the coefficient of effective absorbance (A_{eff}) can be expressed as below:

$$A_{eff} = (1 - R - T)/(1 - R) \quad (12)$$

The total EMI shielding effectiveness (SE) refers to the logarithm of the power ratio of the incident wave, to the transmitted wave. It is composed of absorption (SE_A), reflection (SE_R) and multiple reflection parts (SE_M). In the case of $SE \geq 15$ dB, the multiple reflection part can be neglected, and SE can be simplified as below:

$$SE = SE_R + SE_A + SE_M \approx SE_R + SE_A \quad (13)$$

According to the reflectance and effective absorbance, the SE_R and SE_A can be given by:

$$SE_R = -10 \log(1 - R) \quad (14)$$

$$SE_A = -10 \log(1 - A_{eff}) = -10 \log(T/(1 - R)) \quad (15)$$

1.1.2.3 Characterization methods

At present, there are mainly four methods to measure electromagnetic shielding. They includes Open field method, Shielded box method, Shielded room method, Coaxial transmission line method [10, 11].

1) Open field method

Open field method is also called free space method. It was used to evaluate practical shielding performance of a finished product like an assembly. This method doesn't focus on the measurement of any special material component. It is more partial to true test of finally finished shield. This kind of measurement device should insure there is enough distance from receiving antenna, and record the transmitted electromagnetic wave which escaped from the shielding product.

2) Shielded box method

This method is often used to compare different electromagnetic shielding materials. The shielding sample was tightly fixed in the window part of a metal box in which there is a receiving antenna. Outside this metal box, there is a transmitting antenna. How much is transmitted can be recorded by receiving antenna. For this method, good contact between shielding sample and metal box is difficult to achieve as well as increasing measuring frequency above 500 MHz.

3) Shielded room method

Shielded room method is developed based on shielded box method, and overcame the frequency limitation of shielded box method. The difference with shielded box method is that each components of this measurement system including signal generator, transmitting antenna, receiving antenna and recorder are isolated in separate space to eliminate mutual interference. The measurement frequency could be greatly increased compared with shielded box method.

4) Coaxial transmission line method

Coaxial transmission line method is so far most widely used one. The measurement device mainly comprises vector network analyzer (VNA) for calculation of scattering parameters, coaxial

cables, and metal sample holder. Coaxial transmission cables can generate electromagnetic waves within a wide frequency range. It produces smaller losses compared with conventional antennas. The vector network analyzer can transmit, receive and record electromagnetic intensities. The main advantage of this method is that the shielding result measured from different labs can be used for comparison. Also, the VNA can divide the shielding result into reflected, absorbed and transmitted parts, which provide better understanding for the mechanisms of shielding materials.

1.1.3 Electromagnetic shielding materials

Electromagnetic shielding materials have been given more and more attention because of mutual workspace interferences and human radiation hazard of the electromagnetic waves from electromagnetic devices, such as telephones, televisions, radio transmission equipments and microwave ovens. Lots of natural substances have been tried as shielding materials in which the materials with good electrical conductivity showed satisfied electromagnetic shielding ability. The earliest materials used as electromagnetic shielding materials were metals such as copper (Cu), and aluminum (Al). They exhibited high shielding performance, but some drawbacks such as large density, easy corrosion, and inconvenient processing have limited their applications in advanced electronic products.

Based on those problems, researchers have developed some new types of shielding materials, which mainly include electrically conductive polymers such as polyaniline (PANI) and carbon based materials such as carbon nanotubes (CNTs). Electrically conductive polymers are the products artificially synthesized from small molecules. They show relatively good shielding ability, and can be adjusted in structures and electrical conductivity. Carbon based materials generally present in the form of powder. Their electrical conductivities differ with the change of structures.

The electrical conductivities of those new types of shielding materials are not as good as conventional metals, but their structure and properties can be adjusted. They are considered promising for use in advanced shielding application due to light weight, corrosion resistance, convenient adjustment in structure, and easy processing in production. The following part will introduce the applications of metallic materials, electrically conductive polymers, and carbon based materials in electromagnetic shielding field.

1.1.3.1 Conventional metallic materials

Conventional metallic shielding materials have been well developed over past decades. They could present in the form of bulk sheets, meshes, plating coatings, powders (whiskers, fibers, filaments) in filled polymer composites or coatings. Some typical metals used as shielding materials include silver (Ag), Copper (Cu), aluminum (Al), nickel (Ni), and brass. They have extremely good electrical and thermal conductivities compared with other materials including conductive polymers and carbon powders [11]. This makes them well used in electromagnetic shielding devices. In this way, they can not only act as a shield, but also transfer the heat that the machines on stream generate.

There are also many metal based substances or compounds for use as shielding materials such as alloys, ferrites, and metallic oxides. One typical metallic materials for constructing shield is mumetal, a high permeability alloy with iron (Fe, 14%), (Cu, 5%), chromium (Cr, 1.5%) and (Ni, 79.5%) [6]. In addition, metals can also compound with conductive fillers (i.e., carbon materials) or intrinsically conductive polymers (ICP). There are different approaches to process and utilize metallic materials for use as shielding products. Those various metal based materials can be prepared into board, mesh, or film, or coated onto plastic materials. This depends on different

shielding purposes and applications. Coating onto plastic materials is one common way for using as shielding materials. Up to now, there are different methods to metalize the plastic surface, which mainly include foil laminates and tapes, ion plating, vacuum metallization, cathode sputtering, conductive painting, and electroplating [11].

Conventional metal based shielding materials have been satisfied for using in electromagnetic shielding field. However, they have not been capable of meeting the increasing demand for light and environment-resistant industrial products due to their high densities, dissolution in acid, weak resistance to oxidation. Two main drawbacks of metallic materials, large density and corrosion, have limited their applications in various fields. For example, aerospace applications need the products with light weight and high environment resistance. Therefore, when insuring good shielding performance, electromagnetic shielding materials need to possess other properties to meet various demands in different industrial fields.

1.1.3.2 Conductive polymers

Since electrically conductive polymers were discovered in the late 1970s [12], their electromagnetic shielding abilities have been much investigated [13-20]. Intrinsically conducting polymers (ICPs) are polymers with highly π -conjugated polymeric chains mainly including polyacetylene (PA, 3-1000 S/cm), polyaniline (PANI, 0.01-5 S/cm), polythiophene (PTh, 2-150 S/cm), and polypyrrole (PPY, 0.03-100 S/cm) [9]. They have been attracting much attention for electromagnetic shielding mainly due to their electrical conductivities. Their chemical structures are shown in **Fig. 1.5**. Compared with metals and carbon-based materials, ICPs have good properties such as simple processability, lightweight, strong corrosion resistance and excellent compatibility with other materials. For example, the densities of typical polyaniline and

polypyrrole are 1.1-1.3 g/cm³ and 1.2 g/cm³, respectively [21, 22]. These are much less than that of metals, such as 8.9 g/cm³ of copper [23]. For electromagnetic shielding performance of ICPs, mobile charges (polarons and bipolarons) and bound charges (dipoles) at their back-bone are main mechanisms of shielding. Their electrical conductivity can also be adjusted by governing their oxidation state, doping, chemical structure, and morphology. In addition, electrically conductive polymers show higher electromagnetic absorption ability when compared to reflection dominated metallic shielding materials.

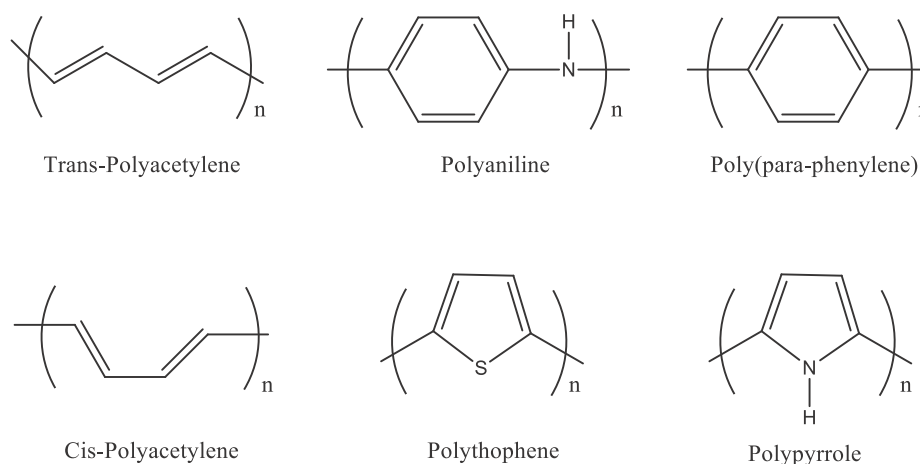


Fig. 1.5 Chemical structure of several common ICPs.

Neutral conjugated polymers usually have low conductivity, but they will be enhanced through chemical or electrochemical redox reactions (so called doping) [24, 25]. The conductivity after doping is highly related to the dopants used as well as the level of doping. This unique feature could make the properties of conductive polymers vary in the range of insulators, semiconductors and conductors. Doping is considered to be a reversible process, and it makes the backbone of conductive polymer change between positive (p-doping) or negative charge carriers (n-doping). For instance, the electrical conductivity of PPy could be increased from 0.1 to 100 S/cm before and after doping, respectively [25].

Doping plays an important role in varying their electrical conductivities. For example, un-doped polymers display poor conducting properties and lie in insulating or semiconducting range (10^{-10} to 10^{-5} S/cm). Controlled doping with suitable dopants can transform poorly conducting PA, PANI, and PPY into semiconducting or metallic conductivity (10^{-6} to 10^5 S/cm) [9]. This feature of conductive polymers is considered promising in controlled electromagnetic shielding field.

1.1.3.3 Carbon materials

Recently, carbon based nano/micro-composites, such as graphene [26-28], carbon nanotubes (CNTs) [29-31], carbon black (CB) [32], graphite [33], and carbon nanofibers (CNFs) [34], have attracted considerable attention for electromagnetic shielding owing to their high specific surface areas, electrical conductivity, and unique one, two, and three dimensional structures [35, 36]. According to different structures, carbon can form various substances such as carbon black (CB), graphite, graphene, carbon nanotube (CNT), fullerene, diamond, and carbon nanofiber (CNF) [37]. At the same time, various structures endow them different electrical conductivities and other properties.

Due to the powder properties of carbon materials, they are usually used by way of coating, or mixed with other materials to form composites. Polymers are recently used as matrix to mix with carbon materials in which graphene, CNT, CB, graphite, CNF are commonly used as carbon fillers. Carbon-based composites can take different forms such as films, foams, nonwoven fabrics, porous materials, and textiles. By compositing with polymers, different applications benefit from additional properties such as being light weight and resistant to environmental corrosion oxidation and having high strength [33-42].

Graphite is most abundantly available material. It has in-plane conductivity in the range of 10^4 S/cm. The common form of graphite based polymer composites is available as inks and coating [6]. CB is generally formed from thermal decomposition of hydrocarbons in gas phase as small particles [5]. In electromagnetic shielding field, the role of CB in carbon/polymers is to increase electrical conductivity. For example, Wang studied the electromagnetic shielding effect of CB/acrylonitrile butadiene styrene (ABS) nanocomposites. The nanocomposite with 35% mass fraction of CB had the electrical conductivity of 9.7×10^3 S/cm, and reached up to 6 dB in 0.2-1.6 GHz [6, 43]. CNF forms from the interlocked sheets having regular hexagonal patterns. It has the diameter in 50–200 nm and the length up to 100 μm .

CNF are often subjected to pre-heat treatment to enhance the electrical conductivity of the nanofiber. Heat treatment can re-arrange carbon planes and remove the amorphous carbon deposited on the surface of the CNF. Thus, its crystallinity and the electrical conductivity could be increased [44]. Compared with other carbon materials such as graphite and CB, CNFs have lower densities. CNFs are usually used as fillers of polymers for electromagnetic shielding. The shielding ability changes with the filling content and composites structures [45-49].

CNTs are considered promising as nano-fillers for various applications. The two major types of CNT having high structural similarity are single-walled carbon nanotubes (SWCNT) and MWCNT. They have higher aspect ratio and smaller diameter when compared with CNF. Thus, CNT based nanocomposites have lower electrical percolation threshold concentration than that of CNF based ones [36]. In other words, the conductive composite based on CNTs can be produced with low loading ratio for satisfaction in different applications. Till to now, there are different approaches to produce CNT, which mainly include laser ablation, arc discharge and chemical

vapor deposition (CVD). Among these processes, CVD is said to be the most promising one because of this approach may allow continuous production of large amount of CNTs at relatively low cost [50, 51]. The electrical conductivity of CNT depends on the purity, size, structure, and chirality. In addition, Multiwall carbon nanotubes (MWCNTs) consist of several concentric cylindrical graphene layers which bonded with each other by Van der Waals forces [52]. The diameter of MWCNT is typically in the range of 5–50 nm [36].

Graphene, since its successful preparation by Andre Geim and Konstantin Novoselov at the University of Manchester in 2004, has undertaken approximately 15 years [53-55]. Graphene is a kind of two dimensional carbon material consisting of a one layer thick hexagonal lattice with one carbon at each vertex, which is thought to be thinnest material in the world. Lots of famous scientists have demonstrated its huge potential application in industry such as solar cells, light-emitting diodes (LED), touch panels, super capacitor, conductive ink, and smart windows or phones due to its strong mechanical property, high electron mobility, high thermal conductivity, and good optical properties. When it comes to electromagnetic shielding, owing to excellent electrical conductivity of graphene, it has great potential to be applied in that shielding field. Some typical approaches for preparing graphene have been developed such as chemical vapor deposition, mechanical and chemical exfoliation. However, there is so far no mature approach for manufacturing graphene (one or a few layers) in an industrial scale.

1.1.3.4 Electromagnetic shielding composites

Over these years, the development of composites has been attracting much attention in various application fields due to tunable structures and compositions. Composites mainly includes the combination (hybrid micro/nano-particles or blend) of different materials in micro/nano or macro

scale, the modification (i.e., filling, coating) of one material (fillers) for the other material (matrix), and the blending or lamination of different materials. Compared with pure materials, more performance can be endowed by different compositing. This is helpful to more practical application. The trend of compositing happens to electromagnetic shielding fielding as well.

Recently, carbon/polymer composites, as an important group of carbon composites, are considered important in the field of electromagnetic shielding because of the rich variety of available natural and synthetic polymers, which can be modified and adjusted for targeted properties [56-62]. There are lots of polymers that are intrinsically non-conducting in nature such as polyurethanes (PU), polyethylene (PE), polyvinyl alcohol (PVA), polyvinylidene fluoride (PVDF), polylactic acid (PLA), polyethyleneimine (PEI). They can be endowed with electrical conductivity by loading different carbon fillers. Currently, graphene, CNF and CNT are mostly used carbon fillers for preparation of carbon/polymer shielding composites. For example, Mohammed and coworkers used acrylonitrile butadiene styrene (ABS) as matrix to mix with different carbon materials (CB, CNF, and CNT), and prepared CB/ABS, CNF/ABS and CNT/ABS nanocomposites [36]. These nanocomposites exhibited better and better shielding performance with increasing carbon loading content in the X-band frequency range. Among them, CNT shows best SE performance under similar loading condition.

1.2 Shape memory materials

1.2.1 Background

Shape memory material is a type of material that can remember its original shape after fixed to another shape by external force. In the past few decades, a variety of shape memory materials have been developed including shape memory polymer (SMP) [63-65], shape memory alloy

(SMA) [66], shape memory ceramic (SMC) [67], shape memory gel (SMG) [68, 69], shape memory foam [70], shape memory fiber [71, 72], and other specific materials. These materials can be fixed to a desired shape by force, and autonomously recovered through external stimulation such as temperature [73], electricity [74], light [75], pH [76], solvent [77], magnetic field [78], compression [79], and water [80]. This flexible performance has resulted in application of shape memory materials in many industrial fields including sensors, actuators, smart devices, aerospace, deployable space structure, biomedical devices, and textile materials.

In recent years, polymer based shape memory materials (SMP) have been attracting more and more attention due to their easy processing, rich monomer types, and flexibility in both synthesis and modification aspects. According to different structures, SMPs usually include block-copolymer, supramolecular polymer, crosslinked polymer, and polymer blends. There are varieties of SMPs which have been developed up to now. Some common SMPs include polyurethane, styrene-based polymers, acrylate-based polymers, thioene based polymers, and epoxy based polymers. Among those SMPs, shape memory epoxy (SMEP) and polyurethane (SMPU) are much investigated ones. SMPs covered lots of product forms such as film, fiber, fabric, foam, and gel. For purpose of desired property and effect, they can be also prepared into composites with other materials such as carbon materials and other inorganic fillers.

1.2.2 Shape memory theory

According to the types of shape memory materials, there are different shape memory mechanisms. Main three types of typical shape memory materials include shape memory alloys, shape memory polymers, and shape memory ceramics [63]. Many other shape memory materials are their derivatives such as various shape memory composites. Shape memory alloys such as

TiNi and Cu-Al-Ni alloys acts based on thermos-elasticity and the reversible transformation of austenite and martensite with the change of temperature. Shape memory ceramics mainly include (a) viscoelastic shape memory ceramics such as mica based glass ceramics, zirconia, and aluminium oxide whose viscoelastic mechanism is not clear yet; (2) martensite phase transformation ceramics such as zirconia and barium titanate acting; (3) ferroelectric shape memory ceramics such as PZT acting based on parallel-ferroelectric and reverse ferroelectric-ferroelectric transitions; (4) ferromagnetic shape memory ceramics such as tetragonal manganites acting based on paramagnetic-ferromagnetic, paramagnetic-reverse ferromagnetic, or orbital order-disorder transitions.

For shape memory polymers, there are at least two structures. One structure is soft part, and can be transferred to another shape by external force when reaching one condition such as one temperature (temperature responsive SMP) or placed in a certain environment such as one solution (solvent responsive SMP). Furthermore, this shape can be temporarily fixed by crystallization, glass transition, melting transition, reversible covalent or non-covalent bonds such as Diels–Alder reactions and supramolecular interactions. The other structure is hard part, and used to remember its original shape after SMP is transformed to another shape by force. This hard part can be achieved by introducing chemical crosslinks, crystalline phases or interpenetrating three dimensional networks [63, 64].

According to shape recovery types, there are basically stretching recovery and bending recovery of film-shaped SMPs, compression recovery of foam shaped SMPs, and shrinking recovery of gel-shaped SMPs. With regarding to evaluation of shape memory effects of SMPs, fixity ratio, recovery time, ratio, and recovery force are commonly used reference criterions.

However, up to now, due to the diversity of recovery ways, there are not strict or clear definitions in quantificationally explaining shape memory effectiveness especially for those bending or compression recoveries. For examples, how long should be stretched or what extent should be bended to evaluate the effects of stretching recovery or bending recovery. Therefore, the difference of the shape recovery effects under different shape transformation and fixing resulted in difficult comparison in shape memory effect for varieties of developed SMPs. In the future, the confirmation for evaluation methods of SMPs seems to be demandable.

1.2.3 Stimulus-responsive shape memory materials

According to stimulation types, SMPs can response to heat, light, solvent, electricity, humidity, and ultrasound [63]. Primary mechanisms of them are that SMPs can be endowed with different structures which are sensitive to those stimuluses, and thus lead to physical or chemical transformation or diffusion of chains or segments. Those changes in structures could be activated by heat effects such as glass transition, melting transition, crystallization, light effect, electric effect, physical effects such as supramolecular interaction, hydrophilic and hydrophobic interactions, and chemical effects such as oxidation or reduction.

The SMPs responding to heat are usually called as thermal (or temperature) responsive (triggered or induced or activated) shape memory polymers. They have been most investigated in the past few decades. As abovementioned, they can be stimulated mainly by glass transition, melting transition, and crystallization [81, 82]. There are thermal plastic and thermosetting SMPs. Thermosetting SMPs are to heat the polymers to a melting point (T_m) or higher temperature in order to blend with crosslinking agent, and then their crosslinking reaction is carried out in the mold to determine initial shape. After cooling and crystallization, the chemical crosslinking

structure is a stationary phase, while the crystalline phase is a reversible phase. When the temperature rises above T_m , the reversible phase melts and becomes soft, and thus can be easily shaped by external force. With the force maintained during the whole process, the SMP is cooled and fixed to another shape, and then the chains or segments of it are oriented and frozen. When heating the SMP above T_m , the molecular chains in the reversible phase naturally curls due to the action of entropy elasticity until reaching thermodynamic equilibrium state, so that shape recovery occurs and goes back to original shape status. Thermoplastic SMPs essentially form a stationary phase and a reversible phase in physically or chemically crosslinking. When the temperature rises above the glass transition temperature (T_g), the reversible phase is softened due to the microscopic Brown motion, while the stationary phase is still in a solidified state. At this status, the SMP is deformed and cooled by external force, and thus the reversible phase becomes solidified due to the hardening of the chains. When the SMP with new shape is heated above T_g , the reversible phase softens to reach thermodynamic equilibrium state under the recovery stress of the stationary phase, and thus the SMP restores to the original state from macroscopic point view.

Electro-responsive SMPs usually refer to the composite material of thermo-responsive shape memory polymers and electrically conductive materials such as conductive carbon powder, metal powder, and electrically conductive polymer [83, 84]. Their memory mechanism is similar to thermally responsive SMPs. Therefore, they can response to heat as well. When electro-responsive SMPs are subjected to one electrical field, the current occurs inside the SMPs. This generates heat, and lead to shape recovery. The rising extent and efficiency of temperature have directional relation with applied voltage and the addition amount of the electrically conductive fillers. Electro-responsive SMPs are promising to be used in electrical actuation field.

Photo responsive SMPs are based on the heat effect of photosensitizer, chemical reactions, or changes in chemical structure and spatial conformation [85, 86]. This kind of SMPs includes chemical structures such as benzene, or other components such as aromatic ketone, which are sensible to light. For example, cinnamic groups can form cross-linked covalent bonds under the irradiation of the ultraviolet light over 260 nm, while these bonds will be cleaved under ultraviolet light below 260 nm, which thus makes it possible for use as photo responsive shape memory polymer. One advantage for light responsive SMPs is they can achieve remote control, which make them promising in biomedical application.

There are also some other chemically and physically responsive SMP materials such as pH-, redox-, pressure-, moisture- and solvent induced shape memory polymers. These responses are usually based on the transformation of the chains in reversal phase between softness and solidification, reversal transformation of spatial conformation. Rich stimulation conditions for SMPs make them possible to be used in various applications especially in biomedical and actuation fields.

1.2.4 Different ways of shape recovery

According to different ways of shape recovery, SMPs are divided into one-way, two-way and multi-stage shape memory polymers. As shown in **Fig. 1.6a**, one-way SMPs can't naturally go back to the deformed status from original shape without the assistance of external force. They are the SMPs that have been mostly investigated in the past decades especially for thermo-responsive one-way SMPs. The factors that influence the shape memory properties of one-way mainly SMPs include the weight content and ratio of hard and soft segments, crystallization of soft segments, crossing linking extent, and the content of sensitive functional groups or components (i.e.,

sensitive fillers for responding to stimulus) as well as some external processing conditions such as cooling fixing and recovering temperatures. These factors have direct impact on the fixing ratio, recovery time, ratio, and force of one-way SMPs.

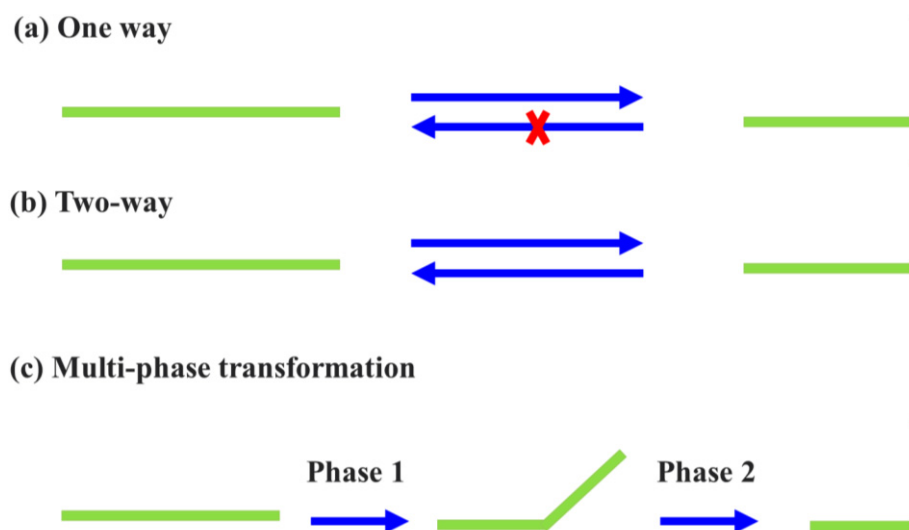


Fig. 1.6 Different ways of shape memory, (a) one-way shape memory; (b) Two-way shape memory; (c) Multi-stage shape memory

Two-way SMPs can show reversible shape switching between two different shapes under different stimulation environments without the assistance of external force, as illustrated in **Fig. 1.6b**. These two-way SMPs mainly include liquid crystalline elastomers (LCE), T_m -type SMPs under constant stress, and SMP laminated composites. LCEs can achieve a reversible shape change upon stimulation such as light, heat, and electric field due to their reversible contraction and extension [81]. Thermo-responsive LCEs work based on the interaction between liquid crystalline order and polymer elasticity. When a LCE film is heated up, a transition anisotropic phase to isotropic phase occurs, thus resulting in the disordered arrangement of the liquid crystalline. This will lead to the contraction of the film make it naturally bend to another shape. When cooling the film below the phase-transition temperature, it will expand and go back to its original size. T_m -type two-way SMPs work under constant stress load based on crystallization

induced elongation (CIE) during cooling and melting induced contraction (MIC) during heating. SMP laminated composites with two-way effect utilizes the mismatched mechanical properties of different SMPs such as different elastic modulus and mechanical strength with varying temperature. In addition, thermo-responsive semi-crystalline polymers can also show two-way shape memory effects under constant loading. They work based on the cooling-induced extension of semi-crystalline polymer films under a tensile load, and heating-induced contraction.

Multi-stage SMPs can remember at least two temporary shape, as shown in **Fig. 1.6c**. The shape memory effect at different stages can be activated through different stimulation extent using one stimulus such as different T_g stimulation, or through different stimulus such as temperature and solvent. Multi-stage SMPs generally have multiphase polymer network. This multiphase three-dimensional network contains at least two independent domains, which are corresponding to individual phase transition. They are usually achieved by chemical or physical cross-linking, arrangement of liquid crystalline, and combination of one-way or two-way SMPs with distinct responsive structures [87]. For thermos-responsive multi-stage SMPs, introducing multiple segments with different T_g is a common way to fabricate multi-stage SMPs that response to different temperatures and transform to individual temporary shapes.

1.2.5 Shape memory actuation

Shape memory polymers are promising to be used in many industrial fields such as sensors, actuators, smart devices, aerospace, deployable space structure, biomedical devices, and textile materials, due to their easy processing, rich monomer types, various stimulation response, different ways of shape memory, and flexibility in both synthesis and modification aspects. In these applications, a shape memory switch, which can be possibly used in control systems like in

sensor and actuator fields, has emerged because some shape memory polymers have reached high shape fixity ratio, shape recovery ratio, flexible structure adjustability, rapid and sensitive response, stable dimension, and/or good durability [73, 88-91]. To date, there is still insufficient attention which was put on the researches regarding adjustable shape memory switches. Here, some relevant work reported in recent years will be introduced. Zhu and Wang prepared one kind of light-actuated two-way reversible shape memory polymer by incorporating polydopamine (PDA) nanospheres into semi-crystalline polymer networks [92]. Because of the strong absorption of PDA to light, this composite showed a reversible angle change of 45° when the light was switched on and off. The speed of angle change could be faster with stronger light or higher content of PDA. Ambrogi and coworkers synthesized epoxy-based shape-memory liquid crystalline by using carboxylic acid as a curing agent [93]. The controlled degree of liquid crystallinity, and high actuation stress and strain could be achieved by simply changing the aliphatic chain length of the curing agent. Strain actuation could be modulated in the strain range from approximately 60% to 160%. Maiti and coworkers used linear hexamethylene diisocyanate (HMDI) to prepare the polyurethanes (PUs) with different hard segment content (HSC) [94]. The result suggested that the increase of HSC gave decreased shape fixity and increased shape recovery. In summary, the studies described were well done, but the focus was not on the investigation of shape memory switches. With increasing attention of SMPs on shape memory actuation, the development of smart switching devices based on shape memory polymers is considered to be promising [95, 96].

For SMP switches, high sensitivity, recyclable recovery, good fixity, efficient responding, and flexible adjustability are required to cater for the different demands of sensors and actuators. It is

difficult for SMPs to achieve these points by themselves. Presently, there are two basic methods, internal fabrication and external modification, that can possibly be used for adjustable shape memory switches. Internal fabrication can potentially achieve the variation such as glass transition temperature (T_g), melting temperature (T_m), and mechanical properties of SMP by the control of chemical composition like the ratio of hard and soft segments [73, 93, 94, 97], or the addition of nano/micro fillers and functional molecules [96-101]. Some researchers have investigated the properties of SMPs by changing internal structures [91, 102, 103]. However, there was not enough concentration on the study for shape memory switching effect.

In our group, we also fabricated many shape memory composites that include carbon nanofiber/epoxy [104], silica/epoxy composite [105], silica/water-borne epoxy foam [106], and carbon nanotube/waterborne epoxy nanocomposites [107, 108]. Their shape memory effects, including recovery ratio, time, and stress, and other properties like mechanical performance, were investigated in detail. Based on our experience, it is still a challenge to achieve efficient responding, highly repeatable recovery, and flexible adjustability of SMPs because of the difficulty in fine adjustability of microstructure and composition. At present, the modification by adding fillers or varying internal structure is expected to achieve better shape memory and switching effect. Carbon materials may be promising as the fillers of SMPs for application in temperature responsive shape memory materials due to their good thermal and electrical conductivity as well as unique 1-, 2- and 3-dimensional micro/nano-structures.

1.3 Purpose, proposal and significance of research

Rapid development of advanced intelligence security and smart electronic equipment has led to the demand for functional electromagnetic shielding devices, which can respond to external

stimulus (i.e., electricity, heat, and light) or/and have tunable shielding effect, such as controllable EM shielding switch for cutoff and reception of electromagnetic signals [109-116]. For example, Wang and co-workers have reported a kind of hydro-sensitive sandwich structure by embedding porous polypropylene non-woven spacers into highly conductive pyrolytic graphite papers. In the presence and absence of polar water molecules, porous spacers achieved a switchable structural transformation through polar induced interfaces. Thus, under dry and wet conditions, the sandwich structures exhibited weak and strong electromagnetic shielding ability, respectively [117]. Furthermore, Chen et al. prepared a biomass-derived electrically conductive macroscopic carbon grid (MCG) by carbonizing wood-pulp fabric matting. They found that double-layered MCG showed tunable electromagnetic shielding performance by varying the interleaving degree of the stacked grids through tiny translational motion [118]. Therefore, increasing attention is being paid to developing carbon based composites for functional electromagnetic shielding.

As mentioned in section 1.2, many types of shape memory polymers (SMPs) containing films, foams, fibers, hydrogels, and fabrics, have been reported, which can respond to various external stimuli such as heat, electricity, light, chemical solvent and pH. In most cases, shape recovery and fixity effects, which include recovery time, ratio, force, and fixity ratio, were mainly studied to estimate primary performance of those SMPs. However, in terms of the evaluation for their practical applications, little relevant work has been performed except for limited applications, such as soft actuators, functional textures, and medical applications [119-125]. As for the reason, there is still a limited understanding of how SMPs might be applicable to different fields.

Thus, with the aims of developing functional shielding devices and expanding the application of SMPs, we introduced shape memory polymers to electromagnetic shielding field. Shape

memory effect was used as actuation force for adjusting the shape variation of functional shielding devices. As illustrated in **Fig 1.7**, after endowment with shape memory effect, conventional shielding films are possible to adjust and fix thickness, or achieve different bending to vary shielding effect.

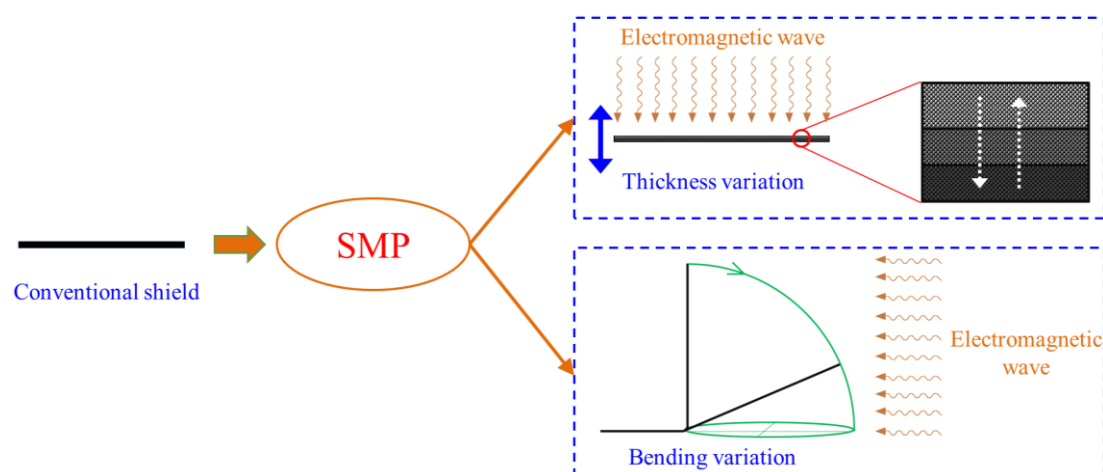


Fig. 1.7 Endowment of conventional electromagnetic shielding materials with shape memory actuation effect for adjustment of thickness or bending to vary shielding effect.

In this research, shape memory polyurethane (SMPU), one type of thermoplastic polymer consisting of hard and soft segments, was introduced as a substrate. It was selected because of its easy processing, excellent flexibility, and environmental friendliness. The shape memory function of this SMPU is stimulated and driven by temperature, with glass transition temperature determining the shape switching of the SMPU. By using SMPU as three dimensional matrix, carbon/SMPU with different three dimensional structures were fabricated for functional electromagnetic shielding. Those functional carbon/SMPU structural composites are expected to cater for the demand for various smart electromagnetic shielding devices.

1.4 Outline of dissertation

In this dissertation, by using shape memorable polyurethane (SMPU) as supporting matrix,

varieties of nano/micro-carbon based composites with different three dimensional structures were designed and fabricated for stimuli-responsive adjustable electromagnetic shielding. Shape memory effect was mainly utilized for driving in thickness variation of those functional shielding composites. These functional shielding composites include thickness-adjustable graphite micro-flakes@SMPU sponge (G@SMPU), vapor grown carbon fiber (VGCF) based polyurethane foam (VGCF@PUF), gradient VGCF based shape memory polyurethane foam (VGCF@SMPUF), and unidirectional nonwoven VGCF based polyurethane fibrous membrane (VGCF@PUFM). Their fabrication approaches are illustrated in **Fig. 1.8**, and explained in the corresponding figure titles. Next, each chapter will be introduced.

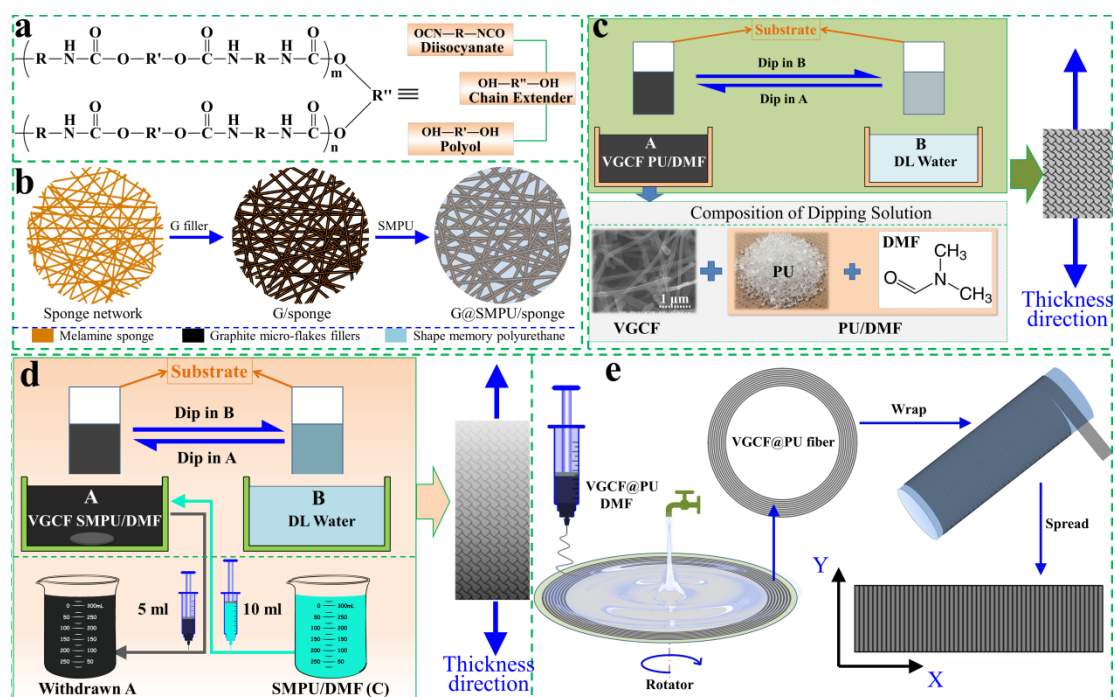


Fig. 1.8 (a) Chemical structure of SMPU; (b) Fabrication approach of G@SMPU by filling of graphite micro-flakes and SMPU in turn; (c) VGCF based PU foam (VGCF@PUF) fabricated by repeated dipping in A and B solutions; (d) gradient VGCF based SMPU foam (VGCF@SMPUF) fabricated with gradual dilution of VGCF during each dipping in A solution; (e) Fabrication approaches of unidirectional nonwoven VGCF@PUFM by rotation spinning in H₂O flow to form striped VGCF@PU fiber bundles, followed by assembly of which to be membrane.

In chapter 1, present development situation of electromagnetic shielding was presented at first. Then, electromagnetic shielding theory and recent electromagnetic shielding materials was systematically revealed. After that, the recent research related to shape memory actuation was simply overviewed. Based on the abovementioned, the purpose and significance of this dissertation research was proposed in the end.

In chapter 2, with the aim to understand the memory effect of SMPU on shape actuation, multi-layer graphene oxide (MLGO) coated shape memory polyurethane (MLGO@SMPU) was firstly fabricated by multiple dipping in GO solution for adjustable shape memory switching devices. The morphologies and mechanical properties were measured. Then, the shape memory actuation effects based on bending behaviour, which mainly included angle recovery ratio, recovery time, bending recovery force, and angle fixity ratio, were evaluated by homemade apparatus. This shape memory actuated MLGO@SMPU is expected to be applied to smart switching devices such as in sensor and actuator fields.

In chapter 3, by using shape memory effect as driving force, driving thickness adjustable graphite (G) micro-flakes@shape memory polyurethane (G@SMPU) sponge was fabricated by two-step dipping separately in G-dispersed aqueous solution and SMPU/THF solution for high-performance microwave shielding. The microwave shielding effect of the G@SMPU specimens with different G loading content were evaluated by free space method. The shielding effect under different compression was investigated.

In chapter 4, instead of graphite micro-flakes, VGCFs having higher electrical conductivity was used as carbon fillers of polyurethane. By way of dipping coating, VGCF based polyurethane foam was fabricated based on H₂O-DMF solvent exchange for compression-adjusted high-performance microwave shielding. The obtained VGCF@PUF specimens with different thicknesses were obtained by hot compression under relatively high temperature and suitable pressure. The electrical conductivity of the VGCF@PUF under different hot compression was investigated due to its significance to electromagnetic shielding. In the end, microwave shielding of the VGCF@PUF specimens with different degrees of compression was evaluated by coaxial transmission line method in the frequency range of 0.5-18 GHz. Different shielding effect was expected when varying hot compression extent.

In chapter 5, gradient VGCF based shape memory polyurethane foam (VGCF@SMPUF) was fabricated by alternative dipping in a gradually diluted VGCF@SMPU/DMF solution and distilled water for directional microwave shielding. Shape memory performance for this VGCF@SMPUF was considered to achieve by heat transfer of thermal conductive VGCF. Shielding effectiveness was adjusted through different degrees of angle recovery. The influence of hot compression on the bending recovery and shielding effects of the two sides of this gradient VGCF@SMPUF was investigated. It was expected that there are different bending based shape memory effect, and microwave shielding properties for the two sides with low and high content of VGCF, respectively.

In chapter 6, unidirectional nonwoven VGCF based polyurethane (PU) fibrous membrane (VGCF@PUFM) was fabricated by rotation spinning based on DMF-H₂O exchange for directional microwave shielding. Different electrical conductivity and mechanical strength in parallel and perpendicular directions were expected. The shielding performance of this VGCF@PUFM was evaluated by free space method in which the electromagnetic wave with polarized property in the frequency range of 4-14 GHz was used. It was anticipated that this VGCF@PUFM could possibly exhibited varying microwave shielding performance.

In chapter 7, summary for this dissertation was presented based on the researches as-abovementioned.

References

- [1] <https://byjus.com/physics/characteristics-of-em-waves>
- [2] A Ishimaru (2017). *Electromagnetic wave propagation, radiation, and scattering: from fundamentals to applications*. John Wiley & Sons.
- [3] Joseph Mercola, *Researcher Explains How Electromagnetic Fields Damage Your Health*, <http://mieuxprevenir.blogspot.com/2018/04/researcher-dr-paul-heroux-explains-how.html>, 2018, Apr, 29.
- [4] M Hasan, G., A Sheikh, I., Karim, S., Haque, A., A Kamal, M., G Chaudhary, A., ... & Mirza, Z. (2014). Effect of electromagnetic radiations on neurodegenerative diseases-technological revolution as a curse in disguise. *CNS & Neurological Disorders-Drug Targets (Formerly Current Drug Targets-CNS & Neurological Disorders)*, 13(8), 1406-1412.
- [5] Joshi, A., & Datar, S. (2015). Carbon nanostructure composite for electromagnetic interference shielding. *Pramana*, 84(6), 1099-1116.
- [6] Sankaran, S., Deshmukh, K., Ahamed, M. B., & Pasha, S. K. (2018). Recent advances in electromagnetic interference shielding properties of metal and carbon filler reinforced flexible polymer composites: a review. *Composites Part A: Applied Science and Manufacturing*, 114, 49-71.
- [7] Jiang, D., Murugadoss, V., Wang, Y., Lin, J., Ding, T., Wang, Z., ... & Wei, R. (2019). Electromagnetic interference shielding polymers and nanocomposites-a review. *Polymer Reviews*, 1-58.
- [8] Shukla, V. (2019). Review of electromagnetic interference shielding materials fabricated by iron ingredients. *Nanoscale Advances*.

- [9] Saini, P., & Arora, M. (2012). Microwave absorption and EMI shielding behavior of nanocomposites based on intrinsically conducting polymers, graphene and carbon nanotubes. In *New Polymers for Special Applications*. IntechOpen.
- [10] Singh, A. K., Shishkin, A., Koppel, T., & Gupta, N. (2018). A review of porous lightweight composite materials for electromagnetic interference shielding. *Composites Part B: Engineering*, 149, 188-197
- [11] Geetha, S., Satheesh Kumar, K. K., Rao, C. R., Vijayan, M., & Trivedi, D. C. (2009). EMI shielding: Methods and materials—A review. *Journal of applied polymer science*, 112(4), 2073-2086.
- [12] Shirakawa, H., Louis, E. J., MacDiarmid, A. G., Chiang, C. K., & Heeger, A. J. (1977). Synthesis of electrically conducting organic polymers: halogen derivatives of polyacetylene,(CH)_x. *Journal of the Chemical Society, Chemical Communications*, (16), 578-580.
- [13] Shacklette, L. W., & Colaneri, N. F. (1991, May). EMI shielding measurements of conductive polymer blends. *IEEE Instrumentation and Measurement Technology Conference*, IEEE, 1991, 72-78.
- [14] Taka, T. (1991). EMI shielding measurements on poly (3-octyl thiophene) blends. *Synthetic Metals*, 41(3), 1177-1180.
- [15] Trivedi, D. C., & Dhawan, S. K. (1993). Shielding of electromagnetic interference using polyaniline. *Synthetic metals*, 59(2), 267-272.
- [16] Colaneri, N. F., & Schacklette, L. W. (1992). EMI shielding measurements of conductive polymer blends. *IEEE transactions on instrumentation and measurement*, 41(2), 291-297.
- [17] Naishadham, K. (1992). Shielding effectiveness of conductive polymers. *IEEE transactions*

on electromagnetic compatibility, 34(1), 47-50.

[18] Dhawan, S. K., Singh, N., & Rodrigues, D. (2003). Electromagnetic shielding behaviour of conducting polyaniline composites. *Science and Technology of Advanced Materials*, 4(2), 105-113.

[19] Joo, J., & Epstein, A. J. (1994). Electromagnetic radiation shielding by intrinsically conducting polymers. *Applied Physics Letters*, 65(18), 2278-2280.

[20] Joo, J., & Lee, C. Y. (2000). High frequency electromagnetic interference shielding response of mixtures and multilayer films based on conducting polymers. *Journal of applied physics*, 88(1), 513-518.

[21] Barra, G. M., Leyva, M. E., Soares, B. G., & Sens, M. (2002). Solution-cast blends of polyaniline–DBSA with EVA copolymers. *Synthetic metals*, 130(3), 239-245.

[22] Hong, Y. K., Lee, C. Y., Jeong, C. K., Sim, J. H., Kim, K., Joo, J., ... & Byun, S. W. (2001). Electromagnetic interference shielding characteristics of fabric complexes coated with conductive polypyrrole and thermally evaporated Ag. *Current applied physics*, 1(6), 439-442.

[23] Wang, Y., & Jing, X. (2005). Intrinsically conducting polymers for electromagnetic interference shielding. *Polymers for advanced technologies*, 16(4), 344-351.

[24] Li, C., Bai, H., & Shi, G. (2009). Conducting polymer nanomaterials: electrosynthesis and applications. *Chemical Society Reviews*, 38(8), 2397-2409.

[25] Shi, Y., Peng, L., Ding, Y., Zhao, Y., & Yu, G. (2015). Nanostructured conductive polymers for advanced energy storage. *Chemical Society Reviews*, 44(19), 6684-6696.

[26] Chen, Z., Xu, C., Ma, C., Ren, W., & Cheng, H. M. (2013). Lightweight and flexible graphene foam composites for high-performance electromagnetic interference shielding.

Advanced materials, 25(9), 1296-1300.

[27] Yousefi, N., Sun, X., Lin, X., Shen, X., Jia, J., Zhang, B., ... & Kim, J. K. (2014). Highly aligned graphene/polymer nanocomposites with excellent dielectric properties for high-performance electromagnetic interference shielding. *Advanced Materials*, 26(31), 5480-5487.

[28] Wu, Y., Wang, Z., Liu, X., Shen, X., Zheng, Q., Xue, Q., & Kim, J. K. (2017). Ultralight graphene foam/conductive polymer composites for exceptional electromagnetic interference shielding. *ACS applied materials & interfaces*, 9(10), 9059-9069.

[29] Zhang, K., Yu, H. O., Shi, Y. D., Chen, Y. F., Zeng, J. B., Guo, J., ... & Wang, M. (2017). Morphological regulation improved electrical conductivity and electromagnetic interference shielding in poly (L-lactide)/poly (ϵ -caprolactone)/carbon nanotube nanocomposites via constructing stereocomplex crystallites. *Journal of Materials Chemistry C*, 5(11), 2807-2817.

[30] Zeng, Z., Jin, H., Chen, M., Li, W., Zhou, L., Xue, X., & Zhang, Z. (2017). Microstructure design of lightweight, flexible, and high electromagnetic shielding porous multiwalled carbon nanotube/polymer composites. *small*, 13(34), 1701388.

[31] Zhang, K., Li, G. H., Feng, L. M., Wang, N., Guo, J., Sun, K., ... & Wang, M. (2017). Ultralow percolation threshold and enhanced electromagnetic interference shielding in poly (L-lactide)/multi-walled carbon nanotube nanocomposites with electrically conductive segregated networks. *Journal of Materials Chemistry C*, 5(36), 9359-9369.

[32] Rahaman, M., Chaki, T. K., & Khastgir, D. (2011). Development of high performance EMI shielding material from EVA, NBR, and their blends: effect of carbon black structure. *Journal of materials science*, 46(11), 3989-3999.

[33] Yan, Y., Xia, H., Qiu, Y., Xu, Z., & Ni, Q. Q. (2019). Shape memory driving

thickness-adjustable G@ SMPU sponge with ultrahigh carbon loading ratio for excellent microwave shielding performance. *Materials Letters*, 236, 116-119.

[34] Song, W. L., Wang, J., Fan, L. Z., Li, Y., Wang, C. Y., & Cao, M. S. (2014). Interfacial engineering of carbon nanofiber–graphene–carbon nanofiber heterojunctions in flexible lightweight electromagnetic shielding networks. *ACS applied materials & interfaces*, 6(13), 10516-10523.

[35] Chung, D. D. L. (2001). Electromagnetic interference shielding effectiveness of carbon materials. *carbon*, 39(2), 279-285.

[36] Al-Saleh, M. H., Saadeh, W. H., & Sundararaj, U. (2013). EMI shielding effectiveness of carbon based nanostructured polymeric materials: a comparative study. *Carbon*, 60, 146-156.

[37] Oganov, A. R., Hemley, R. J., Hazen, R. M., & Jones, A. P. (2013). Structure, bonding, and mineralogy of carbon at extreme conditions. *Reviews in Mineralogy and Geochemistry*, 75(1), 47-77.

[38] Song, W. L., Cao, M. S., Lu, M. M., Bi, S., Wang, C. Y., Liu, J., ... & Fan, L. Z. (2014). Flexible graphene/polymer composite films in sandwich structures for effective electromagnetic interference shielding. *Carbon*, 66, 67-76.

[39] Ling, J., Zhai, W., Feng, W., Shen, B., Zhang, J., & Zheng, W. G. (2013). Facile preparation of lightweight microcellular polyetherimide/graphene composite foams for electromagnetic interference shielding. *ACS applied materials & interfaces*, 5(7), 2677-2684.

[40] Hong, X., & Chung, D. D. L. (2017). Carbon nanofiber mats for electromagnetic interference shielding. *Carbon*, 111, 529-537.

[41] Song, W. L., Guan, X. T., Fan, L. Z., Cao, W. Q., Wang, C. Y., & Cao, M. S. (2015). Tuning

three-dimensional textures with graphene aerogels for ultra-light flexible graphene/texture composites of effective electromagnetic shielding. *Carbon*, 93, 151-160.

[42] Zou, L., Zhang, S., Li, X., Lan, C., Qiu, Y., & Ma, Y. (2016). Step-by-Step Strategy for Constructing Multilayer Structured Coatings toward High-Efficiency Electromagnetic Interference Shielding. *Advanced Materials Interfaces*, 3(5), 1500476.

[43] Wang, X. (2011). Investigation of electromagnetic shielding effectiveness of nanostructural carbon black/ABS composites. *J Electromagn Anal Appl.*, 3(05), 160-164

[44] Endo M, Kim Y, Hayashi T, Nishimura K, Matusita T, Miyashita K, et al. (2001). Vapor-grown carbon fibers (VGCFs): basic properties and their battery applications. *Carbon*, 39(9):1287-97.

[45] Das, A., Hayvaci, H. T., Tiwari, M. K., Bayer, I. S., Erricolo, D., & Megaridis, C. M. (2011). Superhydrophobic and conductive carbon nanofiber/PTFE composite coatings for EMI shielding. *Journal of colloid and interface science*, 353(1), 311-315.

[46] Yang, S., Lozano, K., Lomeli, A., Foltz, H. D., & Jones, R. (2005). Electromagnetic interference shielding effectiveness of carbon nanofiber/LCP composites. *Composites Part A: applied science and manufacturing*, 36(5), 691-697.

[47] Lee, B. O., Woo, W. J., & Kim, M. S. (2001). EMI shielding effectiveness of carbon nanofiber filled poly (vinyl alcohol) coating materials. *Macromolecular Materials and Engineering*, 286(2), 114-118.

[48] Chung, D. D. L. (2012). Carbon materials for structural self-sensing, electromagnetic shielding and thermal interfacing. *Carbon*, 50(9), 3342-3353.

[49] Lee, B. O., Woo, W. J., Park, H. S., Hahm, H. S., Wu, J. P., & Kim, M. S. (2002). Influence of

aspect ratio and skin effect on EMI shielding of coating materials fabricated with carbon nanofiber/PVDF. *Journal of materials science*, 37(9), 1839-1843.

[50] Yah CS, Iyuke SE, Simate GS, Unuabonah EI, Bathgate G, Matthews G, et al. (2011). Continuous synthesis of multiwalled carbon nanotubes from xylene using the swirled floating catalyst chemical vapor deposition technique. *J Mater Res.*, 26(05):640-644.

[51] Iqbal J, Rafique MMA. (2011). Production of carbon nanotubes by different routes - a review. *J Encapsulation Adsorpt Sci.*, 1(2):29–34.

[52] Ma P-C, Siddiqui NA, Marom G, Kim J-K. (2010). Dispersion and functionalization of carbon nanotubes for polymer-based nanocomposites: a review. *Compos. Part A: Appl. Sci. Manuf.*, 41(10):1345–1367.

[53] Geim, A. K., & Novoselov, K. S. (2010). The rise of graphene. In *Nanoscience and Technology: A Collection of Reviews from Nature Journals*, pp. 11-19.

[54] Novoselov, K. S., Geim, A. K., Morozov, S. V., Jiang, D., Zhang, Y., Dubonos, S. V., ... & Firsov, A. A. (2004). Electric field effect in atomically thin carbon films. *science*, 306(5696), 666-669.

[55] Ferrari, A. C., Meyer, J. C., Scardaci, V., Casiraghi, C., Lazzeri, M., Mauri, F., ... & Geim, A. K. (2006). Raman spectrum of graphene and graphene layers. *Physical review letters*, 97(18), 187401.

[56] Liang, J., Wang, Y., Huang, Y., Ma, Y., Liu, Z., Cai, J., ... & Chen, Y. (2009). Electromagnetic interference shielding of graphene/epoxy composites. *Carbon*, 47(3), 922-925.

[57] Zhang, H. B., Yan, Q., Zheng, W. G., He, Z., & Yu, Z. Z. (2011). Tough graphene– polymer microcellular foams for electromagnetic interference shielding. *ACS applied materials &*

interfaces, 3(3), 918-924.

[58] Yan, D. X., Ren, P. G., Pang, H., Fu, Q., Yang, M. B., & Li, Z. M. (2012). Efficient electromagnetic interference shielding of lightweight graphene/polystyrene composite. *Journal of Materials Chemistry*, 22(36), 18772-18774.

[59] Yang, Y., Gupta, M. C., Dudley, K. L., & Lawrence, R. W. (2005). Novel carbon nanotube-polystyrene foam composites for electromagnetic interference shielding. *Nano letters*, 5(11), 2131-2134.

[50] Yang, Y., Gupta, M. C., Dudley, K. L., & Lawrence, R. W. (2005). A comparative study of EMI shielding properties of carbon nanofiber and multi-walled carbon nanotube filled polymer composites. *Journal of nanoscience and nanotechnology*, 5(6), 927-931.

[61] Maiti, S., Shrivastava, N. K., Suin, S., & Khatua, B. B. (2013). Polystyrene/MWCNT/graphite nanoplate nanocomposites: efficient electromagnetic interference shielding material through graphite nanoplate-MWCNT-graphite nanoplate networking. *ACS applied materials & interfaces*, 5(11), 4712-4724.

[62] Das, N. C., Khastgir, D., Chaki, T. K., & Chakraborty, A. (2000). Electromagnetic interference shielding effectiveness of carbon black and carbon fibre filled EVA and NR based composites. *Composites part A: applied science and manufacturing*, 31(10), 1069-1081.

[63] Sun, L., Huang, W. M., Ding, Z., Zhao, Y., Wang, C. C., Purnawali, H., & Tang, C. (2012). Stimulus-responsive shape memory materials: a review. *Materials & Design*, 33, 577-640.

[64] Behl, M.; Razzaq, M. Y.; Lendlein, A. (2010). Multifunctional shape memory polymers. *Adv. Mater.*, 22(31), 3388-3410.

[65] Chan, B. Q. Y.; Low, Z. W. K.; Heng, S. J. W.; Chan, S. Y.; Owh, C.; Loh, X. J. (2016).

Recent advances in shape memory soft materials for biomedical applications. *ACS Appl. Mater. Interfaces*, 8(16), 10070-10087.

[66] Jani, J. M.; Leary, M.; Subic, A.; Gibson, M. A. (2014). A review of shape memory alloy research, applications and opportunities. *Mater. Design (1980-2015)*, 56, 1078-1113.

[67] Lai, A.; Du, Z.; Gan, C. L.; Schuh, C. A. (2013). Shape memory and superelastic ceramics at small scales. *Science*, 341(6153), 1505-1508.

[68] Lu, W.; Le, X.; Zhang, J.; Huang, Y.; Chen, T. (2017). Supramolecular shape memory hydrogels: A new bridge between stimuli-responsive polymers and supramolecular chemistry. *Chem. Soc. Rev.*, 46(5), 1284-1294.

[69] Löwenberg, C.; Balk, M.; Wischke, C.; Behl, M.; Lendlein, A. (2017). Shape-memory hydrogels: Evolution of structural principles to enable shape switching of hydrophilic polymer networks. *Accounts Chem. Res.*, 50(4), 723-732.

[70] Li, G.; Uppu, N. (2010). Shape memory polymer based self-healing syntactic foam: 3-D confined thermomechanical characterization. *Compos. Sci. Technol.*, 70(9), 1419-1427.

[71] Deng, J.; Zhang, Y.; Zhao, Y.; Chen, P.; Cheng, X.; Peng, H. (2015). A shape-memory supercapacitor fiber. *Angew. Chem. Int. Edit.*, 54(51), 15419-15423.

[72] Zhong, J.; Meng, J.; Yang, Z.; Poulin, P.; Koratkar, N. (2015). Shape memory fiber supercapacitors. *Nano Energy*, 17, 330-338.

[73] Huang, M.; Zheng, L.; Wang, L.; Dong, X.; Gao, X.; Li, C.; Wang, D. (2017). Double crystalline multiblock copolymers with controlling microstructure for high shape memory fixity and recovery. *ACS Appl. Mater. Interfaces*, 9(35), 30046-30055.

[74] Xie, Y.; Meng, Y.; Wang, W.; Zhang, E.; Leng, J.; Pei, Q. (2018) Bistable and reconfigurable

photonic crystals electroactive shape memory polymer nanocomposite for ink free rewritable paper. *Adv. Funct. Mater.*, 1802430.

[75] Du, L.; Xu, Z.; Fan, C.; Xiang, G.; Yang, K.; Wang, Y. (2018). A fascinating metallo supramolecular polymer network with thermal/magnetic/light responsive shape memory effects anchored by Fe₃O₄ nanoparticles. *Macromolecules*, 51(3), 705-715.

[76] Le, X.; Zhang, Y.; Lu, W.; Wang, L.; Zheng, J.; Ali, I.; et al. (2018). Novel anisotropic hydrogel with integrated self-deformation and controllable shape memory effect. *Macromol. Rapid Comm.*, 39(9), 1800019.

[77] Huang, J.; Liao, J.; Wang, T.; Sun, W.; Tong, Z. (2018). Super strong dopamine hydrogels with shape memory and bioinspired actuating behaviours modulated by solvent exchange. *Soft Matter*, 14(13), 2500-2507.

[78] Razzaq, M. Y.; Behl, M.; Kratz, K., Lendlein, A. (2013) Multifunctional hybrid nanocomposites with magnetically controlled reversible shape-memory effect. *Adv. Mater.*, 25(40), 5730-5733.

[79] Fang, Y.; Ni, Y.; Leo, S. Y.; Taylor, C.; Basile, V.; Jiang, P. (2015). Reconfigurable photonic crystals enabled by pressure-responsive shape-memory polymers. *Nat. Commun.*, 6, 7416.

[80] Fang, Z.; Kuang, Y.; Zhou, P.; Ming, S.; Zhu, P.; Liu, Y.; et al. (2017). Programmable shape recovery process of water-responsive shape-memory poly (vinyl alcohol) by wettability contrast strategy. *ACS Appl. Mater. Interfaces*, 9(6), 5495-5502.

[81] Hu, J., Zhu, Y., Huang, H., & Lu, J. (2012). Recent advances in shape-memory polymers: Structure, mechanism, functionality, modeling and applications. *Progress in Polymer Science*, 37(12), 1720-1763.

- [82] Liu, Y., Du, H., Liu, L., & Leng, J. (2014). Shape memory polymers and their composites in aerospace applications: a review. *Smart Materials and Structures*, 23(2), 023001.
- [83] Wang, W., Liu, Y., & Leng, J. (2016). Recent developments in shape memory polymer nanocomposites: Actuation methods and mechanisms. *Coordination Chemistry Reviews*, 320, 38-52.
- [84] Luo, X., & Mather, P. T. (2010). Conductive shape memory nanocomposites for high speed electrical actuation. *Soft Matter*, 6(10), 2146-2149.
- [85] Hager, M. D., Bode, S., Weber, C., & Schubert, U. S. (2015). Shape memory polymers: past, present and future developments. *Progress in Polymer Science*, 49, 3-33.
- [86] Berg, G. J., McBride, M. K., Wang, C., & Bowman, C. N. (2014). New directions in the chemistry of shape memory polymers. *Polymer*, 55(23), 5849-5872.
- [87] Zhao, Q., Qi, H. J., & Xie, T. (2015). Recent progress in shape memory polymer: New behavior, enabling materials, and mechanistic understanding. *Progress in Polymer Science*, 49, 79-120.
- [88] Wang, W.; Shen, D.; Li, X.; Yao, Y.; Lin, J.; Wang, A.; et al. (2018). Light-driven shape-memory porous films with precisely controlled dimensions. *Angew. Chem.*, 130(8), 2161-2165.
- [89] Riccardi, L.; Naso, D.; Janocha, H.; & Turchiano, B. (2012). A precise positioning actuator based on feedback-controlled magnetic shape memory alloys. *Mechatronics*, 22(5), 568-576.
- [90] Ur Rehman, H.; Chen, Y.; Hedenqvist, M. S.; Li, H.; Xue, W.; Guo, Y. L.; et al. (2018). Self-healing shape memory PUPCL copolymer with high cycle life. *Adv. Funct. Mater.*, 28(7), 1704109.

- [91] Meng, H.; Li, G. (2013). A review of stimuli-responsive shape memory polymer composites. *Polymer*, 54(9), 2199-2221.
- [92] Wang, K.; Jia, Y.; Zhu, X. (2017). Two-way reversible shape memory polymers made of cross-linked cocrystallizable random copolymers with tunable actuation temperatures. *Macromolecules*, 50(21), 8570-8579.
- [93] Belmonte, A.; Lama, G. C.; Gentile, G.; Fernández-Francos, X.; De la Flor, S.; Cerruti, P.; et al. (2017). Synthesis and characterization of liquid-crystalline networks: Toward autonomous shape-memory actuation. *J. Phy. Chem. C*, 121(40), 22403-22414.
- [94] Biswas, A.; Aswal, V. K.; Ray, B.; Maiti, P. (2018). Nanostructure-controlled shape memory effect in polyurethanes. *J. Phy. Chem. C*, 122(20), 11167-11176.
- [95] Yan, W.; Rudolph, T.; Noechel, U.; Gould, O.; Behl, M.; Kratz, K.; Lendlein, A. (2018) Reversible actuation of thermoplastic multiblock copolymers with overlapping thermal transitions of crystalline and glassy domains. *Macromolecules*, 51, 4624–4632
- [96] Belmonte, A.; Lama, G. C.; Gentile, G.; Cerruti, P.; Ambrogio, V.; Fernández-Francos, X.; De la Flor, S. (2017). Thermally-triggered free-standing shape-memory actuators. *Eur. Polym. J.*, 97, 241-252.
- [97] Parameswaranpillai, J.; Ramanan, S. P.; Jose, S.; Siengchin, S.; Magueresse, A.; Janke, A.; Pionteck, J. (2017). Shape memory properties of Epoxy/PPO–PEO–PPO triblock copolymer blends with tunable thermal transitions and mechanical characteristics. *Ind. Eng. Chem. Res.*, 56(47), 14069-14077.
- [98] Ji, S.; Fan, F.; Sun, C.; Yu, Y.; Xu, H. (2017). Visible light-induced plasticity of shape memory polymers. *ACS Appl. Mater. Interfaces*, 9(38), 33169-33175.

- [99] Mishra, S. R., & Tracy, J. B. (2018). Sequential actuation of shape-memory polymers through wavelength-selective photothermal heating of gold nanospheres and nanorods. *ACS Applied Nano Materials*, 1(7), 3063-3067.
- [100] Li, C.; Qiu, L.; Zhang, B.; Li, D.; Liu, C. Y. (2016). Robust vacuum-/air-dried graphene aerogels and fast recoverable shape-memory hybrid foams. *Adv. Mater.*, 28(7), 1510-1516.
- [101] Zhang, P.; Behl, M.; Peng, X.; Razzaq, M. Y.; Lendlein, A. (2016). Ultrasonic cavitation induced shape-memory effect in porous polymer networks. *Macromol. Rapid Comm.*, 37(23), 1897-1903.
- [102] Liu, Y.; Lv, H.; Lan, X.; Leng, J.; Du, S. (2009). Review of electro-active shape-memory polymer composite. *Compos. Sci. Technol.*, 69(13), 2064-2068.
- [103] Ratna, D.; Karger-Kocsis, J. (2008). Recent advances in shape memory polymers and composites: A review. *J. Mater. Sci.*, 43(1), 254-269.
- [104] Dong, Y.; Ni, Q. Q.; Li, L.; Fu, Y. (2014). Novel vapor-grown carbon nanofiber/epoxy shape memory nanocomposites prepared via latex technology. *Mater. Lett.*, 132, 206-209.
- [105] Dong, Y.; Ni, Q. Q.; Fu, Y. (2015). Preparation and characterization of water-borne epoxy shape memory composites containing silica. *Compos. Part A: Appl. S.*, 72, 1-10.
- [106] Dong, Y.; Fu, Y.; Ni, Q. Q. (2015). In-situ grown silica/water-borne epoxy shape memory composite foams prepared without blowing agent addition. *J. Appl. Polym. Sci.*, 132(39).
- [107] Dong, Y.; Xia, H.; Zhu, Y.; Ni, Q. Q.; Fu, Y. (2015) Effect of epoxy-graft-polyoxyethylene octyl phenyl ether on preparation, mechanical properties and triple-shape memory effect of carbon nanotube/water-borne epoxy nanocomposites. *Compos. Sci. Technol.*, 120, 17-25.
- [108] Lu, J.; Arsalan, A.; Dong, Y.; Zhu, Y.; Qian, C.; Wang, R.; et al. (2017). Shape memory

effect and recovery stress property of carbon nanotube/waterborne epoxy nanocomposites investigated via TMA. *Polym. Test.*, 59, 462-469.

[109] Cai, X., Hu, M., Zhang, D., Hu, G., & Yang, J. (2018). Experimental Study on Tunable Electromagnetic Shielding by Microlattice Materials with Organized Microstructures. *Advanced Engineering Materials*, 1700823.

[110] Zhang, L. Q., Yang, B., Teng, J., Lei, J., Yan, D. X., Zhong, G. J., & Li, Z. M. (2017). Tunable electromagnetic interference shielding effectiveness via multilayer assembly of regenerated cellulose as a supporting substrate and carbon nanotubes/polymer as a functional layer. *Journal of Materials Chemistry C*, 5(12), 3130-3138.

[111] Mishra, M., Singh, A. P., Gupta, V., Chandra, A., & Dhawan, S. K. (2016). Tunable EMI shielding effectiveness using new exotic carbon: Polymer composites. *Journal of Alloys and Compounds*, 688, 399-403.

[112] Lu, L., Xing, D., Teh, K. S., Liu, H., Xie, Y., Liu, X., & Tang, Y. (2017). Structural effects in a composite nonwoven fabric on EMI shielding. *Materials & Design*, 120, 354-362.

[113] Li, Y., Shen, B., Yi, D., Zhang, L., Zhai, W., Wei, X., & Zheng, W. (2017). The influence of gradient and sandwich configurations on the electromagnetic interference shielding performance of multilayered thermoplastic polyurethane/graphene composite foams. *Composites Science and Technology*, 138, 209-216.

[114] Zhao, B., & Park, C. B. (2017). Tunable electromagnetic shielding properties of conductive poly (vinylidene fluoride)/Ni chain composite films with negative permittivity. *Journal of Materials Chemistry C*, 5(28), 6954-6961.

[115] Lee, S. H., Yu, S., Shahzad, F., Kim, W. N., Park, C., Hong, S. M., & Koo, C. M. (2017).

Density-tunable lightweight polymer composites with dual-functional ability of efficient EMI shielding and heat dissipation. *Nanoscale*, 9(36), 13432-13440.

[116] Shen, B., Li, Y., Yi, D., Zhai, W., Wei, X., & Zheng, W. (2017). Strong flexible polymer/graphene composite films with 3D saw-tooth folding for enhanced and tunable electromagnetic shielding. *Carbon*, 113, 55-62.

[117] Wang, Y., Cheng, X. D., Song, W. L., Ma, C. J., Bian, X. M., & Chen, M. (2018). Hydro-sensitive sandwich structures for self-tunable smart electromagnetic shielding. *Chemical Engineering Journal*, 344, 342-352.

[118] Chen, Z., Yi, D., Shen, B., Zhang, L., Ma, X., Pang, Y., ... & Zheng, W. (2018). Semi-transparent biomass-derived macroscopic carbon grids for efficient and tunable electromagnetic shielding. *Carbon*, 139, 271-278.

[119] Jin, B., Song, H., Jiang, R., Song, J., Zhao, Q., & Xie, T. (2018). Programming a crystalline shape memory polymer network with thermo-and photo-reversible bonds toward a single-component soft robot. *Science advances*, 4(1), eaao3865.

[120] Yan, Y., Xia, H., Qiu, Y., Xu, Z., & Ni, Q. Q. (2019). Multi-layer graphene oxide coated shape memory polyurethane for adjustable smart switches. *Composites Science and Technology*, 172, 108-116.

[121] Huang, Y., Zhu, M., Pei, Z., Xue, Q., Huang, Y., & Zhi, C. (2016). A shape memory supercapacitor and its application in smart energy storage textiles. *Journal of Materials Chemistry A*, 4(4), 1290-1297.

[122] Zarek, M., Mansour, N., Shapira, S., & Cohn, D. (2017). 4D Printing of Shape Memory - Based Personalized Endoluminal Medical Devices. *Macromolecular rapid communications*, 38(2),

1600628.

[123] Wong, Y. S., Salvekar, A. V., Da Zhuang, K., Liu, H., Birch, W. R., Tay, K. H., ... & Venkatraman, S. S. (2016). Bioabsorbable radiopaque water-responsive shape memory embolization plug for temporary vascular occlusion. *Biomaterials*, 102, 98-106.

[124] Zhao, W., Liu, L., Lan, X., Su, B., Leng, J., & Liu, Y. (2017). Adaptive repair device concept with shape memory polymer. *Smart Materials and Structures*, 26(2), 025027.

[125] Wei, H., Zhang, Q., Yao, Y., Liu, L., Liu, Y., & Leng, J. (2016). Direct-write fabrication of 4D active shape-changing structures based on a shape memory polymer and its nanocomposite. *ACS applied materials & interfaces*, 9(1), 876-883.

Chapter 2

**Multi-layer graphene oxide coated shape
memory polyurethane for adjustable smart
switches**

2 Multi-layer graphene oxide coated shape memory polyurethane for adjustable smart switches

2.1 Introduction

Over past decades, a variety of shape memory materials have been developed including shape memory polymer (SMP) [1-3], shape memory alloy (SMA) [4], shape memory ceramic (SMC) [5], shape memory gel (SMG) [6, 7], shape memory foam [8], shape memory fiber [9, 10], and other specific materials. These materials can be fixed to a desired shape by force, and autonomously recovered through external stimulation such as temperature [11], electricity [12], light [13], pH [14], solvent [15], magnetic field [16], compression [17], and water [18]. This flexible performance has resulted in application of shape memory materials in many industrial fields including sensors [19], actuators [20], smart devices [21], aerospace [22], deployable space structure [23], biomedical devices [24], and textile materials [25].

In these applications, a shape memory switch, which can be used in control systems like in sensor and actuator fields, has shown promise because some shape memory materials, especially SMPs, have reached high shape fixity ratio, shape recovery ratio, flexible structure adjustability, rapid and sensitive response, stable dimension, and/or good durability [11, 26-29]. To date, insufficient attention has resulted in limited research being done regarding adjustable shape memory switches. Here, some relevant work reported in recent years will be introduced. Zhu and Wang prepared one kind of light-actuated two-way reversible shape memory polymer by incorporating polydopamine (PDA) nanospheres into semi-crystalline polymer networks [30]. Because of the strong absorption of PDA to light, this composite showed a reversible angle change of 45° when the light was switched on and off. The speed of angle change could be faster with

stronger light or higher content of PDA. Ambrogi and coworkers synthesized epoxy-based shape-memory liquid crystalline by using carboxylic acid as a curing agent [31]. The controlled degree of liquid crystallinity, and high actuation stress and strain could be achieved by simply changing the aliphatic chain length of the curing agent. Strain actuation could be modulated in the strain range from approximately 60% to 160%. Maiti and coworkers used linear hexamethylene diisocyanate (HMDI) to prepare the polyurethanes (PUs) with different hard segment content (HSC) [32]. The result suggested that the increase of HSC gave decreased shape fixity and increased shape recovery. In summary, the studies described were well done, but the focus was not on the investigation of shape memory switches. With increasing attention of SMPs on shape memory actuation, the development of smart switching devices based on shape memory effect is promising [33, 34].

For SMP switches, high sensitivity, recyclable recovery, good fixity, efficient responding, and flexible adjustability are required to cater for the different demands for sensors and actuators. It is difficult for SMPs to achieve these points by themselves. Presently, there are two basic methods, internal fabrication and external modification, that can possibly be used for adjustable shape memory switches. Internal fabrication can potentially achieve the variation such as glass transition temperature (T_g), melting temperature (T_m), and mechanical properties of SMP by the control of chemical composition like ratio of hard and soft segments [11, 31, 32, 35], or the addition of nano/micro fillers and functional molecules [36-39]. Some researchers have investigated the properties of SMPs by changing internal structures [29, 40, 41]. However, they did not concentrate on the shape memory switching effect, the focus of this research. In our group, we also fabricated many shape memory composites that include carbon nanofiber/epoxy [42], silica/epoxy composite

[43], silica/water-borne epoxy foam [44], and carbon nanotube/waterborne epoxy nanocomposites [45, 46]. Their shape memory effects, including recovery ratio, time, and stress, and other properties like mechanical performance, were investigated in detail. Based on our experience, it is a great challenge to achieve efficient responding, recovery, and adjustability of SMPs because of incomplete shape memory theory and the difficulty in fine adjustability of microstructure and composition. Therefore, external assistance, such as surface treatment and modification, seems to be important to achieve the properties. Thus, the intrinsic property of shape memory will not be lost due to the structural integrity of SMPs. At the same time, fine external modification can be expected to flexibly adjust the property parameters of shape memory materials.

Surface coating is an important approach in industry. By coating modified materials with different properties onto SMP substrates, their response sensitivity, recovery ability, mechanical and thermal properties can be possibly adjusted in a controlled way. To our knowledge, few studies concerning the coating of shape memory materials have been undertaken. It will be of great significance to develop coating modified SMPs for adjustable shape memory switches.

In this chapter, shape memory polyurethane (SMPU), one type of thermoplastic polymer consisting of hard and soft segments, was introduced as a substrate. It was selected because of its easy processing, excellent flexibility, and environmental friendliness. The shape memory of this SMPU is stimulated and driven by temperature, with glass transition temperature determining the shape switching of the SMPU. Then, graphene oxide (GO), obtained from the oxidation of flaky graphite, was selected as the coating layer of the SMPU substrate due to its unique two-dimensional structure. The presence of the GO layer ensured that the SMPU and heat source are isolated, through which, the recovery time, ratio, and force of the SMPU could potentially be

controllably adjusted.

In this study, through a multi-dipping approach, we fabricated multi-layer GO coated SMPU (MLGO@SMPU) for an adjustable shape memory switch. The morphology and structure of this MLGO@SMPU was firstly analyzed to better understand the effect of GO on shape memory properties. Because of the hydrophilic property and multi-layer coating structure of GO, water resistance and adhesive tests were also carried out. Finally, we evaluated the recovery ratio, time and force, and fixity ratio of these MLGO@SMPU specimens. It was expected that this novel and straightforward approach of dipping coating of SMP for fabrication of adjustable recovery ratio, time and force, could lead to new insights for application of shape memory materials as switching devices in sensor and actuator fields.

2.2 Experiment

2.2.1 Materials

Graphite powder (7-10 μm), potassium permanganate (KMnO_4), sodium nitrate (NaNO_3), concentrated sulfuric acid (H_2SO_4 , 98%), hydrogen peroxide (H_2O_2 , 30%), and dimethyl formamide (DMF) were all purchased from Wako Pure Chemical Industries Ltd, Japan. SMPU pellets (MM6520) were obtained from SMP technologies Company, Japan. All chemicals were used without further purification.

2.2.2 Preparation of GO

GO was prepared by modification of Hummers' method [47]. 10 g graphite and 0.8 g NaNO_3 powder were added in batches into 230 ml concentrated H_2SO_4 solution contained in a beaker while being stirred magnetically in an ice bath. After uniform dispersion, 30 g KMnO_4 was slowly added to the mixture within 0.5 h. After stirring for another half an hour in the ice bath, the beaker

was transferred into an oil bath and subjected to magnetic stirring at 40 °C for 2 h. A brownish paste was obtained. 300 ml distilled water was gently poured in and continually stirred for 0.5 h. After cooling down to room temperature, adequate H₂O₂ was added to the beaker, turning the solution bright yellow. The resulting solution was then filtered and repeatedly washed with distilled water. Finally, the obtained GO was dried at 60 °C in a vacuum dryer for 48 h.

2.2.3 Preparation of SMPU film

The SMPU pellets used in this research were obtained by polyaddition of linear chain diisocyanate and polyol, as illustrated in **Fig 2.1**. The SMPU has a glass transition temperature (T_g) of ~60 °C and melting point (T_m) of ~175 °C, as studied in our previous work [48-51]. For preparation of SMPU film, 5.0 g SMPU pellets were dissolved in 5.0 ml DMF solvent to prepare a high concentration of SMPU/DMF solution. Then, the viscous solution was coated onto a teflon substrate by using an automatic film applicator (PI-1210, Tester Sangyo Co. Ltd., Japan), followed by drying at 80 °C for 5 days to remove residual DMF. Finally, the obtained SMPU film was adjusted to approximately 0.2 mm thickness by hot pressing at 90 °C.

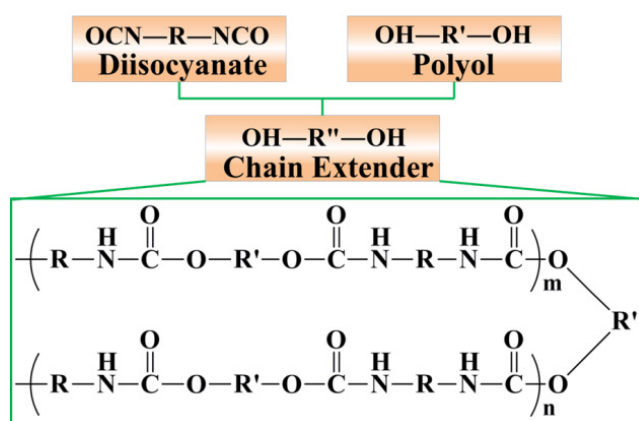


Fig. 2.1 Structure representation of SMPU

2.2.4 Fabrication of MLGO@SMPU

The MLGO@SMPU was fabricated by multiple dipping of SMPU precursor in concentrated

GO aqueous solution, as shown in **Fig. 2.2**. For details, the as-obtained SMPU film was fully dipped into 0.005 g/ml GO aqueous solution, which had been subjected to sonication for 2 h before, and then suspended in air to remove extra GO solution. The SMPU film coated with GO was then gently transferred in a dryer and kept at 50 °C for 24 h. The obtained GO@SMPU was labeled as 1 layer. Likewise, through repeated dipping and drying procedures, different layers of MLGO@SMPU ranging from 2 to 5 layers were fabricated. Finally, all MLGO@SMPU specimens were subjected to hot pressing at 90 °C for 24 h for sufficient contact between GO and SMPU layers.

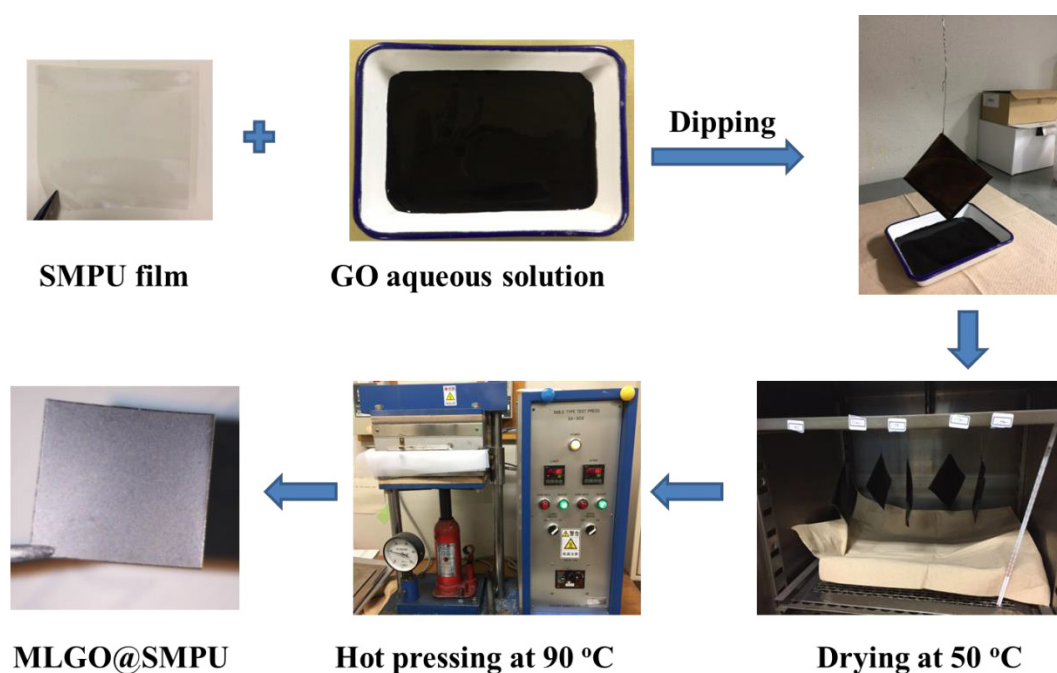


Fig. 2.2 Schematic representation of fabrication of MLGO@SMPU

2.2.5 Characterization

Surface morphologies of MLGO@SMPU specimens were observed by using field emission scanning electron microscopy (FE-SEM, Hitachi S-5000, 20 kV). Their cross sections were investigated by optical microscope (VHX-1000SP (1539), KEYENCE) with a real zoom lens from 500 to 5000 times. The crystal structures of the samples were characterized by X Ray Diffraction

(XRD, MiniFlex300, Japan) scanning in the range of $2\theta = 5^{\circ}$ - 40° . The static tensile measurements of the samples were carried out via a Tensilon Tensile Tester (RTC1250A, A&D Co.) using a tensile speed of 5 mm/min at room temperature. The Fourier transform infrared (FTIR) spectra of the MLGO@SMPU were measured on a Nicolet 5700 attenuated total reflection Fourier transform infrared (ATR-FTIR) instrument (Thermo Electron Corp., USA) with a resolution of 4 cm^{-1} . The T_g of SMPU was measured by dynamic mechanical analysis (DMA) on a DVA-225 instrument (IT Keisoku Seigyo Co. Ltd., Japan).

Water resistance tests of the MLGO@SMPU samples were conducted by their standing (24 h) or sonication (3 min) in distilled water. An adhesive force test of the GO layer on the SMPU film was evaluated by the adhesion and exfoliation of normal adhesive tape to the GO coating on the surface of the MLGO@SMPU film. 10 mm * 10 mm MLGO@SMPU film was slide-cut lightly on the surface into 4 * 4 squares to separate each part of GO. Other evaluations concerning shape memory property will be introduced in the results and discussion section that follows.

2.3 Results and discussion

2.3.1 Morphology and structure analysis

The surface morphology of MLGO@SMPU was presented in **Fig 2.3a**. GO sheets ranging in size from 5-15 μm were compacted together. This avoided the drop of GO sheets from the surface of the MLGO@SMPU. Then, to directly observe the inter-layer structure of the GO layers, we investigated the surface morphology at the fracturing spot for 3-layer MLGO@SMPU caused by external impact failure. As shown in **Fig 2.3b**, the first, second and third GO layers could be seen separately. Between the 2nd and 3rd layers of GO, external impact resulted in obvious exfoliation, but a good fusion area was still observable, and attributed to the hot compression for

MLGO@SMPU.

Because the layer structures of these MLGO@SMPU specimens have a direct impact on shape memory effect, their morphologies were then observed by optical microscope in cross section. As shown in **Fig. 2.3c**, multi-layer GO, stacked together in parallel, uniformly covers the surface of the SMPU substrate. Owing to natural dipping, it can also be seen there is a loose structure between the GO layer and SMPU. However, compact stacking of the GO layers onto the SMPU surface was formed following hot compression at 90 °C, as indicated in **Fig. 2.3d**. Moreover, the thickness of the MLGO@SMPU specimens increased with increased GO layers (**Tab. 2.1**). Measurement indicated that the thickness of the single-sided GO layer varied from 1.75 μm of 1-layer GO to 12.10 μm of 5-layer GO, as listed in **Tab. 2.1**.

Fig. 2.3e presents the XRD patterns of the MLGO@SMPUs with 1-layer, 3-layer and 5-layer GO. The peaks around 11.5° are ascribed to the GO layers in MLGO@SMPUs. Since large-scale and one-pot preparation of GO resulted in insufficient oxidation of graphite, the peak position of the GO in XRD patterns shows a larger value than was previously reported (around 10°) [52]. As seen from the peak intensity of GO, the amount of GO grows with increase in dipping times. A wide peak, located at approximately 20°, demonstrates the amorphous property of the SMPU polymer.

Fig. 2.3f exhibits the FTIR spectra of the MLGO@SMPUs with 1-, 3-, and 5-layer GO. The two peaks at 2853 cm⁻¹ and 2924 cm⁻¹ resulted from the C-H groups in the GO component. These MLGO@SMPU specimens gave wide peaks ranging from 2162 cm⁻¹ to 3686 cm⁻¹. These are attributed to the OH- groups of GO, which were obtained from the oxidation of graphite. It can also be clearly seen that the wide peak area increases with the increase of GO layer. This indicates

increased GO amount with more dipping times. Through experimental measurement, the loading ratios of the MLGO@SMPUs with different layers were calculated and summarized in **Tab. 2.1**.

1-layer MLGO@SMPU has a GO loading ratio of 0.142 wt%, while the loading ratio of 5-layer MLGO@SMPU could reach a value of 1.096 wt%.

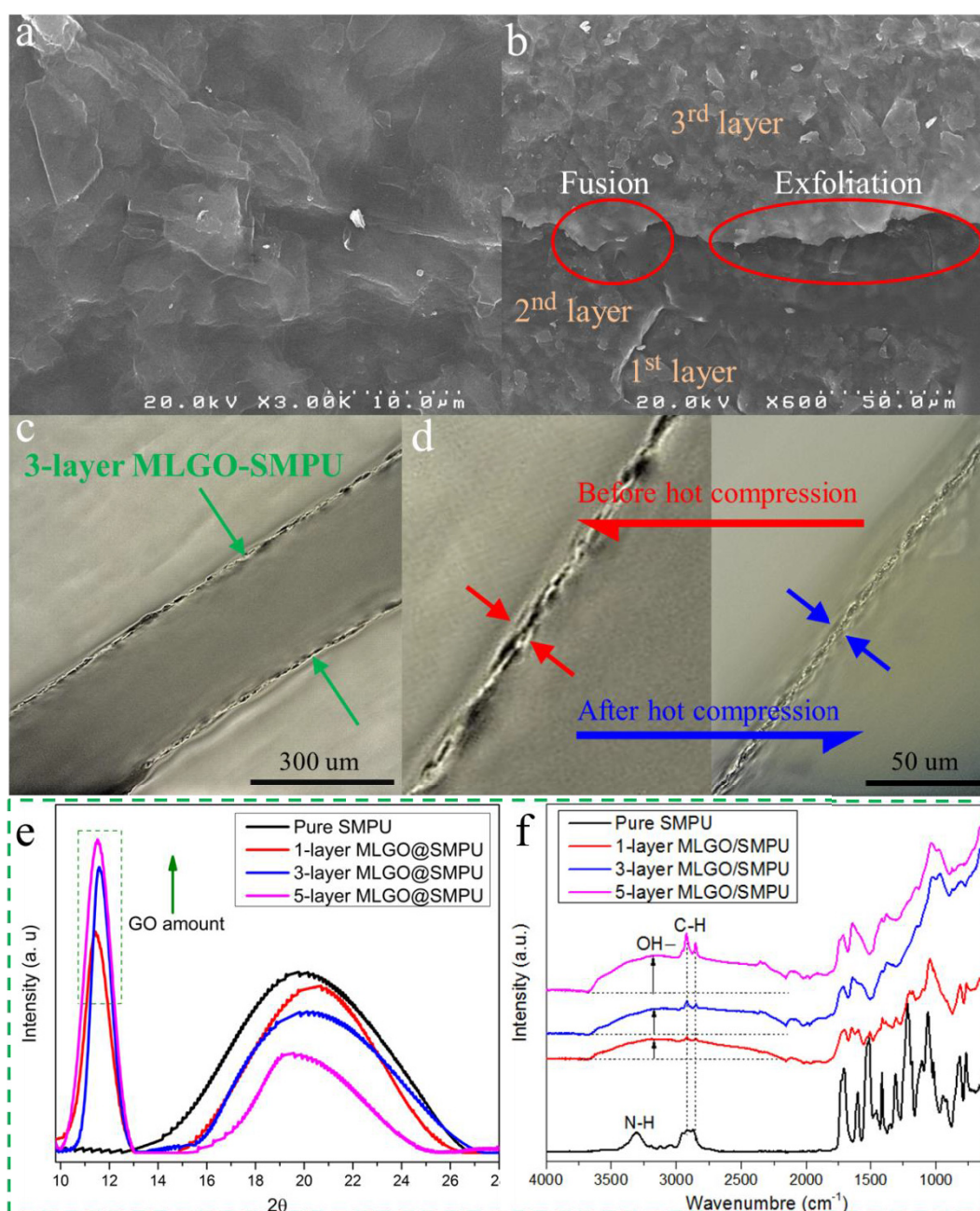


Fig. 2.3 (a) The surface morphology of a 3-layer MLGO@SMPU specimen; (b) The morphology at the fracturing spot of a 3-layer MLGO@SMPU specimen; (c, d) The cross sections of a 3-layer MLGO@SMPU specimen before and after hot compression at 90 °C; (e) XRD patterns, and (f)

FTIR spectra of the MLGO@SMPU specimens with 1-layer, 3-layer and 5-layer GO

Tab. 2.1 Film thickness, GO thickness, and GO loading ratio of the MLGO@SMPU specimens with different GO layers

Specimens	Film thickness	GO thickness*	GO loading ratio
Pure SMPU	200.3 μm	-	-
1 layer	203.8 μm	1.75 μm	0.142 wt%
2 layers	208.4 μm	4.05 μm	0.369 wt%
3 layers	213.6 μm	6.65 μm	0.605 wt%
4 layers	219.1 μm	9.40 μm	0.857 wt%
5 layers	224.5 μm	12.10 μm	1.096 wt%
* Refer to the thickness of the GO layer for single-sided MLGO@SMPU			

2.3.2 Mechanical properties

Mechanical behavior of the MLGO@SMPU was then analyzed. **Fig. 2.4a** shows the strain-stress curves of the MLGO@SMPU specimens with different GO layers. All specimens including pure SMPU revealed similar mechanical behavior, in which the substrate SMPU plays a vital role. After undergoing initial elastic deformation, which required the stretching stress of at least 50 MPa, they then showed a plastic deformation area, which made the MLGO@SMPU specimens clearly stretch over 150 % in strain. The mechanical stretching process for 3-layer MLGO@SMPU is shown in **Fig. 2.4b**. It can be seen that the GO layer on the surface of the SMPU substrate generated multiple fractures during stretching. The stress increased with strain until approximately 400 %. After that, the MLGO@SMPU specimens started to break in the strain range from 400 % to 432 %. The comparison before and after breaking is shown in **Fig. 2.4c**.

Considering that the continuity of GO layers disappeared after the initial stretching process, the value difference in maximum strain and stress, as can be seen from **Fig. 2.4a**, may be attributed to the statistical scattering of the as-prepared SMPU specimens. **Fig. 2.4d** shows the strain-stress curves up to the strain of 20 %. It can be seen that the increase of GO layer resulted in higher stress demand in the initial stretching stage. This indicates that below the strain of approximately 6 %, the coating of GO onto the SMPU substrate could enhance mechanical tensile strength of the MLGO@SMPU.

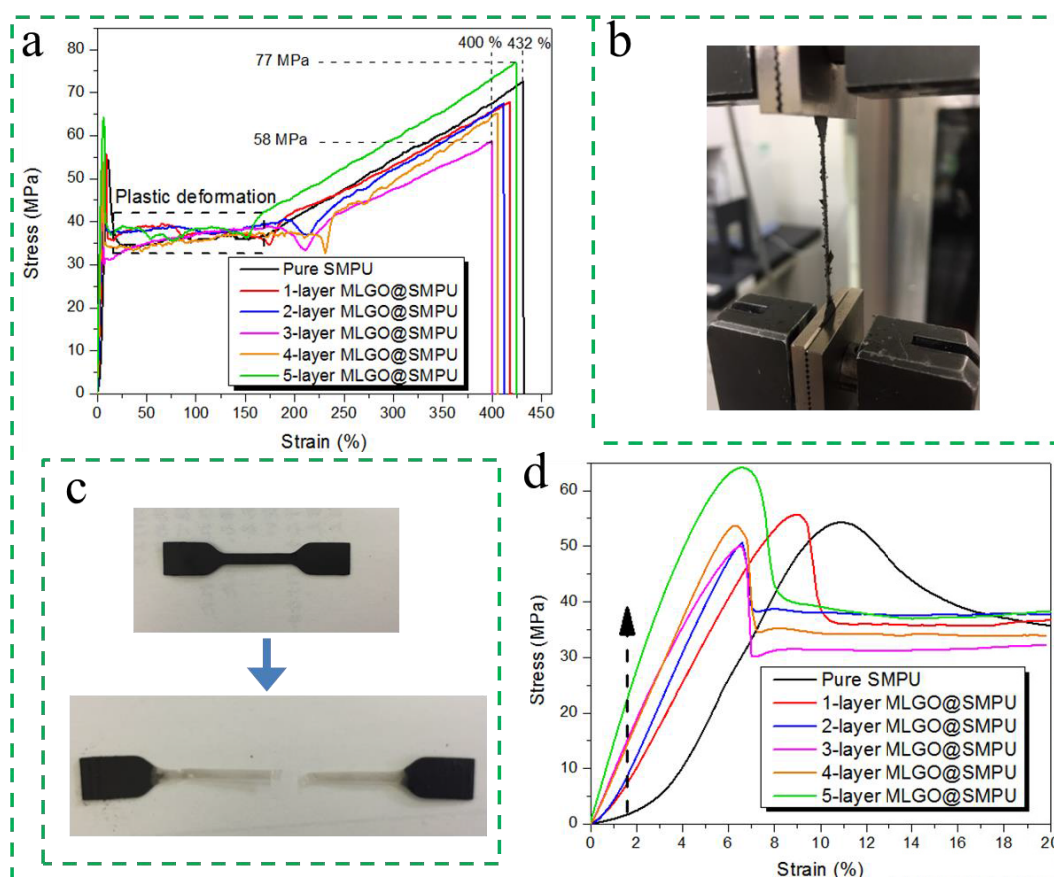


Fig. 2.4 (a) Strain-stress curves of the MLGO@SMPUs with different GO layers; (b) The observation during the mechanical stretching of 3-layer MLGO@SMPU; (c) The comparison before and after the stretching of 3-layer MLGO@SMPU; (d) Strain-stress curves up to the strain of 20 %.

2.3.3 Water resistance of GO layer

It is known that GO is vulnerable to polar water molecules, and well-oxidized GO can be stably dispersed in water media. Here, we investigated the water resistance of GO to water media, as shown in **Fig. 2.5**. Firstly, a piece of 5-layer MLGO@SMPU was treated by standing in distilled water for 24 h. The specimen is shown in **Fig. 2.5a** and **2.5b** before and after this process. After drying the treated specimen for 3 days, the weight loss content of the specimen was approximately 1.3 wt%, which suggests that the holding ratio of the SMPU substrate for GO layers could be maintained above 98 wt%. Then, similarly, a piece of 5-layer MLGO@SMPU was treated by sonicating in distilled water for 3 mins. The solution, before and after treating the specimen, was shown in **Fig. 2.5a**. After drying the sonicated specimen for 3 days, the weight loss content of the specimen was approximately 93.6 wt%. As shown in **Fig. 2.5c**, the sonication treatment achieved an almost complete drop of the GO layers from the SMPU surface. This is because of the separation of the GO sheets, which were inter-connected by weak van der Waals force. Therefore, we conclude that this MLGO@SMPU is stable in standing water within 24 h, and vulnerable after being subjected to mechanical vibration like ultra-sonication.

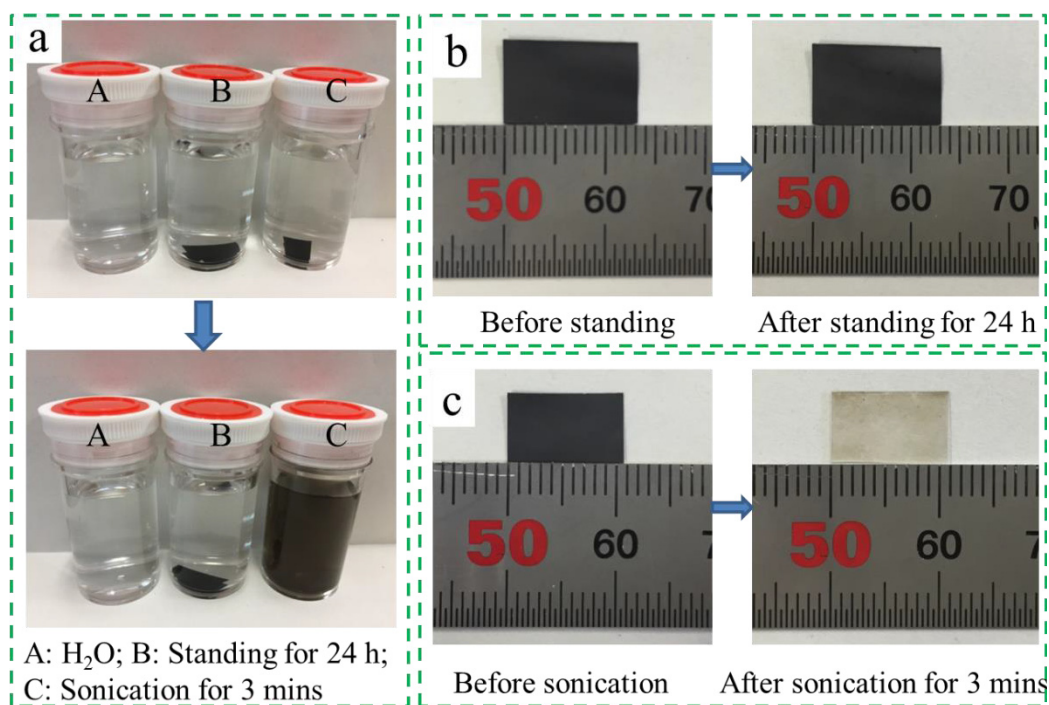


Fig. 2.5 Water resistance test. (a) The comparison before and after different treatments (A: pure H₂O, B: standing for 24 h, C: sonication for 3 mins) for 5-layer MLGO@SMPU; (b) 5-layer MLGO@SMPU before and after standing in distilled water for 24 h; (c) 5-layer MLGO@SMPU before and after sonicating in distilled water for 3 mins.

2.3.4 Adhesive properties of GO layer

To evaluate the adhesive performance of the GO layer, an adhesive force test was conducted by repeated adhesion and exfoliation of normal transparent adhesive tape for the surface of MLGO@SMPU specimens. The pictures of the adhesive tapes, which were repeatedly adhered and peeled off from the MLGO@SMPU surface, are presented in **Fig. 2.6**. As can be clearly seen, much GO remained on the adhesive tape after peeling. With the increase of GO layers, the peeling times which were required to remove the GO layers neatly and thoroughly from the SMPU, increased as well. For example, more than 5 times were needed to almost completely remove the GO layers from the SMPU substrate. For 1-layer MLGO@SMPU, little GO remained on the tape after peeling, which suggests tight adhesion of the 1st layer of GO with SMPU substrate. For

2-layer MLGO@SMPU, after the 1st time of peeling, it became difficult to adhere more GO from the MLGO@SMPU. This also indicates the relatively good adhesion of the 1st layer of GO with the SMPU surface. For MLGO@SMPU specimens having more than 2 layers of GO, multiple peeling was needed, which suggests weak interaction force between GO layers.

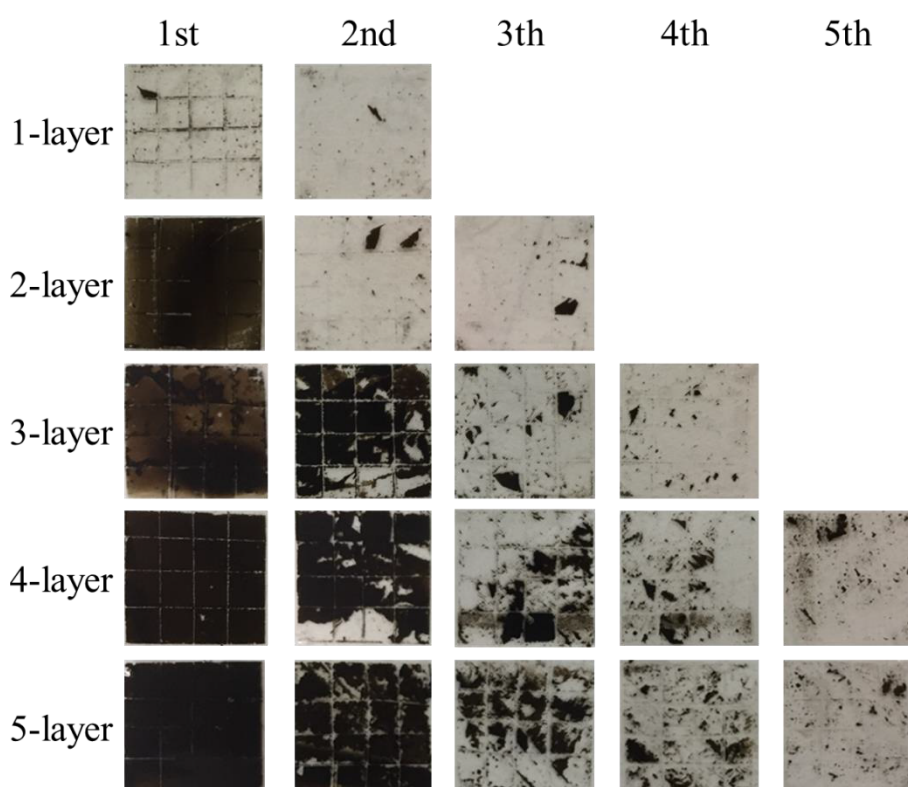


Fig. 2.6. The pictures of the adhesive tapes after they were peeled off from the surfaces of the MLGO@SMPU specimens with different GO layers. For this adhesive force test, the surfaces of 10 mm * 10 mm MLGO@SMPU films were all slide-cut lightly into 4 * 4 squares to separate each part of GO before adhering the adhesive tape onto the MLGO@SMPU.

2.3.5 Shape memory recovery

Angle recovery performance for shape memory MLGO@SMPUs with different GO layers was evaluated using homemade apparatus shown in **Fig 2.7a** and **2.7b**. For initial conditions, a 30 mm * 6 mm (length * width) strip-type MLGO@SMPU specimen was pre-heated at 80 °C, and equally folded in half to a perpendicular shape, followed by cooling and fixing at low temperature.

Then, the specimen was placed between an aluminum (Al) block and plate, beneath which was a heater, as illustrated in **Fig 2.7a**. The temperature of the heater was set at 80 °C. Because of thermal conductivity of the Al plate and block, heat transfer made the specimen respond to heat and recover. The protractor, which was aligned to the specimen, recorded the angle recovery of the MLGO@SMPU stripe.

The recovery angle of the MLGO@SMPU specimens is presented in **Fig 2.7c**. As layers of GO increased, the MLGO@SMPU stripe, whose initial status was vertical (90°), showed a decreased recovery angle. Pure SMPU has a recovery angle of 97°, while 5-layer MLGO@SMPU has a recovery angle decreasing to 75°. Then, based on the angle change, the angle recovery ratio was calculated by dividing the initial 90° using the changed angle. **Fig 2.7d** presents corresponding angle recovery ratio and time. It can be seen that the increase of GO layer led to a decreased angle recovery ratio, and increased angle recovery time. The angle recovery ratio of 5-layer MLGO@SMPU is about 83.2 %, and the corresponding angle recovery time needs about 7.6 s. The separation of insulating GO layers means that the internal SMPU phase of the MLGO@SMPU, which contributes to shape memory effect, has a slower response time to heat compared with pure SMPU. In this way, the recovery angle of the MLGO@SMPU could be adjusted by controlling the coating thickness of the GO layer. The application of this MLGO@SMPU could possibly be expected in temperature-responding shape memory switching devices which have the demand of different recovery angles.

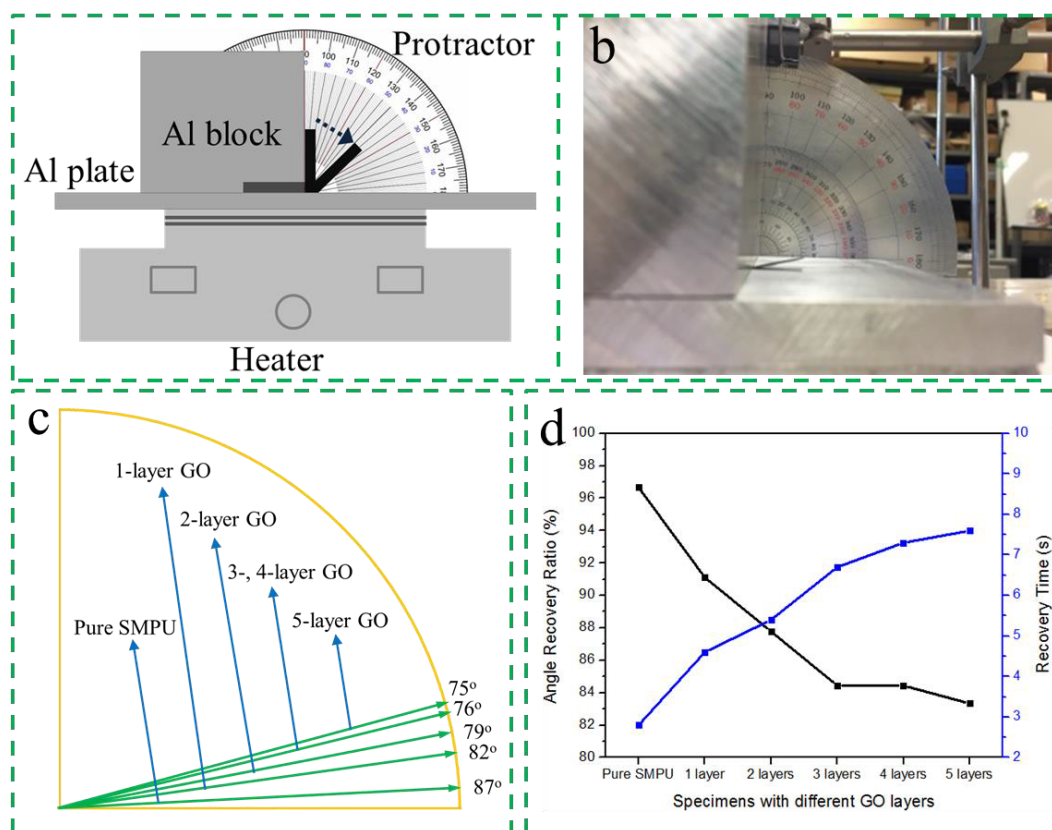


Fig. 2.7 The angle recovery of the MLGO@SMPU specimens with different GO layers. (a) The evaluation schematic for shape memory recovery; (b) The evaluation apparatus for shape memory recovery; (c) The recovery angles of MLGO@SMPU specimens; (d) The angle recovery ratio and time of different MLGO@SMPU specimens.

2.3.6 Shape memory switching evaluation

To better understand the relation between the bending recovery force of MLGO@SMPU and the coating layers of GO, a simple apparatus was designed as illustrated in **Fig. 2.8a**. Except for a suspending glass slide, the other parts of this apparatus are similar to the one that was used in measuring the angle recovery ratio. When the MLGO@SMPU recovers back from the initial 90° position, it will get bumped with the glass slide, and then lift the glass slide up to a balanced status, as seen in **Fig. 2.8b**. The horizontal distance from the bottom end of the lifted glass slide to its original position, expressed as lifting distance, was used as an indicator for evaluating the bending

recovery ability of the MLGO@SMPU specimens.

As presented in **Fig. 2.8c**, the lifting distance of different MLGO@SMPU specimens was summarized. It can be seen that, the lifting distance, which was supported by the bending recovery force of the MLGO@SMPU specimen, increased with more coating layers of GO. Pure SMPU had a lifting distance of 2.2 mm, and the 5-layer MLGO@SMPU could increase the lifting distance up to 12.9 mm. This indicates that the recovery force of the MLGO@SMPU could increase with increased GO layers. The reason for that is related to the bending of the MLGO@SMPU at the bending point (i.e., the position folded in half). Because this bending is a small deformation behavior including simultaneous stretching and compression, the mechanical change of the MLGO@SMPU was considered in low strain range. As can be seen from **Fig. 2.4d**, in low strain, the increase of the GO layer enhanced the mechanical strength of the MLGO@SMPU. Thus, the reinforced MLGO@SMPU could still keep its original dimension even in higher temperature status, and this led to a larger lifting distance compared with the pure SMPU, which turned soft with elevated temperature.

To further know the bending recovery force of different MLGO@SMPU specimens, the force conditions of the glass slide were analyzed under steady lifting status, as illustrated in **Fig. 2.8d**. In the direction perpendicular to the glass surface, the glass slide received its own gravity, and the support from the bending recovery force of the MLGO@SMPU, which gave it a balanced status. The bending recovery force of the MLGO@SMPU was calculated based on the moment balance of the glass slide under balanced lifting status. The calculated result was presented in **Fig. 2.8e**. It can be seen that the increase of the GO layer enhanced the bending recovery force of the MLGO@SMPU from the 1.9 mN of 1-layer GO to the 18.3 mN of 5-layer GO. This recovery

force adjustable MLGO@SMPU can be expected to meet the demand of the shape memory switching devices which need controllable actuating force under different situations.

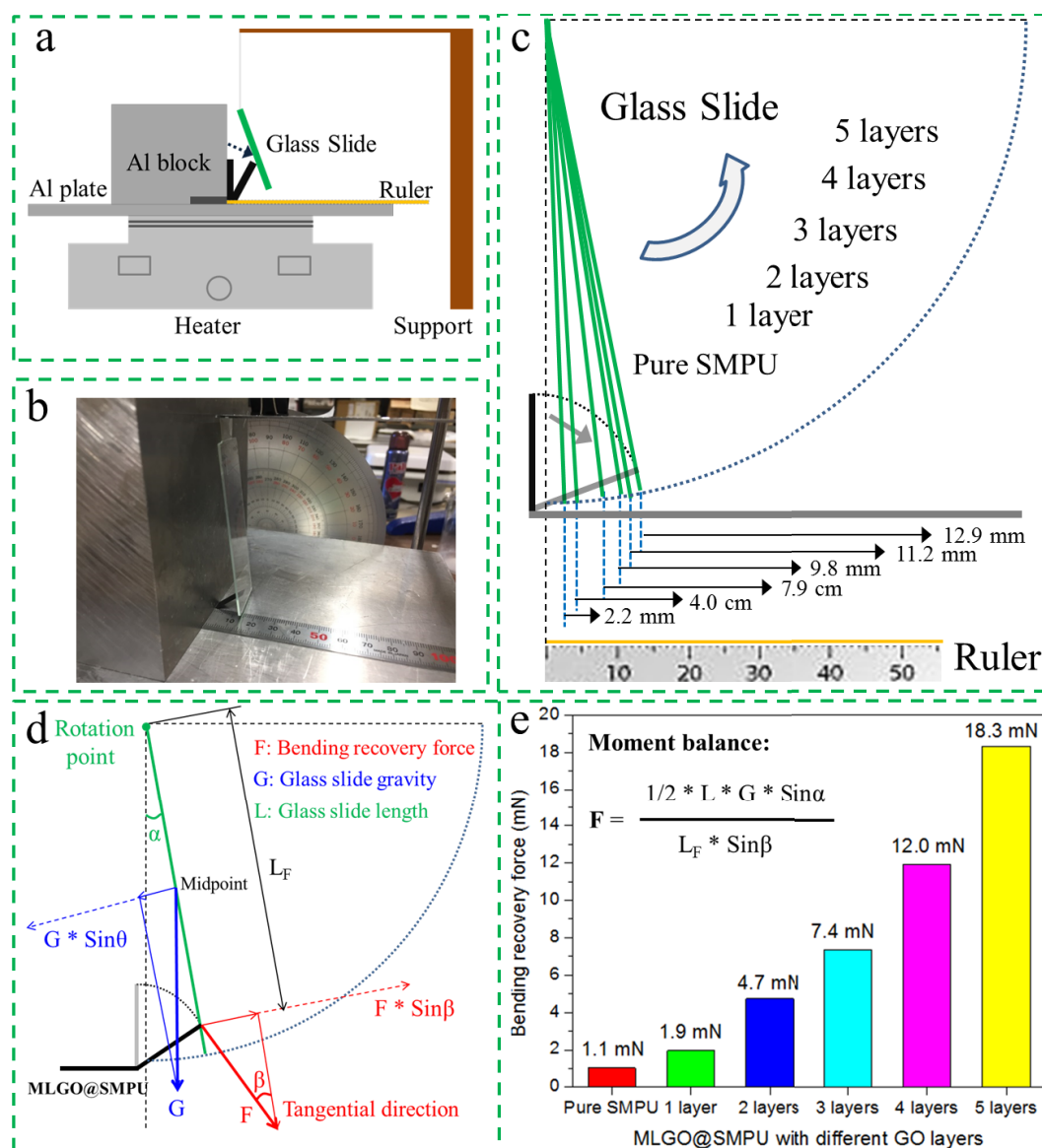


Fig. 2.8 The recovery force evaluation of shape memory MLGO@SMPU specimens, all specimens are 30 mm * 6 mm (length * width), and the thickness refers to **Tab. 2.1**. (a) The evaluation schematic for bending recovery force; (b) Evaluation apparatus for bending recovery force, one piece of glass slide with the size of 76 mm * 26 mm * 1 mm (length * width * thickness) and the weight of approximately 4.8 g was vertically suspended to evaluate the lifting ability of the MLGO@SMPU. In initial state, the vertical height to bottom Al plate, and the horizontal

distance to adjacent Al block of the glass slide were both set as 2.0 mm; (c) The horizontal distance to initial position of the lifted glass slide for different MLGO@SMPU specimens; (d) The force analysis of the glass slide under final balanced lifting status; (e) The calculated bending recovery force based on the moment balance of the lifted glass slide under final balanced status.

2.3.7 Angle fixity ratio of shape memory

The angle fixity ratios of the MLGO@SMPU specimens were measured by the angle change using the apparatus presented in **Fig. 2.9a**. The MLGO@SMPU stripe was folded in half, and then fixed to a vertical shape at low temperature. The angle fixity (af) ratio was calculated by $R_{af} = (1 - \theta/90^\circ) * 100 \%$, where R_{af} and θ are the angle fixity ratio, and the angle bended back from initial right angle, respectively. After 5 days, the angle change was measured and the result is presented in **Fig. 2.9b**. With increasing GO layers, the angle fixity ratio of the MLGO@SMPU showed a decreasing trend. In the case of the 5-layer MLGO@SMPU, the angle fixity ratio dropped to 83.3 %. This is because the GO component does not have a shape memory effect, and consequently the folded GO layer at the bending point of the fixed MLGO@SMPU specimen exhibited a gradual “unfolding” phenomenon. The more GO layers, the more evident unfolding the MLGO@SMPU shows. Therefore, we can conclude that, in order to get the shape memory switching devices, which need good angle fixity ratio, the layer thickness of the GO component on the SMPU substrate cannot be that thick. An angle fixity ratio above 90 % requires fewer than 4 layers of GO.

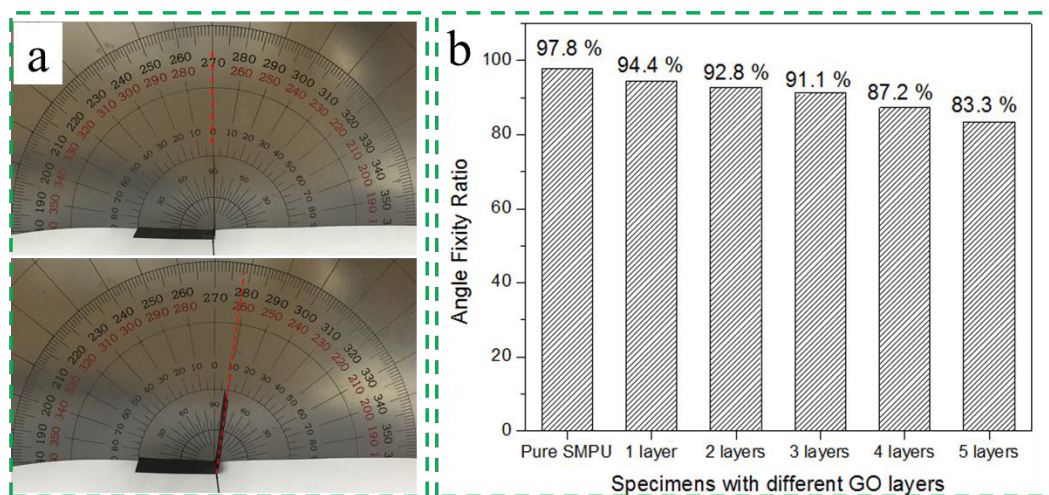


Fig. 2.9 The angle fixity ratios of the MLGO@SMPU specimens with 30 mm * 6 mm (length * width). (a) Evaluation apparatus for measuring the angle fixity ratio. The MLGO@SMPU specimens, which were pre-folded in half at 80 °C, were cool-fixed and aligned in front of a protractor. After 5 days, according to the measured angle change, the angle fixity ratios of the MLGO@SMPU specimens were calculated; (b) The angle fixity ratios of the MLGO@SMPU specimens with different GO layers.

2.4. Conclusions

MLGO@SMPU composites with different GO layers were fabricated by multiple dipping in GO aqueous solution for adjustable shape memory switches. Morphology observation showed that multi-layer graphene oxide was evenly covered onto the surface of the SMPU substrate. Strain stress curves indicated that the increase of GO layers improved the mechanical strength of these MLGO@SMPU composites in the initial stretching stage. Water resistance testing suggested that the MLGO@SMPU could maintain integrity in water within 24 h, but the GO layer would fall off after being subjected to sonication treatment. Adhesive force testing showed that the first GO layer attached well onto the SMPU surface. However, more GO layers were more easily peeled off from the SMPU substrate. This was attributed to weak intermolecular forces between GO layers. Finally,

the shape memory performances for these MLGO@SMPU composites were evaluated using homemade evaluation apparatus. It was concluded that with the increase of GO layers, the MLGO@SMPU showed a decreased angle recovery ratio, slower recovery time, larger recovery force, and decreased angle fixity ratio.

This work aims to share the fundamental basis and experience of coating research of shape memory materials. It is expected that this novel approach of dipping coating of shape memory materials for adjustable recovery ratio, time, and force, could be applied in the field of smart switching devices. In the following research, the switching ability of the SMPU, which is driven by shape memory effect, will be utilized for fixing and recovery actuation in thickness for adjustable EM shielding.

REFERENCES

- [1] Liu, C.; Qin, H.; Mather, P. T. Review of progress in shape-memory polymers. *J. Mater. Chem.* 2007, 17(16), 1543-1558.
- [2] Behl, M.; Razzaq, M. Y.; Lendlein, A. Multifunctional shape memory polymers. *Adv. Mater.* 2010, 22(31), 3388-3410.
- [3] Chan, B. Q. Y.; Low, Z. W. K.; Heng, S. J. W.; Chan, S. Y.; Owh, C.; Loh, X. J. Recent advances in shape memory soft materials for biomedical applications. *ACS Appl. Mater. Interfaces*, 2016, 8(16), 10070-10087.
- [4] Jani, J. M.; Leary, M.; Subic, A.; Gibson, M. A. A review of shape memory alloy research, applications and opportunities. *Mater. Design (1980-2015)*, 2014, 56, 1078-1113.
- [5] Lai, A.; Du, Z.; Gan, C. L.; Schuh, C. A. Shape memory and superelastic ceramics at small scales. *Science*, 2013, 341(6153), 1505-1508.
- [6] Lu, W.; Le, X.; Zhang, J.; Huang, Y.; Chen, T. Supramolecular shape memory hydrogels: A new bridge between stimuli-responsive polymers and supramolecular chemistry. *Chem. Soc. Rev.* 2017, 46(5), 1284-1294.
- [7] Löwenberg, C.; Balk, M.; Wischke, C.; Behl, M.; Lendlein, A. Shape-memory hydrogels: Evolution of structural principles to enable shape switching of hydrophilic polymer networks. *Accounts Chem. Res.* 2017, 50(4), 723-732.
- [8] Li, G.; Uppu, N. Shape memory polymer based self-healing syntactic foam: 3-D confined thermomechanical characterization. *Compos. Sci. Technol.* 2010, 70(9), 1419-1427.
- [9] Deng, J.; Zhang, Y.; Zhao, Y.; Chen, P.; Cheng, X.; Peng, H. A shape-memory supercapacitor fiber. *Angew. Chem. Int. Edit.* 2015, 54(51), 15419-15423.

- [10] Zhong, J.; Meng, J.; Yang, Z.; Poulin, P.; Koratkar, N. Shape memory fiber supercapacitors. *Nano Energy*, 2015, 17, 330-338.
- [11] Huang, M.; Zheng, L.; Wang, L.; Dong, X.; Gao, X.; Li, C.; Wang, D. Double crystalline multiblock copolymers with controlling microstructure for high shape memory fixity and recovery. *ACS Appl. Mater. Interfaces*, 2017, 9(35), 30046-30055.
- [12] Xie, Y.; Meng, Y.; Wang, W.; Zhang, E.; Leng, J.; Pei, Q. Bistable and reconfigurable photonic crystals electroactive shape memory polymer nanocomposite for ink free rewritable paper. *Adv. Funct. Mater.* 2018, 1802430.
- [13] Du, L.; Xu, Z.; Fan, C.; Xiang, G.; Yang, K.; Wang, Y. A fascinating metallo supramolecular polymer network with thermal/magnetic/light responsive shape memory effects anchored by Fe_3O_4 nanoparticles. *Macromolecules* 2018, 51(3), 705-715.
- [14] Le, X.; Zhang, Y.; Lu, W.; Wang, L.; Zheng, J.; Ali, I.; et al. Novel anisotropic hydrogel with integrated self-deformation and controllable shape memory effect. *Macromol. Rapid Comm.* 2018, 39(9), 1800019.
- [15] Huang, J.; Liao, J.; Wang, T.; Sun, W.; Tong, Z; Super strong dopamine hydrogels with shape memory and bioinspired actuating behaviours modulated by solvent exchange. *Soft Matter* 2018, 14(13), 2500-2507.
- [16] Razzaq, M. Y.; Behl, M.; Kratz, K., Lendlein, A. Multifunctional hybrid nanocomposites with magnetically controlled reversible shape-memory effect. *Adv. Mater.* 2013. 25(40), 5730-5733.
- [17] Fang, Y.; Ni, Y.; Leo, S. Y.; Taylor, C.; Basile, V.; Jiang, P; Reconfigurable photonic crystals enabled by pressure-responsive shape-memory polymers. *Nat. Commun.* 2015, 6, 7416.

- [18] Fang, Z.; Kuang, Y.; Zhou, P.; Ming, S.; Zhu, P.; Liu, Y.; et al. Programmable shape recovery process of water-responsive shape-memory poly (vinyl alcohol) by wettability contrast strategy. *ACS Appl. Mater. Interfaces* 2017, 9(6), 5495-5502.
- [19] Li, L.; Shi, P.; Hua, L.; An, J.; Gong, Y.; Chen, R.; et al. Design of a wearable and shape-memory fibriform sensor for the detection of multimodal deformation. *Nanoscale*, 2018, 10(1), 118-123.
- [20] Song, S. H.; Lee, J. Y.; Rodrigue, H.; Choi, I. S.; Kang, Y. J.; Ahn, S. H. 35 Hz shape memory alloy actuator with bending-twisting mode. *Sci. Rep.* 2016, 6, 21118.
- [21] Hassani, F. A.; Peh, W. Y. X.; Gammad, G. G. L.; Mogan, R. P.; Ng, T. K.; Kuo, T. L. C.; et al. A 3D printed implantable device for voiding the bladder using shape memory alloy (SMA) actuators. *Adv. Sci.* 2017, 4(11), 1700143.
- [22] Liu, Y.; Du, H.; Liu, L.; Leng, J. Shape memory polymers and their composites in aerospace applications: A review. *Smart Mater. Struct.* 2014, 23, 023001.
- [23] Lan, X.; Liu, Y.; Lv, H.; Wang, X.; Leng, J.; Du, S. Fiber reinforced shape-memory polymer composite and its application in a deployable hinge. *Smart Mater. Struct.* 2009, 18(2), 024002.
- [24] Biswas, A.; Singh, A. P.; Rana, D.; Aswal, V. K.; Maiti, P. Biodegradable toughened nanohybrid shape memory polymer for smart biomedical applications. *Nanoscale* 2018, 10(21), 9917-9934.
- [25] Thakur, S. Shape memory polymers for smart textile applications. In *Textiles for Advanced Applications*. InTech. 2017.
- [26] Wang, W.; Shen, D.; Li, X.; Yao, Y.; Lin, J.; Wang, A.; et al. Light-driven shape-memory

- porous films with precisely controlled dimensions. *Angew. Chem.* 2018, 130(8), 2161-2165.
- [27] Riccardi, L.; Naso, D.; Janocha, H.; & Turchiano, B. A precise positioning actuator based on feedback-controlled magnetic shape memory alloys. *Mechatronics*, 2012, 22(5), 568-576.
- [28] Ur Rehman, H.; Chen, Y.; Hedenqvist, M. S.; Li, H.; Xue, W.; Guo, Y. L.; et al. Self-healing shape memory PUPCL copolymer with high cycle life. *Adv. Funct. Mater.* 2018, 28(7), 1704109.
- [29] Meng, H.; Li, G. A review of stimuli-responsive shape memory polymer composites. *Polymer* 201354(9), 2199-2221.
- [30] Wang, K.; Jia, Y.; Zhu, X. Two-way reversible shape memory polymers made of cross-linked cocrystallizable random copolymers with tunable actuation temperatures. *Macromolecules* 2017, 50(21), 8570-8579.
- [31] Belmonte, A.; Lama, G. C.; Gentile, G.; Fernández-Francos, X.; De la Flor, S.; Cerruti, P.; et al. Synthesis and characterization of liquid-crystalline networks: Toward autonomous shape-memory actuation. *J. Phy. Chem. C* 2017, 121(40), 22403-22414.
- [32] Biswas, A.; Aswal, V. K.; Ray, B.; Maiti, P. Nanostructure-controlled shape memory effect in polyurethanes. *J. Phy. Chem. C* 2018, 122(20), 11167-11176.
- [33] Yan, W.; Rudolph, T.; Noechel, U.; Gould, O.; Behl, M.; Kratz, K.; Lendlein, A. Reversible actuation of thermoplastic multiblock copolymers with overlapping thermal transitions of crystalline and glassy domains. *Macromolecules* 2018, 51, 4624-4632
- [34] Belmonte, A.; Lama, G. C.; Gentile, G.; Cerruti, P.; Ambroggi, V.; Fernández-Francos, X.; De la Flor, S. Thermally-triggered free-standing shape-memory actuators. *Eur. Polym. J.* 2017, 97, 241-252.

- [35] Parameswaranpillai, J.; Ramanan, S. P.; Jose, S.; Siengchin, S.; Magueresse, A.; Janke, A.; Pionteck, J. Shape memory properties of Epoxy/PPO–PEO–PPO triblock copolymer blends with tunable thermal transitions and mechanical characteristics. *Ind. Eng. Chem. Res.* 2017, 56(47), 14069-14077.
- [36] Ji, S.; Fan, F.; Sun, C.; Yu, Y.; Xu, H. Visible light-induced plasticity of shape memory polymers. *ACS Appl. Mater. Interfaces* 2017, 9(38), 33169-33175.
- [37] Mishra, S. R.; Tracy, J. B. Sequential actuation of shape-memory polymers through wavelength-selective photothermal heating of gold nanospheres and nanorods. *ACS Appl. Nano Mater.* 2018.
- [38] Li, C.; Qiu, L.; Zhang, B.; Li, D.; Liu, C. Y. Robust vacuum-/air-dried graphene aerogels and fast recoverable shape-memory hybrid foams. *Adv. Mater.* 2016, 28(7), 1510-1516.
- [39] Zhang, P.; Behl, M.; Peng, X.; Razzaq, M. Y.; Lendlein, A. Ultrasonic cavitation induced shape-memory effect in porous polymer networks. *Macromol. Rapid Comm.* 2016, 37(23), 1897-1903.
- [40] Liu, Y.; Lv, H.; Lan, X.; Leng, J.; Du, S. Review of electro-active shape-memory polymer composite. *Compos. Sci. Technol.* 2009, 69(13), 2064-2068.
- [41] Ratna, D.; Karger-Kocsis, J. Recent advances in shape memory polymers and composites: A review. *J. Mater. Sci.* 2008, 43(1), 254-269.
- [42] Dong, Y.; Ni, Q. Q.; Li, L.; Fu, Y. Novel vapor-grown carbon nanofiber/epoxy shape memory nanocomposites prepared via latex technology. *Mater. Lett.* 2014, 132, 206-209.
- [43] Dong, Y.; Ni, Q. Q.; Fu, Y. Preparation and characterization of water-borne epoxy shape memory composites containing silica. *Compos. Part A: Appl. S.* 2015, 72, 1-10.

- [44] Dong, Y.; Fu, Y.; Ni, Q. Q. In-situ grown silica/water-borne epoxy shape memory composite foams prepared without blowing agent addition. *J. Appl. Polym. Sci.* 2015, 132(39).
- [45] Dong, Y.; Xia, H.; Zhu, Y.; Ni, Q. Q.; Fu, Y. Effect of epoxy-graft-polyoxyethylene octyl phenyl ether on preparation, mechanical properties and triple-shape memory effect of carbon nanotube/water-borne epoxy nanocomposites. *Compos. Sci. Technol.* 2015, 120, 17-25.
- [46] Lu, J.; Arsalan, A.; Dong, Y.; Zhu, Y.; Qian, C.; Wang, R.; et al. Shape memory effect and recovery stress property of carbon nanotube/waterborne epoxy nanocomposites investigated via TMA. *Polym. Test.* 2017, 59, 462-469.
- [47] Hummers, W. S.; Offeman, R. E. Preparation of Graphitic Oxide. *J. Am. Chem. Soc.* 1958, 80(6), 1339-1339.
- [48] Chen, H.; Xia, H.; Qiu, Y.; Xu, Z.; Ni, Q. Q. Smart composites of piezoelectric particles and shape memory polymers for actuation and nanopositioning. *Compos. Sci. Technol.* 2018, 163, 123-132.
- [49] Chen, H.; Xia, H.; Qiu, Y.; Ni, Q. Q. Analyzing effects of interfaces on recovery rates of shape memory composites from the perspective of molecular motions. *Compos. Sci. Technol.* 2018, 163, 105-115.
- [50] Chen, H.; Xia, H.; Ni, Q. Q. Study on material performances of lead zirconate titanate/shape memory polyurethane composites combining shape memory and piezoelectric effect. *Compos. Part A: Appl. Sci.* 2018, 110, 183-189.
- [51] Yan, Y.; Xia, H.; Qiu, Y.; Xu, Z.; Ni, Q. Q. Shape memory driving thickness-adjustable G@SMPU sponge with ultrahigh carbon loading ratio for excellent microwave shielding performance. *Mater. Lett.* 2019, 236, 116-119.

- [52] Bandara, N.; Esparza, Y.; Wu, J. Graphite oxide improves adhesion and water resistance of canola protein–graphite oxide hybrid adhesive. *Sci. Rep.* 2017, 7(1), 11538.

Chapter 3

**Graphite micro-flakes and shape memory
polyurethane filled sponge for shape memory
driving thickness-adjustable microwave
shielding**

3 Graphite micro-flakes and shape memory polyurethane filled sponge for shape memory driving thickness-adjustable microwave shielding

3.1 Introduction

Recently, to overcome increasingly deteriorative electromagnetic interference (EMI) and radiation hazard for human health, especially from microwave, carbon based nano/micro-composites, such as graphite [1], carbon black [2], carbon nanotube [3, 4], graphene [5, 6], and carbon nanofiber [7], have been widely researched for microwave shielding mainly due to their electrical conductive properties and unique one/two/three dimensional structures. Generally, higher percent of carbon content in composite would give a higher electromagnetic shielding effect [8-11]. Thus, pure carbon interface could possibly provide better reflection effect due to good interface mismatch. Although some researchers have developed free-standing pure carbon materials for electromagnetic shielding, their mechanical performances, such as elongation and deformation ability, were not enough at all [12, 13].

Therefore, in this chapter, we proposed a novel and facile approach by utilizing melamine sponge having lots of interspace for loading of typical pure carbon material, graphite (G) micro-flakes, as shown in **Fig. 3.1a**. To fix and avoid the drop of G micro-flakes from the sponge, shape memory polyurethane (SMPU) with cooling fixing and heating recovery abilities was adhered onto the surfaces of the G micro-flakes by dipping. In this approach, there would be three obvious advantages sticking out for this graphite micro-flakes filled and shape memory polyurethane fixed (G@SMPU) sponge. (1) Ultrahigh carbon loading ratio could be obtained; (2) The internal porous structure of this G@SMPU sponge could be also utilized to weaken the

incident electromagnetic wave energy by repeated reflection and interference; (3) Thickness adjustable G@SMPU sponge driven by shape memory effect could be obtained.

3.2. Experimental

3.2.1 Materials

Graphite powder and tetrahydrofuran (THF) were all purchased from Wako Pure Chemical Industries Ltd, Japan. SMPU pellets (MS6520, SMP Technologies Inc, Japan) were obtained from SMP technologies Company, Japan. All chemicals were used without further purification.

3.2.2 Preparation of G@SMPU sponge

SMPU, reported in our previous work [14], was used as shape memory composition with T_g of ~ 65 °C and T_m of ~ 170 °C. G@SMPU Sponge was fabricated by sonication assisted dipping approach, as shown in **Fig. 3.1b**. Firstly, different weight of graphite (0 g, 3 g, 6 g, 9 g, and 18 g) and 300 ml distilled water were in turn added in a teflon container and subjected to sonication for 30 min. Then, melamine sponge pre-cut into 90 mm * 90 mm * 26 mm (L * W * H) was dipped into the solution and sonicated for 60 min. After that, the sponges loading different graphite (denoted as G-M sponge, M: 0, 3, 6, 9, 18) were dried at 75 °C for one week. Secondly, the G sponge was dipped into a 300 ml 2 g/ml SMPU/THF solution for 20 min. Then, the sponge was dried for 48 h at 70 °C. Finally, G@SMPU sponges with different weight of graphite (denoted as G-M@SMPU sponge, M: 0, 3, 6, 9, 18) were obtained.

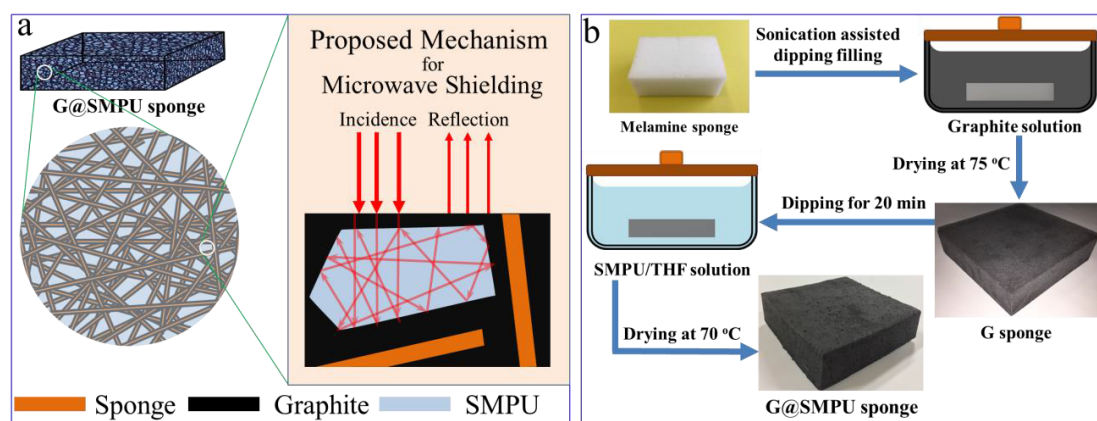


Fig. 3.1 (a) Proposed multi-reflection mechanism for microwave shielding; (b) Fabrication approach for G@SMPU sponge.

3.2.3 Characterization and evaluation

Structures of G and SMPU were characterized by X Ray Diffraction (XRD, MiniFlex300, Japan) and Nicolet 5700 attenuated total reflection Fourier transform infrared (ATR-FTIR) instrument (Thermo Electron Corp., USA). Cross sections of G sponges were observed by photographic camera. Conductivity of G sponges was measured by standard four-probe method using a MCP-HT450 conductivity meter (Dia Instruments Co.).

Shape memory evaluation of G@SMPU sponges was carried out in a dryer with a transparent glass cover for observation. For details, the heated G@SMPU sponge was cool-compressed up to 20 MPa by pressing machine and kept for 10 min for fixing. Then, the compressed G@SMPU sponge was transferred into the dryer for recovery at 80 °C. Besides, maximum compression ratio was measured by calculating the thickness before and after compression. Microwave shielding was evaluated in 7.0-16.5 GHz using transmission attenuation measurement system for microwave (KEYCOM Corp.), which connects with a vector network analyzer (37247D, Anritsu Co. Ltd.) for calculation of shielding effectiveness (SE).

3.3 Results and discussion

3.3.1 Morphology and structure

For SMPU, N-H stretching vibration peak revealed at 3305 cm^{-1} in FTIR spectrum (**Fig. 3.2a**), suggesting its consistency with typical polyurethane. For G micro-flakes, they have the size ranging in 5-20 μm , and exhibited a sharp feature peak at 26.5° in XRD pattern (**Fig. 3.2b**), which is typical graphitic structure.

With increasing addition of G micro-flakes to dipping solution, the loading ratio of the sponge increased as well. G-18 sponge could reach up to 490 wt.%, which is almost 5 times than the weight of the sponge itself. This demonstrated the sponge has a high loading ratio for carbon materials. Also, the porosities of G sponges decreased with increasing loading ratio of G (**Fig. 3.2c-2f**). This is because of the filling of G inside the sponge having lots of internal space (average pore size of $\sim 128\text{ }\mu\text{m}$). For G-18 sponge, there had been no obvious pores observable, indicating saturation of internal space of the sponge.

Fig. 3.2g presents the weight percentages of each composition in G@SMPU sponge. The weight percentage of the sponge composition showed a declining trend down to 8.3 wt.% because of increasing total weight of G@SMPU sponge. Although the SMPU compositions in different G@SMPU sponges exhibited decreased weight percentage down to 51.3 wt.%, in fact, weight calculation suggests they have about the same weight (G-3→G-18: 11.64 g, 11.60 g, 11.37 g, 11.63 g). This indicates the absorption capacity of the sponge for SMPU/THF solution was not influenced by increasing G loading due to its penetrability. For G compositions, they gave a rising weight percentage up to 40.4 wt.%.

Fig. 3.2h shows the electrical conductivity of G sponges. Clearly, with the increase of G, the electrical conductivity of G sponges increased as well. G-18 sponge could achieve an electrical

conductivity up to approximately 0.01 S/cm. This increasing electrical conductivity could be expected for enhanced electromagnetic shielding performance due to its contribution to both reflection and absorption.

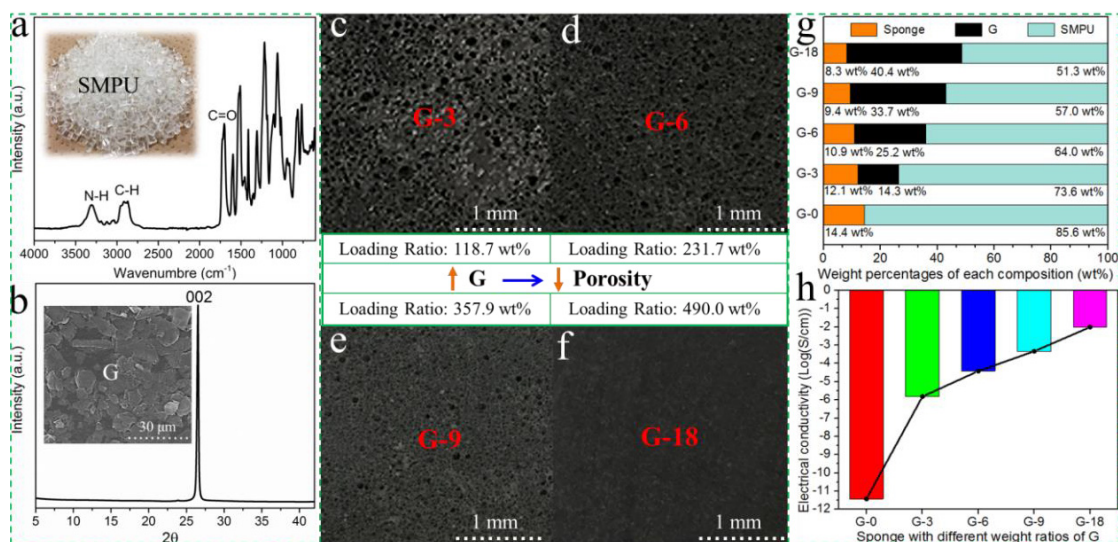


Fig. 3.2 (a) FTIR of SMPU; (b) XRD of G; (c, d, e, f) Cross sections of G sponges; (g) Weight percentages of each composition in G@SMPU sponge; (h) Electrical conductivity of G sponges.

3.3.2 Shape memory effect

Shape memory effect of this G@SMPU sponge was then investigated by compressing in thickness direction. **Fig 3.3a** shows the comparison of G-9@SMPU sponge before and after compression. No obvious damage and spontaneous recovery were found after cool compression. When transferred in preheated dryer, the SMPU inside G-9@SMPU sponge received heat and started to swell gradually, as seen in **Fig. 3.3b**. Within 92 s, G-9@SMPU sponge has achieved the shape recovery of above 95 %. As time proceeds up to 216 s, G-9@SMPU sponge gave a better recovery, and no obvious compression wrinkle was observable from its surface. Other G@SMPU sponges also showed compressing would not cause damage.

Fig 3.3c summarized the shape recovery ratio, time and maximum compression ratio of G@SMPU sponges. G-0@SMPU sponge, namely pure SMPU sponge, reached a recovery ratio of

nearly 100 %. With increasing G loading into sponge, the recovery ratio of G@SMPU sponge exhibited a declining trend. In spite of this, G-18@SMPU sponge could still give a recovery ratio above 90 %. This is because SMPU had to overcome the block of G to get back to original shape. Consequently, the recovery time of G@SMPU sponge were also extended because of increasing G loading. As seen in **Fig. 3.3c**, G-18@SMPU sponge recovered slower 3 times than G-0@SMPU sponge did. In addition, similar to recovery ratio, because of the blocking of G micro-flakes, the maximum compression ratio of G@SMPU sponge also gradually decreased from 86.5 % of G-0@SMPU sponge to 62.6 % of G-18@SMPU sponge.

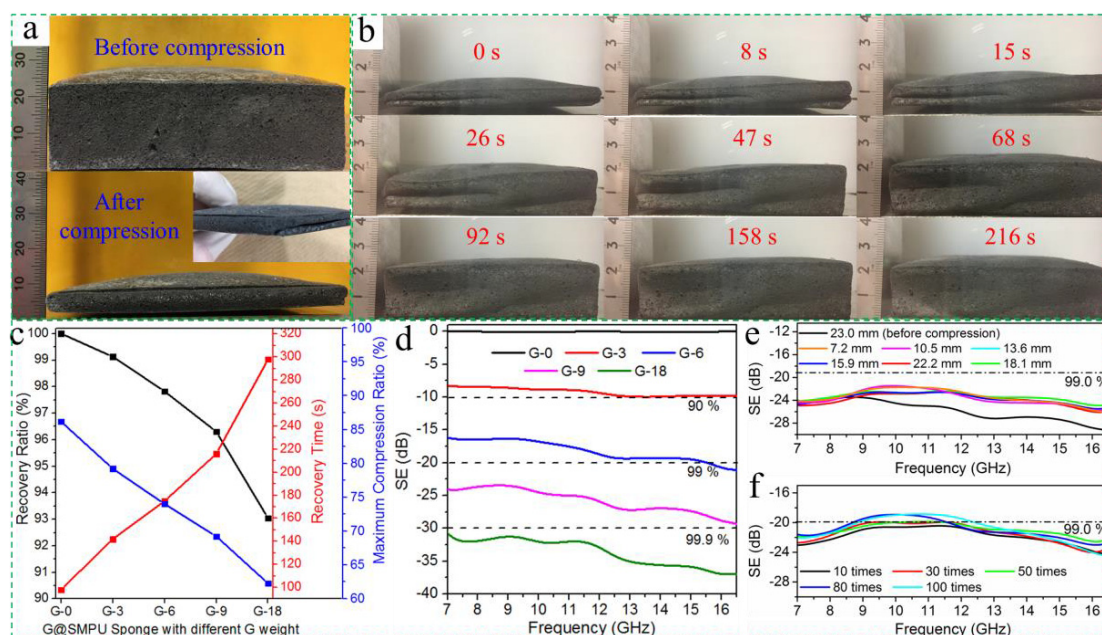


Fig. 3.3 (a) G-9@SMPU sponge before and after compression; (b) Shape recovery process of G-9@SMPU sponge; (c) Recovery ratio, time and maximum compression ratio of G@SMPU sponges; (d) SE of G@SMPU sponges; (e) SE of G-9@SMPU sponge under different thickness; (f) SE of G-9@SMPU sponge after undergoing different compression times.

3.3.3 Electromagnetic shielding effect

For electromagnetic shielding effectiveness (SE), G-9 and G-18@SMPU sponges could reach

the SE values above 20 dB, and 30 dB, respectively, as presented in **Fig 3.3d**. This indicates both of them have achieved a shielding percentage over 99 %. The G-9@SMPU sponge after compression had a subtle decrease of SE (**Fig. 3.3e**). It may result from the generation of internal defects, which the fall-off of the G micro-flakes from the internal interfaces of the sponge brought on. After compression and recovery for a few times, changing compression thickness would not apparently influence the shielding effect.

Fig 3.3f shows the SE of G-9@SMPU sponge by different compression times (10 times → 100 times). There was no obvious shielding change after even compressed for 100 times, which indicates the steady adhesion of G micro-flakes inside G@SMPU sponge due to the fixing of SMPU. This shape memory driving thickness-adjustable G@SMPU sponge with ultrahigh carbon loading could be expected for mobile electromagnetic shielding devices, which requires compression and impact-resistant performance.

3.4 Conclusions

We fabricated a novel shape memory driving thickness-adjustable G@SMPU sponge with ultrahigh carbon loading ratio by two-step dipping for microwave shielding. Dipping coating of SMPU onto the G sponge gave a good shape memory recovery effect above 90 %. G-9@SMPU and G-18@SMPU sponges achieved the shielding percentages more than 99.0 % and 99.9 %, respectively. Moreover, the shielding of this G@SMPU sponge would not weaken obviously when varying thickness or increasing compression time. This indicates the steady distribution and adhesion of G inside the sponge due to the fixing of SMPU.

References

- [1] S. Maiti, N.K. Shrivastava, S. Suin, B. B. Khatua, *ACS Appl. Mater. Interface* 5 (2013) 4712-4724.
- [2] M. Rahaman, T.K. Chaki, D. Khastgir. *J. Mater. Sci.* 46 (2011) 3989-3999.
- [3] Z. Zeng, M. Chen, H. Jin, W. Li, X. Xue, L. Zhou, Y. Pei, H. Zhang, Z. Zhang, *Carbon* 96 (2016) 768-777.
- [4] Z. Zeng, H. Jin, M. Chen, W. Li, L. Zhou, X. Xue, Z. Zhang, *Small* 13 (2017) 1701388.
- [5] N. Yousefi, X. Sun, X. Lin, X. Shen, J. Jia, B. Zhang, B. Tang, M. Chan, J.-K. Kim, *Adv. Mater.* 26 (2014) 5480-5487.
- [6] Y. Wu, Z. Wang, X. Liu, X. Shen, Q. Zheng, Q. Xue, J.-K. Kim, *ACS Appl. Mater. Interface* 9 (2017) 9059-9069.
- [7] S.S. Chauhan, M. Abraham, V. Choudhary, *J. Mater. Sci.* 51(2016) 9705-9715.
- [8] P. Verma, P. Saini, R.S. Malik, V. Choudhary, *Carbon* 89 (2015) 308-317.
- [9] T.K. Gupta, B.P. Singh, R.B. Mathur, S.R. Dhakate, *Nanoscale* 6 (2014) 842-851.
- [10] Y. Chen, H.B. Zhang, Y. Yang, M. Wang, A. Cao, Z.Z. Yu, *Adv. Funct. Mater.* 26 (2016) 447-455.
- [11] M. Qu, F. Nilsson, Y. Qin, G. Yang, Y. Pan, X. Liu, G.H. Rodriguez, J. Chen, C. Zhang, D.W. Schubert, *Compos. Sci. Technol.* 150 (2017) 24-31.
- [12] Z. Chen, C. Xu, C. Ma, W. Ren, H.M. Cheng, *Adv. Mater.* 25 (2013) 1296-1300.
- [13] L. Zhang, N.T. Alvarez, M. Zhang, M. Haase, R. Malik, D. Mast, V. Shanov, *Carbon* 82 (2015) 353-359.
- [14] H. Chen, H. Xia, Y. Qiu, Q.Q. Ni, *Compos. Sci. Technol.* 163 (2018) 105-115.

Chapter 4

**Vapor grown carbon fiber structured
polyurethane foam for compression-adjusted
microwave shielding**

4 Vapor grown carbon fiber structured polyurethane foam for compression-adjusted microwave shielding

4.1 Introduction

In recent years, to take place of conventional metals that was ever used for shielding electromagnetic (EM) wave particularly from the frequency range in microwave, carbon based nano/micro-composites, such as graphene, carbon nanotube (CNT), carbon black (CB), graphite, and carbon nanofiber (CNF), have been wide-spread researched to prevent electromagnetic interference (EMI) and protect human health from radiation due to their electrical conductive properties, and unique one/two/three dimensional structures [1-9]. Except for excellent EM shielding performance, carbon composites, which take different forms of products such as films, foams, nonwoven fabrics, porous materials, and textiles, are also supposed to have light weight, high strength and flexibility, strong resistance to environmental corrosion and oxidation in order to cater for varieties of application fields [10-17]. Thereby, the development of carbon/polymer composites is no doubt to be considered as one significant direction, because diverse polymers, which can be well modified and adjusted for targeted property, make the abovementioned properties well satisfied.

As well-known, EM shielding effectiveness (SE) is mainly a sum of reflection and absorption loss. For carbon composites, reflection loss is related to their surface property. Absorption loss plays more important role in contributing to total shielding [18-20]. Either way, electrical conductivity is vital because it favors to both of them. Therefore, the enhancement of electrical conductivity is a significant issue for high-efficiency EM shielding. However, when compared to the metals like silver (Ag) and copper (Cu), there is still a great lack of electrical conductivity for

carbon composites. Most carbon fillers containing polymers (electrically conductive polymers excluded), such as carbon nanotube (CNT) and graphene based composites, could only reach up to the electrical conductivity below 15 S/cm (mostly below 1 S/cm) when carbon fillers are below the weight content like 20 wt.% [21-24]. As for the reason, except for intrinsic low electrical conductivity of carbon materials, loose physical structure and discrete electrical connection of carbon composites are considered as other key points to lower the electrical conductivity. It is believed that the electrical conductivity of carbon composites can still be improved by structure optimization.

In this chapter, we developed a unique organic solvent-water exchange approach for preparation of polymer foam. By using this approach, we fabricated vapor grown carbon fiber (VGCF) based polyurethane foam (VGCF@PUF) for compression-adjusted high-performance microwave shielding. Hot compression was used for structure optimization. It is found that continuous compression resulted in obvious increase of electrical conductivity, and EM shielding effectiveness increased as well with the increase in extent of compression. This research demonstrated that the effective inter-connection of the electrically conductive composition in carbon based composites has a great impact on EM shielding performance. What is more, it is found that adjustable EM shielding performance could be achieved by different thickness compression.

4.2 Experimental

4.2.1 Materials

Polyurethane (PU, MM 6520, SMP Technologies Inc, Japan), Vapor grown carbon fiber (VGCF, Showa Denko K.K., Japan), *N, N*-dimethyl formamide (DMF, Wako Pure Chemical

Industries, Ltd), and all other reagents were used as received without further purification.

4.2.2 Fabrication of VGCF@PUF

VGCF@PUF was fabricated by H₂O-DMF solvent exchange and subsequent natural drying, as illustrated in **Fig. 4.1a** and **4.1b**. VGCFs (electrical conductivity of $1 * 10^4$ S/cm) were used in this research. They have the diameter of approximately 150 nm, as shown in **Fig. 4.2**. Firstly, VGCF was fully dispersed in 40 mg/ml PU/DMF solution in advance by the weight ratios (VGCF:PU, *w/w*) of 1:9, 3:7, and 1:1. The PU used has a *T_g* of ~ 65 °C, and a *T_m* of ~ 170 °C. Then, one piece of commercial polypropylene (PP) substrate, which has rough surface, was alternately dipped in distilled (DL) water, and the VGCF containing PU/DMF solution for 20 cycles. For each dipping in the two solutions, standing for 3 mins was carried out in a vertically suspended way to flow extra DL water and DMF out of the film attached on the PP substrate. The thickness of the film increased with increasing dipping cycles. After that, the film deposited on the PP substrate was suspended in air and dried slowly by household fan at room temperature (RT) for one week. Next, the obtained foamy film was peeled off and continually dried in oven at 80 °C for 48 h. Finally, VGCF containing PU foam (VGCF@PUF) was obtained.

The VGCF@PUF specimens with the VGCF contents of 10 wt.% (VGCF:PU, 1:9), 30 wt.% (VGCF:PU, 3:7), and 50 wt.% (VGCF:PU, 1:1) were denoted as VGCF@PUF-10, VGCF@PUF-30, and VGCF@PUF-50, respectively. Besides, the VGCF@PUF-30, which was used for hot compression, was dipped for 40 cycles. The hot compression was carried out at 120 °C in the pressure range of 0-20 MPa, and the holding time was maintained for 3 h for each compression.

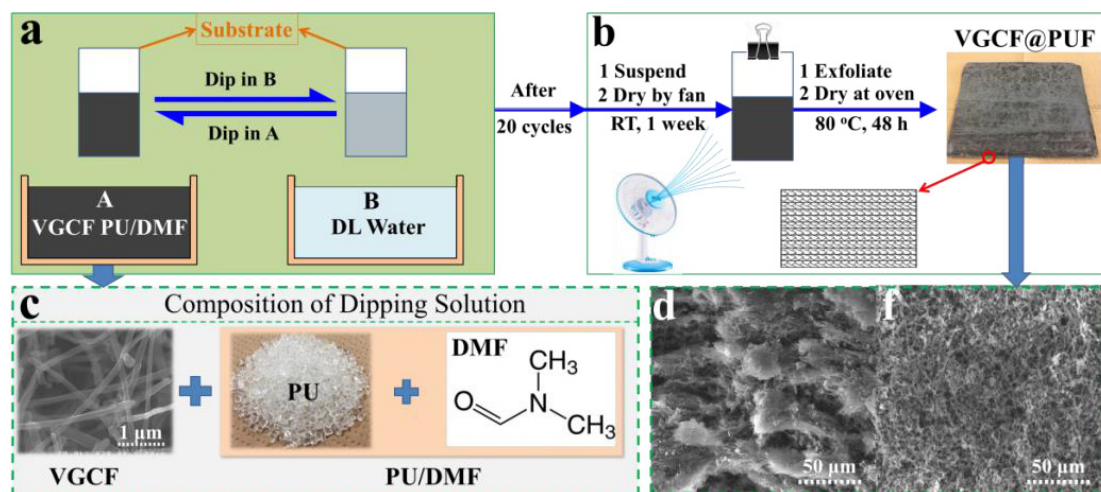


Fig. 4.1 Fabrication schematic of VGCF@PUF. (a) alternate dipping of PP substrate in VGCF containing PU/DMF and DL water; (b) two-stage drying of VGCF@PUF; (c) compositions of dipping solution VGCF PU/DMF; (d) cross sectional and (f) surface morphologies of VGCF@PUF.

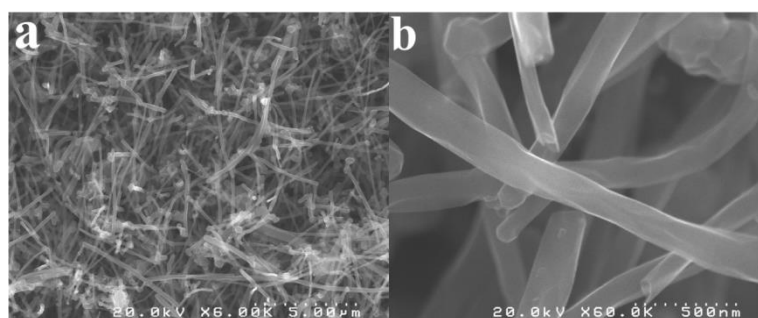


Fig. 4.2 Morphologies of VGCF under 5 μm and 500 nm scale.

4.2.3 Characterization

The morphologies and structures of VGCF@PUF specimens were characterized separately by Field emission scanning electron microscopy (FE-SEM, Hitachi S-5000, 20 kV), Nicolet 5700 attenuated total reflection Fourier Transform Infrared (ATR-FTIR) instrument (Thermo Electron Corp., USA), and Raman spectrometer with 532 nm laser excitation (HoloLab series 5000, Kaiser Optical Systems). The electrical conductivity of the VGCF@PUF films was measured by MCP-HT450 conductivity meter (Dia Instruments Co.) using standard four-probe method. The test

specimens were all uniformly cut into circles with the diameter of 12 mm. The mass density was calculated based on the weight and volume of the specimens. The real weight content of the VGCF composition in the VGCF@PUF was calculated by (I) dissolution and centrifugation of the PUF in the VGCF@PUF to remove PU composition, and (II) drying of the VGCF precipitate to weigh VGCF content. The mechanical properties of the film specimens were characterized by tensile tester (RTC1250A, A&D Co.) at a speed of 1 mm/min. The specimens were dumb-bell shapes with effective dimension of 12 mm * 2 mm (length * width).

Microwave shielding was evaluated in the frequency range of 0.5-18 GHz based on coaxial transmission line method. Coaxial tube measurement system (KEYCOM Corp.) connects with a vector network analyzer (37247D, Anritsu Co. Ltd.) for calculation of shielding effectiveness (SE). The dimension of the test specimens were concentric circles with the outer diameters (*OD*) of 12 mm, and the inner diameters (*ID*) of 2.5 mm.

4.3 Results and discussion

4.3.1 VGCF@PUF with different weight contents

H₂O-DMF solvent exchange made lots of water molecules permeate into PU medium, and VGCF@PUF was then formed after slow evaporation of the water out of the polyurethane foam (PUF). The VGCF@PUF exhibits a carpet-like flocky morphology in which VGCF disperse well in PUF (**Fig. 4.3a-c**). This is because the presence of the VGCF. The VGCF has the diameter of approximately 150 nm, and the length varying in the range of 3-6 μ m. These nanofibers blocked the formation of continuous PUF phase. The PU used was obtained by polyaddition of linear chain diisocyanate and polyol. The amino (-NH-) and ketone (-CO-) groups in its feature structure carbamate (-NH-CO-O-) were detected by FTIR, as shown in **Fig. 4.3d**. For the VGCF@PUF

specimens with different weight contents of VGCF, the feature peaks of VGCF and PUF compositions were both found in Raman spectrums (**Fig. 4.3e**). However, the strongest peak of PUF, the one at approximately 1615 cm^{-1} , gradually disappeared with increasing addition of VGCF, as shown in **Fig. 4.3e**. We attribute this to the coverage by the G peak of VGCF.

Then, the physical structures of the obtained VGCF@PUF specimens were investigated. The thickness of the VGCF@PUF showed an increased tendency (**Fig. 4.3f**). VGCF@PUF-50 could even reach up to 2.09 mm, suggesting the thickness of 5 times larger than pure PUF film. This is attributed to the increase of viscosity of dipping solution VGCF PU/DMF. Meanwhile, the density of VGCF@PUF decreased (**Fig. 4.3g**). The reason is that increased VGCF content achieved more blocking and isolation to PUF phase. As presented in **Fig. 4.3c**, lots of PUF stripes could be observed. Then, weight measurement indicated that the real weight contents of the VGCF in VGCF@PUF are 7.9 wt.%, 26.2 wt.%, and 45.6 wt.%, respectively (**Fig. 4.3h**). This is because of easier outflow of the VGCF with DMF out of the substrate when picking it up from the dipping solution. For electrical conductivity, VGCF@PUF showed a rising value with the increase of VGCF content (**Fig. 4.3h**). VGCF@PUF-50 could give a maximum value of $\sim 0.13\text{ S/cm}$. However, this value is not enough at all when comparing to the electrical conductivity of VGCF highly up to $1 * 10^4\text{ S/cm}$. It is believed that the electrical conductivity of this VGCF@PUF could still be improved by structure optimization. Therefore, hot compression was subjected next for investigation of electrical conductivity.

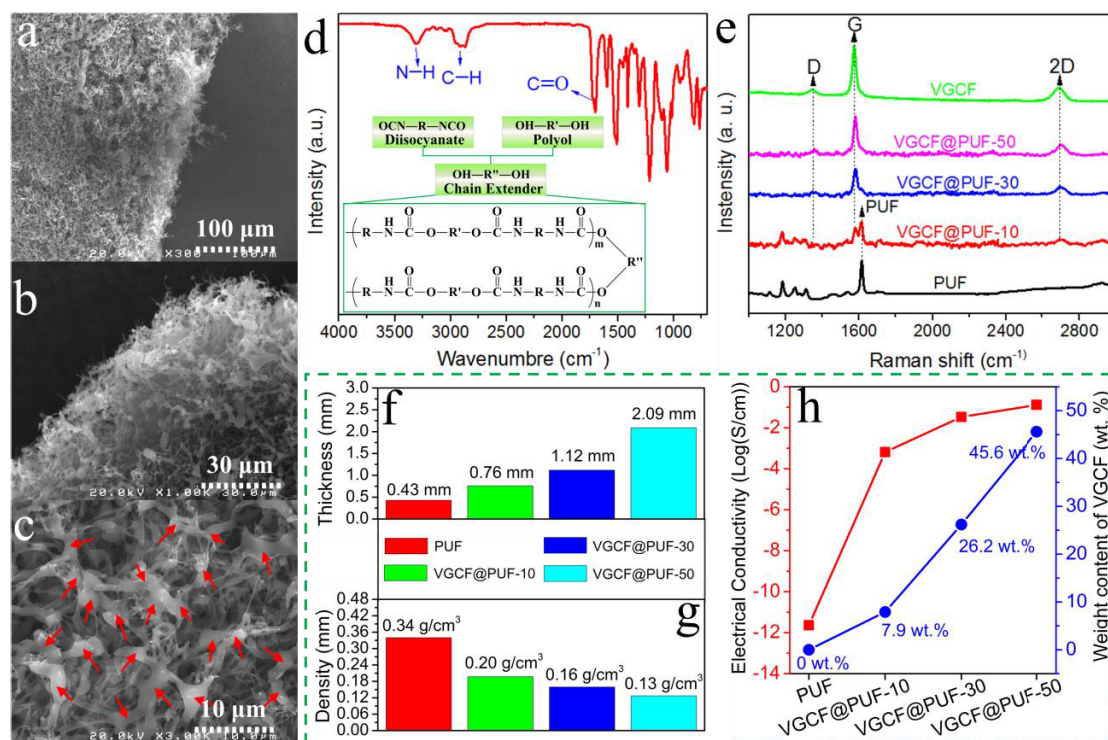


Fig. 4.3 (a, b, c) Morphologies of the VGCF@PUF-30 under different scales with red arrows referring to PUF stripes; (d) FTIR and chemical structure of pure PUF; (e) Raman spectrums of the VGCF, PUF, and the VGCF@PUF specimens with different weight contents; (f) thickness, and (g) density of the VGCF@PUF specimens with different weight contents; (h) electrical conductivity, and real VGCF contents of the VGCF@PUF specimens with different weight contents.

4.3.2 VGCF@PUF with different compression

The VGCF@PUF-30, which was dipped for 40 cycles, has initial thickness of 1.96 mm, and VGCF content of 25.3 wt.%. It was used for hot compression at 120 °C in the pressure range of 0-20 MPa. The VGCF@PUF-30 specimens with decreased thickness (1.23, 0.74, 0.45, and 0.12 mm) were obtained by adjusting compression pressure. As seen from **Fig. 4.4a-d**, the surface of the VGCF@PUF-30 gradually changed from porous structure to film form. This is attributed to the fusion of the PUF stripes under high temperature and pressure. **Fig. 4.4e-h** show the cross

sectional view of the VGCF@PUF specimens undergoing different compression. It can be observed that layered cross section also turn integrated with continuous hot compression.

Study on the mechanical properties of the VGCF@PUF-30 specimens indicated that both tensile strength and elongation at breaking position are enhanced with the increase in extent of compression (1.96-mm thick VGCF@PUF-30 excluded) (**Fig. 4.4i**). This resulted from more and more fusing of discrete PUF stripes into continuous PU phase, which could obviously enhance the mechanical performance of VGCF@PUF. As demonstrated in **Fig. 4.4J**, the hot pressing under high temperature (120 °C) and pressure (15 Mpa) made white pure PUF turn into transparent PU film, thus resulting in drastic increase of both the strength and elongation of the PUF. When it comes to electrical conductivity, the compaction of the VGCF@PUF by hot-compression could make it continuously increased in the thickness range from 1.96 to 0.12 mm, as shown in **Fig. 4.4k**. The maximum of electrical conductivity could go up to ~ 17.9 S/cm. This suggested that the effective electrical inter-connection of VGCF by structure optimization is vital for improvement of electrical conductivity. Owing to increasing electrical conductivity of the VGCF@PUF-30 specimens with continuous compression, high-performance microwave shielding effect could be expected in the following investigation.

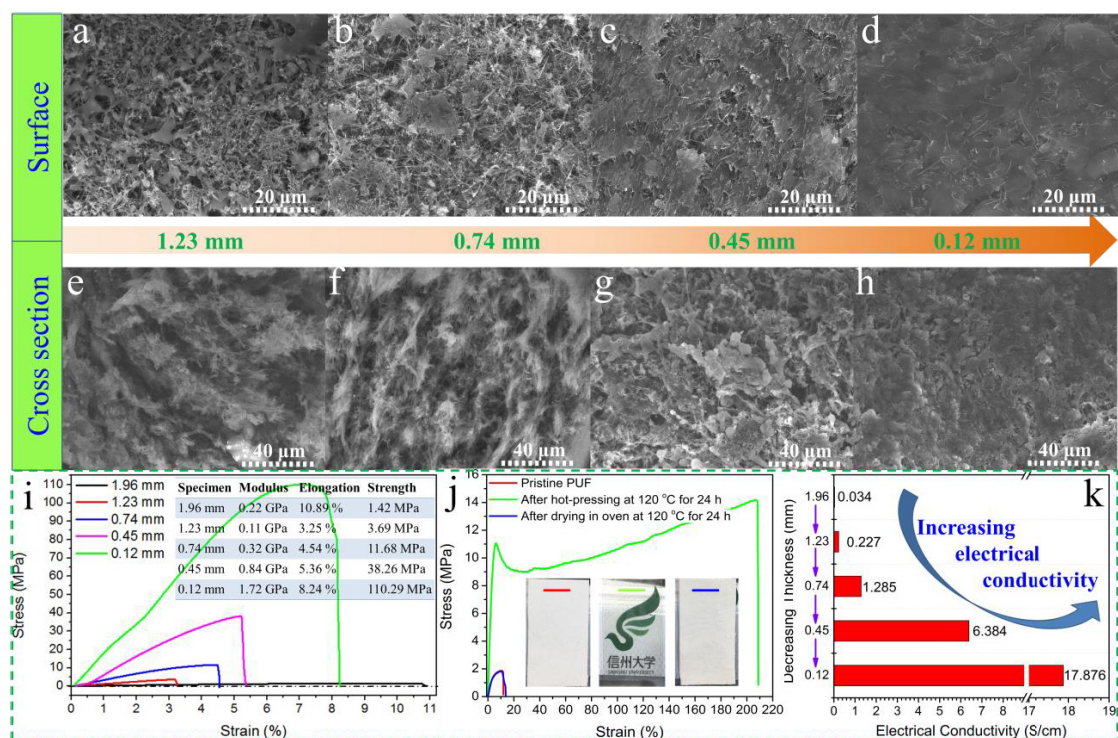


Fig. 4.4 (a, b, c, d) Surface and (e, f, g, h) cross sectional morphologies of the VGCF@PUF-30 specimens with different compression thickness; (i) strain-stress curves and summary of mechanical properties; (j) change in mechanical properties before and after treating pure PUF by hot pressing at 120 °C, and drying in oven at 120 °C; (k) change in electrical conductivity of the VGCF@PUF-30 specimens with decreasing thickness.

4.3.3 Microwave Shielding of VGCF@PUF

Microwave shielding evaluation was carried out based on coaxial transmission line method in the frequency range of 0.5-18 GHz. The shielding result indicated the VGCF@PUF with different VGCF contents exhibited an increased microwave shielding with increasing addition of VGCF (Fig. 4.5a). The VGCF@PUF-50 with ~ 2.1 mm thickness reached a shielding efficiency above 90 % (i.e., above 10 dB) in 0.5-18 GHz. To understand the shielding mechanism of this VGCF@PUF, the reflection (SE_R) and absorption (SE_A) parts are separately analyzed. The total shielding is mainly the sum of reflection (SE_R) and absorption (SE_A), as well as some other

influence. As seen from **Fig. 4.5b** and **4.5c**, both of them increased at the same time. This is attributed to the increase of the VGCF@PUF specimens in VGCF content and thickness. Moreover, the larger SE_A of VGCF@PUF than SE_R indicates this VGCF@PUF is absorption-dominated shielding composite foam. This result is consistent with most research previously reported [18-20]. However, when comparing to their shielding effect, the shielding performances of these VGCF@PUF specimens are not as high as expected. The low shielding values of these VGCF@PUF specimens were considered to be related to their loose structures, as shown in **Fig. 4.3a-c**. There should be enough potential to further improve the shielding effectiveness by optimizing internal structure of the VGCF@PUF specimens. Considering that the VGCF@PUF is a foam with lots of internal space, hot compression was therefore selected to change the structure of the VGCF@PUF.

VGCF@PUF-30, which was dipped for 40 cycles, was used to investigate the effect of hot compression on the microwave shielding of the VGCF@PUF. The VGCF@PUF-30 with different compression thickness gave an obviously increased shielding effectiveness in the frequency range from 0.5 GHz to 18 GHz. As presented in **Fig. 4.5d**, hot-compressing the VGCF@PUF from original 1.96 mm to 0.45 mm made the shielding effectiveness increase from 10-15 dB to be above 35 dB. All of compressed specimens basically achieved a shielding efficiency above 99 %. VGCF@PUF-30 having 0.45 mm thickness could reach above 99.99 % (i.e., above 40 dB) in the frequency range of 6.7-18 GHz. These results are attributed to the increase of electrical conductivity of the VGCF@PUF-30 specimens, which was achieved by more and more electrical inter-connection of VGCF fillers with continuous hot-compression. In spite of decreased thickness, increasing electrical conductivity made this VGCF@PUF-30 achieve a higher shielding

effectiveness. Especially for absorption, compressed thickness made it greatly increased, as shown in **Fig. 4.5f**.

For mechanism of those, total shielding effectiveness (SE) consists of reflection (SE_R), absorption (SE_A), and internal multiple reflection (SE_{MR}), as illustrated in **Fig. 4.5g** and the green part of **Fig. 4.5h**. As to SE_R , the higher the electrical conductivity is, the higher it is, as shown in **Fig. 4.5e**. SE_A can be expressed below:

$$SE_A = 8.686d\sqrt{\pi f\sigma\mu} \quad (1)$$

where d , f , σ , and μ are thickness, frequency, electrical conductivity, and permeability, respectively.

As demonstrated in the equations (blue part) of **Fig. 4.5h**, with VGCF@PUF-30 compressed from original A status to B and C status, increased σ enhanced the reflection SE_R . Furthermore, the change of SE_A is codetermined by three variables, d , σ , and μ . Owing to the non-magnetic property of this VGCF@PUF, the μ is considered to show only slight increase with increasing compression, and the influence is neglected here. Therefore, the change of SE_A is mainly determined by thickness d and electrical conductivity σ . During the compression process from original 1.96 mm to 0.45 mm, drastic increase of the electrical conductivity, which turned more than 5 times larger for each compression, made the value of SE_A increased in spite of decreased thickness, as illustrated in the equation (yellow part) of **Fig. 4.5h**. In addition, SE_{MR} is neglected here due to relatively high shielding value above 15 dB. As a result, the total shielding exhibited an increased shielding effectiveness.

However, further compression to 0.12 mm resulted in decreased shielding effectiveness of the VGCF@PUF-30. This is because hot-compressing the VGCF@PUF-30 to 0.12 mm didn't increase σ obviously (only ~ 3 times larger than former compression) compared to previous

drastic increase of electrical conductivity, as shown in **Fig. 4.4k**. This final compression only led to subtle increase of SE_R , as can be seen in **Fig. 4.5e**. Furthermore, the decrease of the specimen thickness resulted in obviously decreased SE_A , as seen in **Fig. 4.5f**. Therefore, the EM shielding measurement gave a decreased value of SE_{total} . We predict that there should be maximal shielding effectiveness by adjusting compression thickness to a certain value.

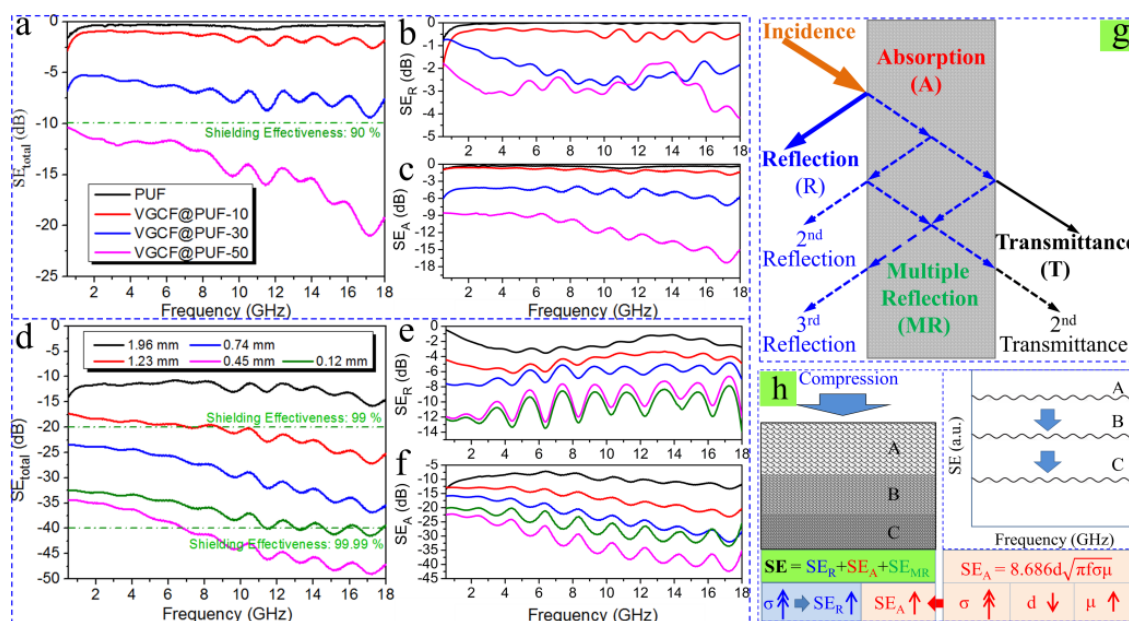


Fig. 4.5 (a) Total SE (SE_{total}), (b) SE_R , and (c) SE_A of the VGCF@PUF specimens with different contents of VGCF; (d) total SE, (e) SE_R , and (f) SE_A of the VGCF@PUF-30 specimens with different compression thickness; (g) mechanism schematic of EM shielding; (h) equation based analysis on the change of SE, SE_R and SE_A during hot compression.

4.4 Conclusions

A H_2O -DMF solvent exchange approach was developed for preparation of nano/micro composite foam. By this approach, vapor grown carbon fiber based polyurethane foam (VGCF@PUF) was fabricated for compression-adjusted microwave shielding. The results showed that the hot compression under 120 °C for VGCF@PUF made discrete PUF stripes, which formed due to the presence of VGCF, fuse together. Therefore, the mechanical performance of the

VGCF@PUF was improved, such as the strength and elongation. At the same time, the hot compression drastically enhanced the electrical conductivity for orders of magnitude. For microwave shielding, in the frequency range from 0.5 GHz to 18 GHz, hot-compressing the VGCF@PUF from original 1.96 mm to 0.45 mm made the shielding effectiveness increase from 10-15 dB to be above 35 dB. This suggests that the structure optimization of carbon filled shielding materials, such as the compacting approach in this research, could promote effective electrical inter-connection of carbon fillers, and thus achieve high-performance microwave shielding.

References

- [1] Wu Y, Wang Z, Liu X, Shen X, Zheng Q, Xue Q, Kim JK. Ultralight graphene foam/conductive polymer composites for exceptional electromagnetic interference shielding. *ACS Appl Mater Interface* 2017; 9(10): 9059-69.
- [2] Shen, B., Li, Y., Yi, D., Zhai, W., Wei, X., & Zheng, W. (2017). Strong flexible polymer/graphene composite films with 3D saw-tooth folding for enhanced and tunable electromagnetic shielding. *Carbon*, 113, 55-62.
- [3] Zeng, Z., Wang, C., Zhang, Y., Wang, P., Seyed Shahabadi, S. I., Pei, Y., ... & Lu, X. (2018). Ultralight and Highly Elastic Graphene/Lignin-Derived Carbon Nanocomposite Aerogels with Ultrahigh Electromagnetic Interference Shielding Performance. *ACS applied materials & interfaces*, 10(9), 8205-8213.
- [4] Wan, Y. J., Zhu, P. L., Yu, S. H., Sun, R., Wong, C. P., & Liao, W. H. (2017). Ultralight, super-elastic and volume-preserving cellulose fiber/graphene aerogel for high-performance electromagnetic interference shielding. *Carbon*, 115, 629-639.
- [5] Yan, Y., Xia, H., Qiu, Y., Xu, Z., & Ni, Q. Q. (2019). Shape memory driving thickness-adjustable G@ SMPU sponge with ultrahigh carbon loading ratio for excellent microwave shielding performance. *Materials Letters*, 236, 116-119.
- [6] Rahaman, M., Chaki, T. K., & Khastgir, D. (2011). Development of high performance EMI shielding material from EVA, NBR, and their blends: effect of carbon black structure. *Journal of materials science*, 46(11), 3989-3999.
- [7] Chen, Z., Xu, C., Ma, C., Ren, W., & Cheng, H. M. (2013). Lightweight and flexible graphene foam composites for high - performance electromagnetic interference shielding.

- Advanced materials, 25(9), 1296-1300.
- [8] Song, W. L., Wang, J., Fan, L. Z., Li, Y., Wang, C. Y., & Cao, M. S. (2014). Interfacial engineering of carbon nanofiber–graphene–carbon nanofiber heterojunctions in flexible lightweight electromagnetic shielding networks. *ACS applied materials & interfaces*, 6(13), 10516-10523.
- [9] Al-Saleh, M. H., Saadeh, W. H., & Sundararaj, U. (2013). EMI shielding effectiveness of carbon based nanostructured polymeric materials: a comparative study. *Carbon*, 60, 146-156.
- [10] Song, W. L., Cao, M. S., Lu, M. M., Bi, S., Wang, C. Y., Liu, J., ... & Fan, L. Z. (2014). Flexible graphene/polymer composite films in sandwich structures for effective electromagnetic interference shielding. *Carbon*, 66, 67-76.
- [11] Zhang, L., Liu, M., Roy, S., Chu, E. K., See, K. Y., & Hu, X. (2016). Phthalonitrile-based carbon foam with high specific mechanical strength and superior electromagnetic interference shielding performance. *ACS applied materials & interfaces*, 8(11), 7422-7430.
- [12] Hong, X., & Chung, D. D. L. (2017). Carbon nanofiber mats for electromagnetic interference shielding. *Carbon*, 111, 529-537.
- [13] Han, J., Wang, X., Qiu, Y., Zhu, J., & Hu, P. (2015). Infrared-transparent films based on conductive graphene network fabrics for electromagnetic shielding. *Carbon*, 87, 206-214.
- [14] Yuan, Y., Yin, W., Yang, M., Xu, F., Zhao, X., Li, J., ... & Li, Y. (2018). Lightweight, flexible and strong core-shell non-woven fabrics covered by reduced graphene oxide for high-performance electromagnetic interference shielding. *Carbon*, 130, 59-68..
- [15] Song, W. L., Guan, X. T., Fan, L. Z., Cao, W. Q., Wang, C. Y., & Cao, M. S. (2015). Tuning three-dimensional textures with graphene aerogels for ultra-light flexible graphene/texture

- composites of effective electromagnetic shielding. *Carbon*, 93, 151-160.
- [16] Lin, Z. I., Lou, C. W., Pan, Y. J., Hsieh, C. T., Huang, C. H., Huang, C. L., ... & Lin, J. H. (2017). Conductive fabrics made of polypropylene/multi-walled carbon nanotube coated polyester yarns: Mechanical properties and electromagnetic interference shielding effectiveness. *Composites Science and Technology*, 141, 74-82.
- [17] Chen, Y., Zhang, H. B., Yang, Y., Wang, M., Cao, A., & Yu, Z. Z. (2016). High - Performance Epoxy Nanocomposites Reinforced with Three - Dimensional Carbon Nanotube Sponge for Electromagnetic Interference Shielding. *Advanced Functional Materials*, 26(3), 447-455.
- [18] Yan, D. X., Pang, H., Li, B., Vajtai, R., Xu, L., Ren, P. G., ... & Li, Z. M. (2015). Structured reduced graphene oxide/polymer composites for ultra - efficient electromagnetic interference shielding. *Advanced Functional Materials*, 25(4), 559-566.
- [19] Yan, D. X., Ren, P. G., Pang, H., Fu, Q., Yang, M. B., & Li, Z. M. (2012). Efficient electromagnetic interference shielding of lightweight graphene/polystyrene composite. *Journal of Materials Chemistry*, 22(36), 18772-18774.
- [20] Zhang, H. B., Yan, Q., Zheng, W. G., He, Z., & Yu, Z. Z. (2011). Tough graphene- polymer microcellular foams for electromagnetic interference shielding. *ACS applied materials & interfaces*, 3(3), 918-924.
- [21] Feng, Q. P., Yang, J. P., Fu, S. Y., & Mai, Y. W. (2010). Synthesis of carbon nanotube/epoxy composite films with a high nanotube loading by a mixed-curing-agent assisted layer-by-layer method and their electrical conductivity. *Carbon*, 48(7), 2057-2062.
- [22] Ling, J., Zhai, W., Feng, W., Shen, B., Zhang, J., & Zheng, W. G. (2013). Facile preparation

of lightweight microcellular polyetherimide/graphene composite foams for electromagnetic interference shielding. *ACS applied materials & interfaces*, 5(7), 2677-2684.

[23] Liang, J., Wang, Y., Huang, Y., Ma, Y., Liu, Z., Cai, J., ... & Chen, Y. (2009). Electromagnetic interference shielding of graphene/epoxy composites. *Carbon*, 47(3), 922-925.

[24] Sankaran, S., Deshmukh, K., Ahamed, M. B., & Pasha, S. K. (2018). Recent Advances in Electromagnetic Interference Shielding Properties of Metal and Carbon Filler Reinforced Flexible Polymer Composites: A Review. *Composites Part A: Applied Science and Manufacturing*.

Chapter 5

**Fabrication of gradient vapor grown carbon
fiber based polyurethane foam for shape
memory driven microwave shielding**

5 Fabrication of gradient vapor grown carbon fiber based polyurethane foam for shape memory driven microwave shielding

5.1 Introduction

Over the past few decades, conventional metallic composites have been widely investigated in the field of electromagnetic (EM) shielding for applications including aviation and radar systems, restricting electromagnetic interference (EMI), and protecting human health from EM radiation, especially that of the microwave frequency band. Recently, carbon based nano/micro-composites, such as graphene [1-3], carbon nanotubes (CNTs) [4-6], carbon black (CB) [7], graphite [8], and carbon nanofibers (CNFs) [9], have attracted considerable attention for EM shielding owing to their high specific surface areas, electrical conductivity, and unique one, two, and three dimensional structures [10, 11] of these materials. Carbon-based composites can take different forms such as films, foams, nonwoven fabrics, porous materials, and textiles. Different applications benefit from additional properties such as being light weight and resistance to environmental corrosion oxidation and having high strength and flexibility [12-16]. Consequently, carbon/polymer composites, as an important group of carbon composites, are considered important in the field of EM shielding because of the rich variety of available natural and synthetic polymers, which can be modified and adjusted for targeted properties.

Rapid development of advanced intelligence security and smart electronic equipment has led to demand for functional EM shielding devices, which can respond to external stimulus (i.e., electricity, heat, and light) or/and have tunable shielding effect, such as controllable EM shielding switch for cutoff and reception of EM signals [17-24]. For example, Wang and co-workers have reported a kind of hydro-sensitive sandwich structure by embedding porous polypropylene

non-woven spacers into highly conductive pyrolytic graphite papers. In the presence and absence of polar water molecules, porous spacers achieved a switchable structural transformation through polar induced interfaces. Thus, under dry and wet conditions, the sandwich structures exhibited weak and strong EM shielding ability, respectively [25]. Furthermore, Chen et al. prepared a biomass-derived electrically conductive macroscopic carbon grid (MCG) by carbonizing wood-pulp fabric matting. They found that double-layered MCG showed tunable EM shielding performance by varying the interleaving degree of the stacked grids through tiny translational motion [26]. Therefore, increasing attention is being paid to developing carbon based shielding composites for functional EM shielding.

In recent years, many types of shape memory polymers (SMPs) containing films, foams, fibers, hydrogels, and fabrics, have been reported, which can respond to various external stimuli such as heat, electricity, light, chemical solvent and pH [27-33]. In most cases, shape recovery and fixity effects, which include recovery time, ratio, force, and fixity ratio, were mainly studied to estimate primary performance of those SMPs. However, in terms of the evaluation for their practical applications, little relevant work has been performed except for limited applications, such as soft actuators, functional textures, and medical applications [34-40]. As for the reason, there is still a limited understanding of how SMPs might be applicable to different fields. Thus, with the aim of expanding applications of SMPs. we therefore introduced shape memory polymers to EM shielding field for the development of functional shielding devices.

In this chapter, the cooling fixing and heating recovery abilities of the SMPU, which have been investigated in previous chapters, were utilized for bending based adjustable EM shielding. Firstly, we fabricated gradient vapor grown carbon fiber (VGCF) based shape memory

polyurethane foam (VGCF@SMPUF) via alternatively dipping in distilled (DL) water, and a VGCF containing SMPU/DMF solution with a continuously decreasing VGCF concentration, for shape memory driven microwave shielding. The shape memory effect was achieved by heat transfer of thermally conductive VGCF. The shielding effectiveness (*SE*) of this VGCF@SMPUF was controlled by different degrees of shape recovery. Moreover, the gradient distribution of the VGCF could directionally improve the efficiency of the shape recovery. Furthermore, microwave shielding of this VGCF@SMPUF was also be adjusted by different degrees of hot compression.

5.2 Experimental

5.2.1 Materials

Polyurethane (MM 6520, SMP Technologies Inc, Japan), Vapor grown carbon fiber (VGCF, Showa Denko K.K., Japan), *N,N*-dimethyl formamide (DMF, Wako Pure Chemical Industries, Ltd), DL water (Wako Pure Chemical Industries, Ltd), and all other reagents were used as received without further purification.

5.2.2 Fabrication of gradient VGCF@SMPUF

On the basis of H₂O-DMF solvent exchange, gradient VGCF@SMPUF was fabricated by alternate dipping of a PP substrate in DL water, and VGCF containing SMPU/DMF solution, where the VGCF concentration decreased for later dipping cycles, as illustrated in **Fig. 5.1**. Specifically, 2 g of VGCF (electrical conductivity of 1×10^4 S/cm, fiber diameter of ~150 nm) was at first dispersed in 100 mL 80 mg/mL of a SMPU/DMF solution by sonication for 1 h and magnetic stirring for 1 h in turn. Then, a polypropylene (PP) substrate was alternately dipped into solution A (VGCF@SMPU/DMF), and solvent B (DL water) for 25 cycles. After each dip into solution A, 5 mL of solution A was removed, and 10 mL of solution C (SMPU/DMF), having the

same SMPU concentration as that of solution A, was added. The mixture was then sonicated for 5 mins and magnetically stirred for 5 mins in turn to uniformly disperse the VGCF. Next, the film formed on the PP substrate was suspended in air and dried slowly by fan at room temperature (*RT*) for 1 week. The film was peeled off and dried in an oven at 80 °C for 48 h. Finally, the obtained gradient VGCF@SMPUF was prepressed at 80 °C for 12 h. Pure SMPUF was similarly prepared by alternate dipping into an 80-mg/mL SMPU/DMF solution and DL water for 25 cycles.

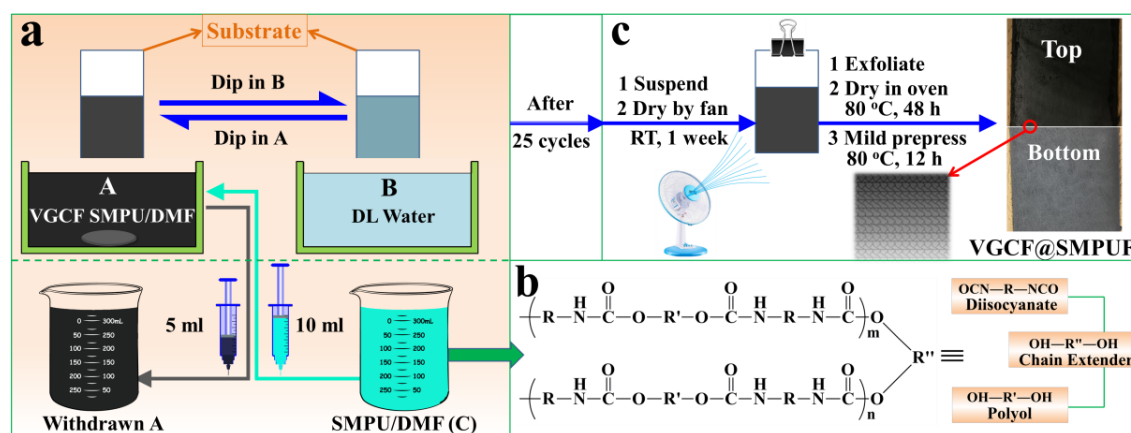


Fig. 5.1 Schematic illustration showing fabrication of gradient VGCF@SMPUF. (a) alternative dipping of PP substrate in VGCF@SMPU/DMF (A) and DL water (B) with partial removal of solution A and addition of solution C after each dipping procedure into solution A; (b) chemical structure of SMPU; (c) two-stage drying and hot prepress of VGCF@SMPUF.

5.2.3 Characterization

The morphologies and structures of the VGCF@SMPUF specimens were characterized separately by field emission scanning electron microscope (FE-SEM, Hitachi S-5000, 20 kV) and Raman spectrometer with 532-nm laser excitation (HoloLab series 5000, Kaiser Optical Systems). Conductivity was measured by MCP-HT450 conductivity meter (Dia Instruments Co.) using standard four-probe method, and mechanical properties were measured by Tensilon tensile tester (RTC1250A, A&D Co.). The weight percentages of the VGCF composition at PS and NS were

regarded as the VGCF contents of the VGCF@SMPU in the initial and final dipping solutions (VGCF@SMPU/DMF). These weight percentages were indirectly calculated by precipitating the dipping solution to obtain the weight of VGCF@SMPU, and re-dissolving and centrifuging the SMPU composition of the dried VGCF@SMPU to obtain the weight of the VGCF.

The microwave shielding properties were evaluated in the frequency range between 6 and 16 GHz with a transmission attenuation measurement system (KEYCOM Corp.) connected to a vector network analyzer (37247D, Anritsu Co. Ltd.) to calculate the shielding effectiveness (*SE*). A heating device was equipped near the circular test area (Φ 7.5 cm) of the system to measure the variation of the shielding effectiveness during shape recovery. A VGCF@SMPUF specimen that was bent to the positive side (PS) (i.e., the higher VGCF content side) recovers from the PS, and is denoted as the recovery from the PS. The electromagnetic waves entered from this side. In a similar way, we describe the VGCF@SMPUF that was bent to the negative side (NS) (i.e., the lower VGCF content side) recovers from the NS.

5.3 Results and discussion

5.3.1 Morphology and structure

The VGCF had a diameter of approximately 150 nm and a length of a few micrometers. Raman measurement verified the presence of D and G feature peaks of VGCF (**Fig. 5.2a**). The SMPU used in this research, as previously studied in our group, is a typical shape memory polymer with a glass transition temperature (T_g) of ~ 65 °C, and melting temperature (T_m) of ~ 170 °C [41, 42]. The polymer was obtained by polyaddition of linear chain diisocyanate and polyol (**Fig. 5.1b**). The amino (-NH-) and ketone (-CO-) groups in its structure, carbamate (-NH-CO-O-), were detected by FTIR, as shown in **Fig. 5.2b**.

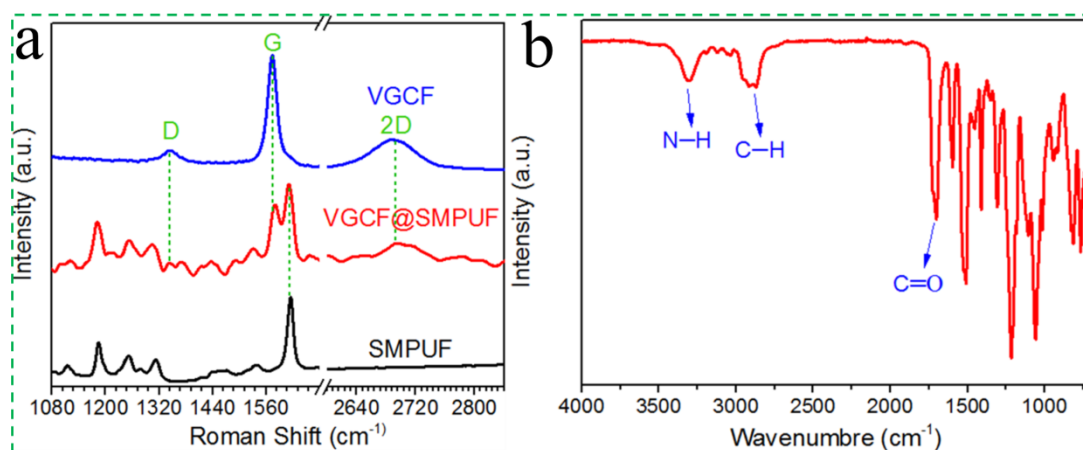


Fig. 5.2 (a) Raman spectrums of VGCF, SMPUF, and VGCF@SMPUF; (b) FTIR spectrum of shape memory polyurethane (SMPU)

The as-obtained VGCF@SMPUF had a black positive side and a white negative side with a porous morphology, as shown in **Fig. 5.3a-3d**. Compared with the low content of VGCF on the negative side, the higher content of VGCF on the positive side obviously impeded the formation of a continuous SMPU phase (**Fig. 5.3c**). For the formation of porous structure on the negative side, we attribute it to the slow evaporation of DL water during drying process (**Fig. 5.3d**). Owing to the strong solubility of DMF for the SMPUF component, inter-laminar fusion led to a subtle layer structure in the VGCF@SMPUF (**Fig. 5.3e**).

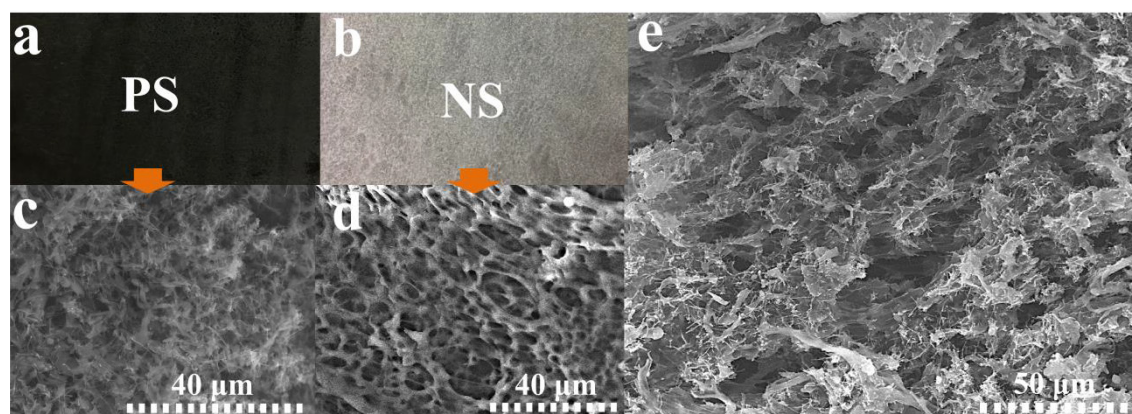


Fig. 5.3 (a, b, c, d) digital images of positive and negative sides of gradient VGCF@SMPUF and corresponding FESEM morphologies; (e) cross sectional view of gradient VGCF@SMPUF.

5.3.2 Conductive and mechanical properties

This gradient VGCF@SMPUF was 1.21-mm thick with a density of $\sim 0.31 \text{ g/cm}^3$ and a VGCF content of 13.18 wt.%, which exhibited an electrical conductivity (σ) of $\sim 4.68 \times 10^{-3} \text{ S/cm}$ (**Fig. 5.4a**). By comparison the PS and NS showed weight contents and electrical conductivities of approximately 19.78 wt.% and 4.87 wt.%, and $8.72 \times 10^{-2} \text{ S/cm}$ and $2.45 \times 10^{-4} \text{ S/cm}$, respectively (**Fig. 5.4b-4c**). This result suggested successful fabrication of a gradient VGCF@SMPUF. Strain-stress curves indicated that the addition of VGCF into SMPUF enhanced the elastic modulus and mechanical strength of the VGCF@SMPUF to be approximately 4 times as high as their original values, whereas the elongation decreased to be more than 2 times as high as its original value (**Fig. 5.5**). We conclude that the addition of VGCF increased the strength and lowered the flexibility of this SMPUF. This result is consistent with most studies that carbon nanofiber or nanotube based fillers have mechanical reinforcement effect on polymer matrices [43-46]

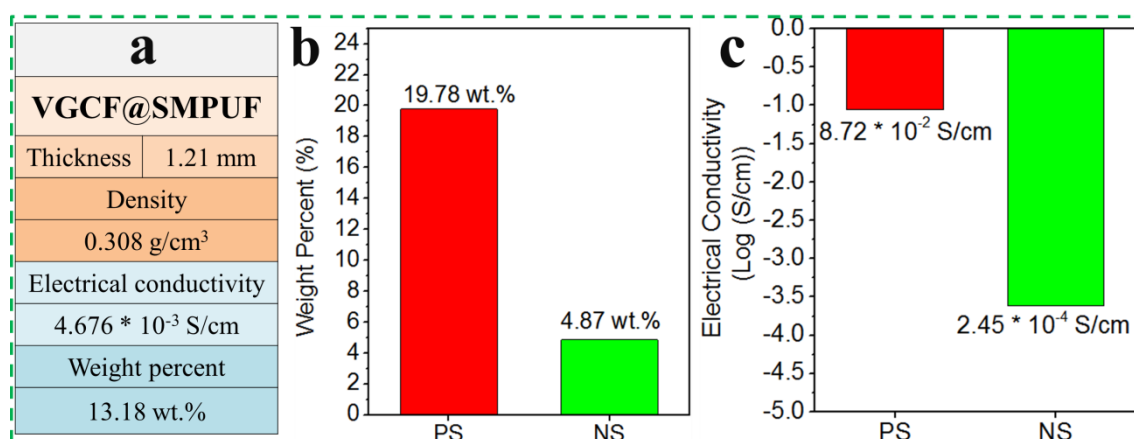


Fig. 5.4 (a) structure information of VGCF@SMPUF; (b, c) weight contents and electrical conductivities for PS and NS of VGCF@SMPUF.

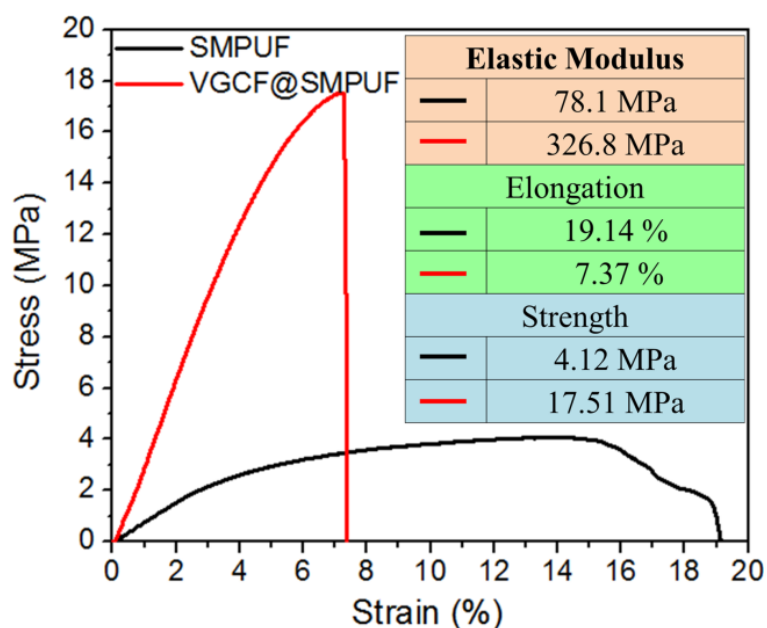


Fig. 5.5 Strain-stress curves of pure SMPUF, and gradient VGCF@SMPUF.

5.3.3 Microwave shielding based on different angle recovery

The SMPU used in this research is a typical temperature-responding one-way shape memory polymer. The shape recovery effect occurs when heating up to the T_g point of the polymer (approximately 65 °C). The VGCF@SMPUF fabricated based on this shape memory polymer was used to investigate the shape memory driven microwave shielding performance. Variation of the SE with the angle recovery was evaluated by the electromagnetic coverage extent of the VGCF@SMPUF to the circular testing area (**Fig. 5.6a-6b**). One side of the VGCF@SMPUF was expanded from the initially fixed right-angle status. The other side was clamped by two aluminum (Al) plates pre-heated to 90 °C. Thus, angle recovery of the VGCF@SMPUF bent to a right angle was achieved by heat transfer from the hot Al plates to VGCF@SMPUF.

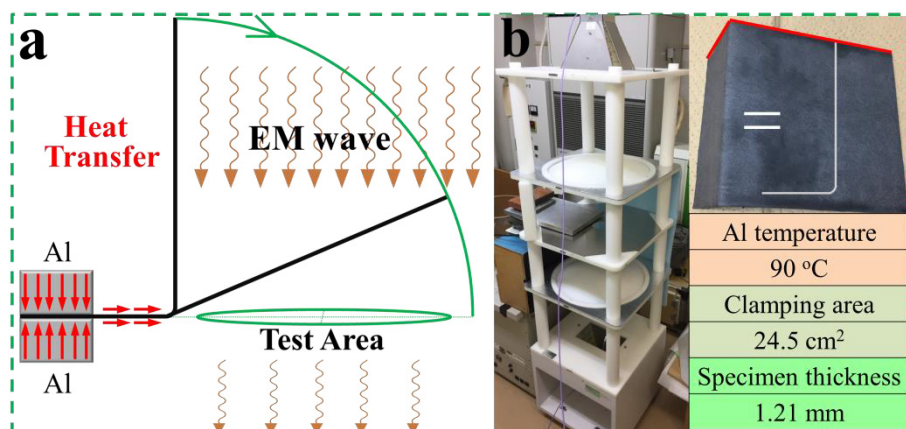


Fig. 5.6 (a) Measurement mechanism of electromagnetic shielding; (b) measurement devices, and conditions of electromagnetic shielding.

As shown in **Fig. 5.7a-b**, the shielding result suggests that the *SE* of the VGCF@SMPUF increased as the recovery angle increased in the frequency range of 6–16 GHz. When the VGCF@SMPUF, which was initially bent to PS and NS, recovered from the PS and NS upon heat transfer, there was no obvious difference in the *SE* values. For the two cases, VGCF@SMPUF gave a similar *SE* at a similar recovery angle. However, the recovery time from the PS and NS were obviously different. As shown in **Fig. 5.7c-7d**, recovery from the PS required 323 s whereas recovery from the NS required 538 s. We attribute these results to the different mechanical strength of PS and NS of the VGCF@SMPUF. The mechanism is discussed in the following section.

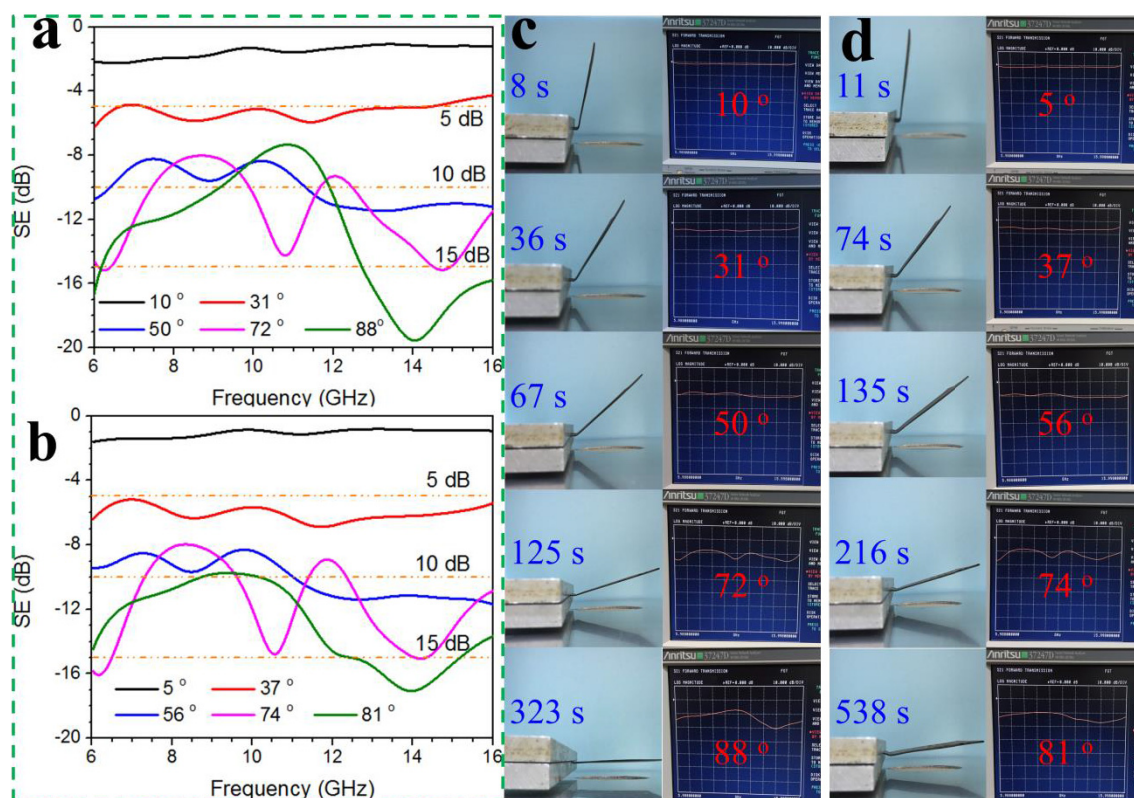


Fig. 5.7 SE change of (a) PS and (b) NS with increasing recovery angle; Angle variation and corresponding SE value of (c) PS and (d) NS of gradient VGCF@SMPUF.

5.3.4 Microwave shielding with different compression

VGCF@SMPUF specimens with thicknesses varying from 1.21 to 0.11 mm were obtained by hot compression. Microwave shielding evaluations indicated an increase of the SE value with decreasing thickness. As shown in **Fig. 5.8a-8b**, the gradient of the 0.11-mm thick VGCF@SMPUF sample reached a SE value up to ~30 dB (*i.e.*, a shielding efficiency of 99.9%) in the frequency range of 6–16 GHz. As for the reason, the shielding effectiveness is the sum of the reflection (SE_R), absorption (SE_A), and multiple reflection (SE_{MR}). Improved electrical conductivity (σ) generally results in an increase of SE_R . Therefore, the considerable increase of σ , which was attributed to continuous compression, increased SE_R . As shown in **Fig. 5.8c**, the VGCF@SMPUF at a thickness of 0.11 mm had σ values more than ~200 times as great as that of

original VGCF@SMPUF with a 1.21 mm thickness. Additionally, due to non-magnetic properties of the VGCF@SMPUF, compression is considered to have no obvious effect on permeability (μ), as shown in the inset of **Fig. 5.8c**. Thus, the value of SE_A increased despite the decrease of thickness. Given that the part of SE_{MR} can be neglected here (>15 dB), as a result, the total SE increased with compression. This indicates that the increase in SE is attributed to an increase of both reflection and absorption.

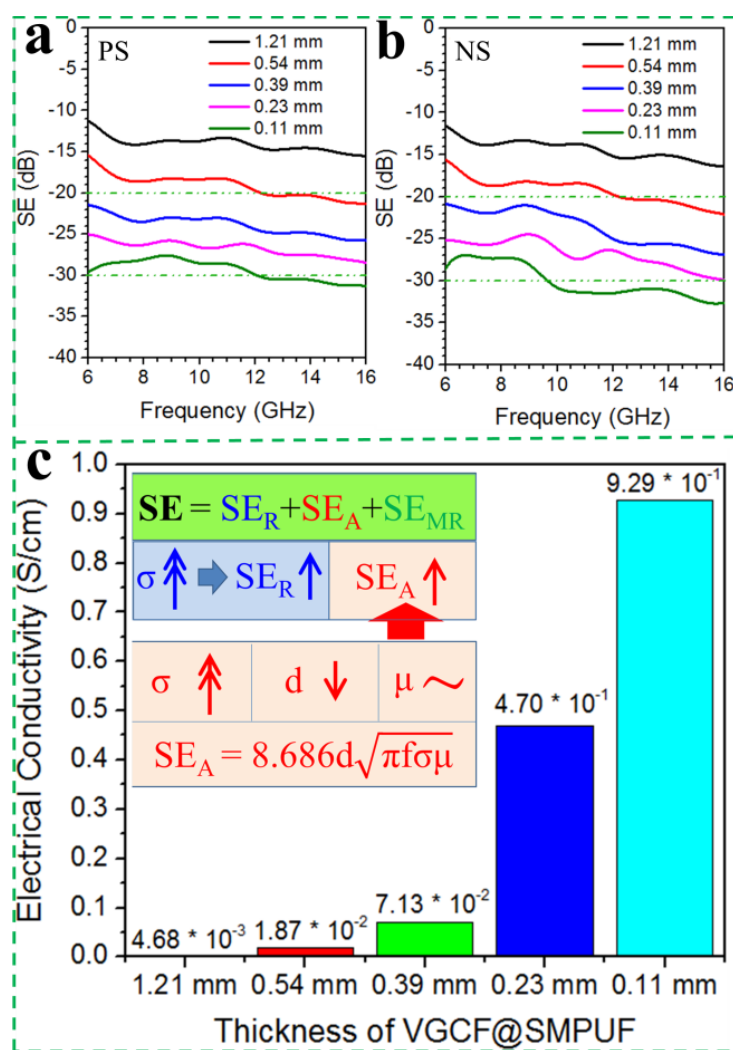


Fig. 5.8 Shielding effectiveness of (a) PS and (b) NS of the VGCF@SMPUF specimens at different extents of compression; (c) electrical conductivities, and change of SE_A and SE_R for the VGCF@SMPUF specimens with different thickness compression.

A comparison of the shielding properties indicates that the PS and NS of the VGCF@SMPUF

specimens with different thickness had similar shielding effects in the frequency range of 6–16 GHz, as shown in **Fig. 5.8a-8b**. In fact, the SE_R parts of those VGCF@SMPUF specimens were considered to be approximately the same because there should be no obvious change of SE_A when the microwave entered from either side of the VGCF@SMPUF. Regarding the reason for similar shielding effects from the PS and NSS, one possibly reason is that, for a non-homogeneous shielding composite, SE_R not only depends on the surface properties, such as surface resistance and permittivity, but also relies on internal properties of the shielding composite due to the presence of multiple interfaces. In other words, SE_R may be the sum of the surface and internal reflection, thus, making the SE_R of PS and NS similar, as illustrated in **Fig. 5.9**. Another possible reason is the similar shielding effects are because of the structure deviation. To confirm the exact reason, further research and demonstration based on lots of experiments are required.

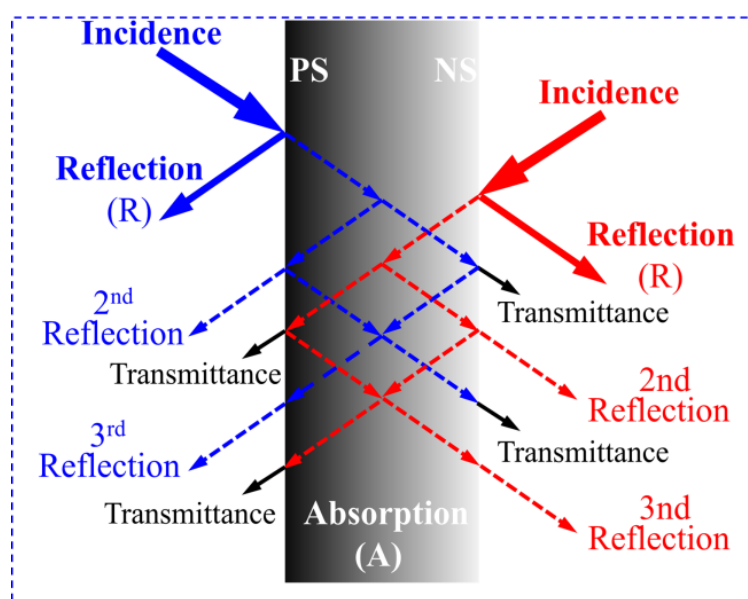


Fig. 5.9 Reflection effect from the PS and NS of gradient VGCF@SMPUF.

5.3.5 Different recovery efficiency on two sides

Then, we investigated the recovery time and ratio, and fixity ratio of this gradient VGCF@SMPUF at different extents of compression. As shown in **Fig. 5.10a-10c**, hot

compression induced a faster recovery of the VGCF@SMPUF and a higher recovery and fixity ratio. The VGCF@SMPUF at thicknesses of 0.23 and 0.11 mm recovered to 100% within tens of seconds. We attribute this result to compaction of the VGCF component, which thus improved the thermal conductivity of the gradient VGCF@SMPUF. As detected from its bending point, when clamped by the Al plates, the VGCF@SMPUF compressed to a thickness of 0.11 mm showed a faster elevation temperature than that of the sample that had not been subjected hot-compression (Fig. 5.11).

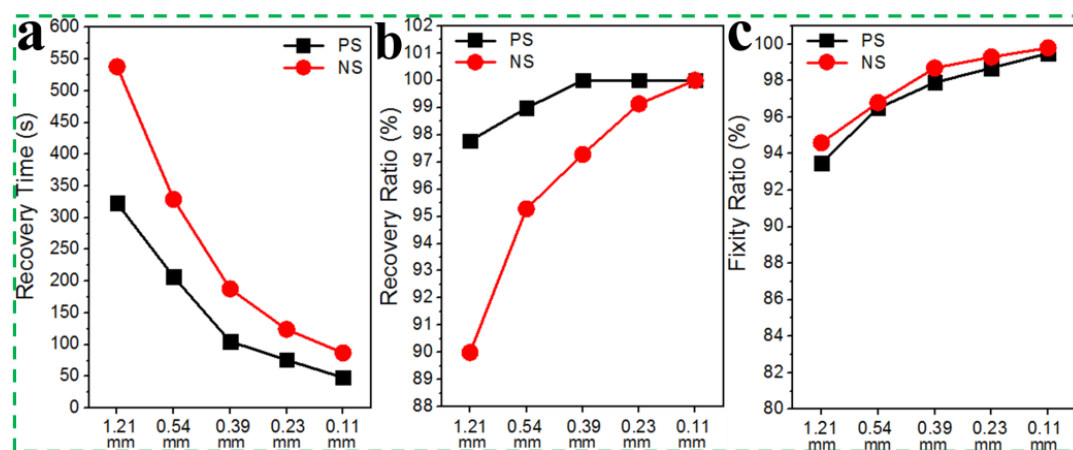


Fig. 5.10 (a) Recovery time, (b) recovery ratio, and (c) fixity ratio of PS and NS of the VGCF@SMPUF specimens with different compression, which were initially bent and fixed at a right angle.

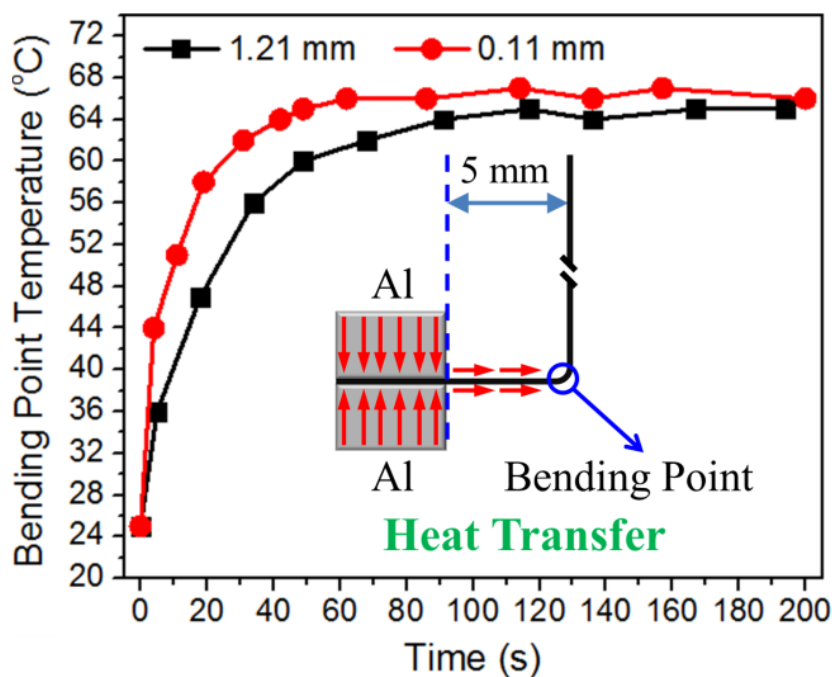


Fig. 5.11 Temperature change of the bending point with time for VGCF@SMPUF specimens with thicknesses of 1.21 and 0.11 mm.

5.3.6 Mechanism for different recovery

In addition, the VGCF@SMPUF that was bent to the PS, showed a faster recovery time and higher recovery ratio than that bent to the NS. As for the reason, recovery of bending is a process where stretching (inner edge) and compression (outer edge) at the bending point proceeds simultaneously. The outer edge of this gradient VGCF@SMPUF, bent to the NS, and had a greater mechanical compression strength than that bent to the PS owing to the higher VGCF content at the outer edge, as illustrated in **Fig. 5.12a**. Therefore, recovery from the PS was easier than from the NS. Notably, the recovery time, ratios, and bending point temperatures of this gradient VGCF@SMPUF became closer as hot-compression was increased, as shown in **Fig. 5.10a-10b**, and **Fig. 5.11**. We attribute this result to the approaching VGCF contents and properties of the two sides with continuous compression (**Fig. 5.12b**). Therefore, we conclude that this gradient fabrication of VGCF content featured different shape recovery efficiencies in the two sides (PS

and NS). This VGCF@SMPUF may have potential applications in the field of structural transformations of functional shielding devices.

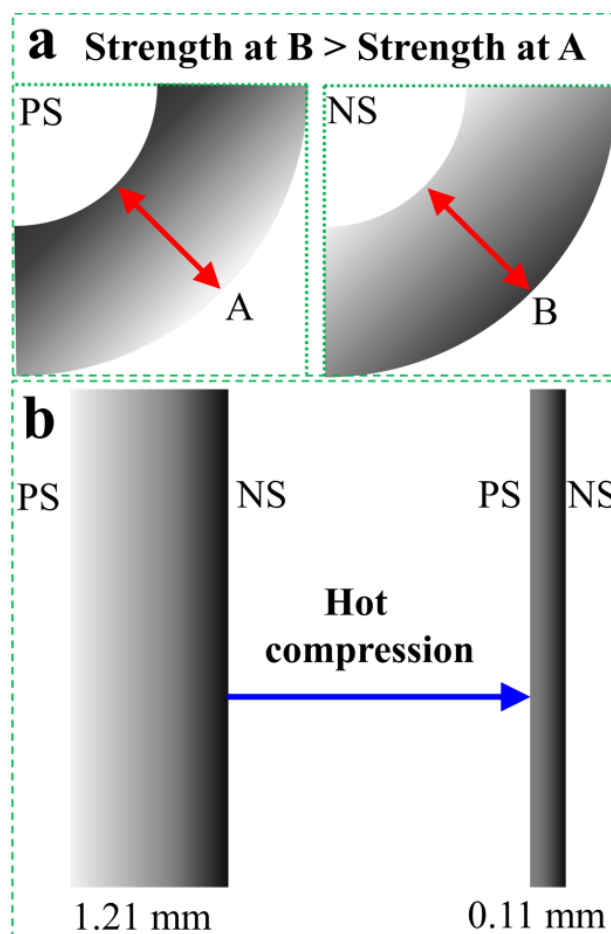


Fig. 5.12 (a) Comparison of the compression strength at the outer edges of PS and NS of gradient VGCF@SMPUF; (b) approaching VGCF contents of PS and NS with continuous hot compression.

This gradient VGCF@SMPUF functionalized traditional EM shielding material, and achieved the adjustment of EM shielding performance through the angle recovery. The shape memory effect was achieved by heat transfer of thermally conductive VGCF. The shielding effectiveness of this VGCF@SMPUF was controlled by different degrees of shape recovery. Moreover, the gradient distribution of the VGCF could directionally improve the efficiency of the angle recovery, such as the recovery ratio and time. However, there are also some limitations to this VGCF@SMPUF. For

examples, thick VGCF@SMPUF has decreased angle fixity and recover ratio, which affect the precision of control and adjustment of VGCF@SMPUF devices. This aspect might be improved by adjusting the mechanical strength of the two sides, which can be achieved by changing the gradient content of the VGCF in the thickness direction. Recently, some approaches based on three-point bending have been developed in order to measure bending recovery effect [47-49]. Therefore, we are intended to quantitatively investigate the bending recovery force and ratio of this gradient VGCF@SMPUF by referring those researches. In addition, the shape recovery of this gradient VGCF@SMPUF is also irreversible, which decreases the practicality and novelty of the device. In the following research, we may consider the development of reversible VGCF@SMP (*i.e.*, two-way SMPs).

5.4 Conclusions

Gradient vapor grown carbon fiber-based shape memory polyurethane foam (VGCF@SMPUF) was fabricated by alternative dipping in a VGCF containing SMPU/DMF solution of decreasing concentration and distilled water to form shape memory driven adjustable microwave shielding. Different electrical conductivities and VGCF contents on two sides of this gradient VGCF@SMPUF were obtained. The adjustability of the shielding effectiveness was achieved by different degrees of angle recovery. Hot compression could not only decrease the recovery time, and gave a higher recovery ratio, but also clearly improve the shielding performance of this gradient VGCF@SMPUF. Moreover, the VGCF@SMPUF recovery from the side with a higher VGCF content exhibited a faster recovery time and higher recovery ratio than that recovering from the side with a lower VGCF content owing to different mechanical strengths at either side.

References

- [1] Chen, Z., Xu, C., Ma, C., Ren, W., & Cheng, H. M. (2013). Lightweight and flexible graphene foam composites for high-performance electromagnetic interference shielding. *Advanced materials*, 25(9), 1296-1300.
- [2] Yousefi, N., Sun, X., Lin, X., Shen, X., Jia, J., Zhang, B., ... & Kim, J. K. (2014). Highly aligned graphene/polymer nanocomposites with excellent dielectric properties for high-performance electromagnetic interference shielding. *Advanced Materials*, 26(31), 5480-5487.
- [3] Wu, Y., Wang, Z., Liu, X., Shen, X., Zheng, Q., Xue, Q., & Kim, J. K. (2017). Ultralight graphene foam/conductive polymer composites for exceptional electromagnetic interference shielding. *ACS applied materials & interfaces*, 9(10), 9059-9069.
- [4] Zhang, K., Yu, H. O., Shi, Y. D., Chen, Y. F., Zeng, J. B., Guo, J., ... & Wang, M. (2017). Morphological regulation improved electrical conductivity and electromagnetic interference shielding in poly (L-lactide)/poly (ϵ -caprolactone)/carbon nanotube nanocomposites via constructing stereocomplex crystallites. *Journal of Materials Chemistry C*, 5(11), 2807-2817.
- [5] Zeng, Z., Jin, H., Chen, M., Li, W., Zhou, L., Xue, X., & Zhang, Z. (2017). Microstructure design of lightweight, flexible, and high electromagnetic shielding porous multiwalled carbon nanotube/polymer composites. *small*, 13(34), 1701388.
- [6] Zhang, K., Li, G. H., Feng, L. M., Wang, N., Guo, J., Sun, K., ... & Wang, M. (2017). Ultralow percolation threshold and enhanced electromagnetic interference shielding in poly (L-lactide)/multi-walled carbon nanotube nanocomposites with electrically conductive segregated networks. *Journal of Materials Chemistry C*, 5(36), 9359-9369.

- [7] Rahaman, M., Chaki, T. K., & Khastgir, D. (2011). Development of high performance EMI shielding material from EVA, NBR, and their blends: effect of carbon black structure. *Journal of materials science*, 46(11), 3989-3999.
- [8] Yan, Y., Xia, H., Qiu, Y., Xu, Z., & Ni, Q. Q. (2018). Shape memory driving thickness-adjustable G@ SMPU sponge with ultrahigh carbon loading ratio for excellent microwave shielding performance. *Materials Letters*, 236 (2019) 116-119.
- [9] Song, W. L., Wang, J., Fan, L. Z., Li, Y., Wang, C. Y., & Cao, M. S. (2014). Interfacial engineering of carbon nanofiber–graphene–carbon nanofiber heterojunctions in flexible lightweight electromagnetic shielding networks. *ACS applied materials & interfaces*, 6(13), 10516-10523.
- [10] Sankaran, S., Deshmukh, K., Ahamed, M. B., & Pasha, S. K. (2018). Recent advances in electromagnetic interference shielding properties of metal and carbon filler reinforced flexible polymer composites: A review. *Composites Part A: Applied Science and Manufacturing*, 114 (2018) 49-71
- [11] Al-Saleh, M. H., Saadeh, W. H., & Sundararaj, U. (2013). EMI shielding effectiveness of carbon based nanostructured polymeric materials: a comparative study. *Carbon*, 60, 146-156.
- [12] Song, W. L., Cao, M. S., Lu, M. M., Bi, S., Wang, C. Y., Liu, J., ... & Fan, L. Z. (2014). Flexible graphene/polymer composite films in sandwich structures for effective electromagnetic interference shielding. *Carbon*, 66, 67-76.
- [13] Ling, J., Zhai, W., Feng, W., Shen, B., Zhang, J., & Zheng, W. G. (2013). Facile preparation of lightweight microcellular polyetherimide/graphene composite foams for electromagnetic interference shielding. *ACS applied materials & interfaces*, 5(7), 2677-2684.

- [14] Hong, X., & Chung, D. D. L. (2017). Carbon nanofiber mats for electromagnetic interference shielding. *Carbon*, 111, 529-537.
- [15] Song, W. L., Guan, X. T., Fan, L. Z., Cao, W. Q., Wang, C. Y., & Cao, M. S. (2015). Tuning three-dimensional textures with graphene aerogels for ultra-light flexible graphene/texture composites of effective electromagnetic shielding. *Carbon*, 93, 151-160.
- [16] Zou, L., Zhang, S., Li, X., Lan, C., Qiu, Y., & Ma, Y. (2016). Step-by-Step Strategy for Constructing Multilayer Structured Coatings toward High-Efficiency Electromagnetic Interference Shielding. *Advanced Materials Interfaces*, 3(5), 1500476.
- [17] Cai, X., Hu, M., Zhang, D., Hu, G., & Yang, J. (2018). Experimental Study on Tunable Electromagnetic Shielding by Microlattice Materials with Organized Microstructures. *Advanced Engineering Materials*, 1700823.
- [18] Zhang, L. Q., Yang, B., Teng, J., Lei, J., Yan, D. X., Zhong, G. J., & Li, Z. M. (2017). Tunable electromagnetic interference shielding effectiveness via multilayer assembly of regenerated cellulose as a supporting substrate and carbon nanotubes/polymer as a functional layer. *Journal of Materials Chemistry C*, 5(12), 3130-3138.
- [19] Mishra, M., Singh, A. P., Gupta, V., Chandra, A., & Dhawan, S. K. (2016). Tunable EMI shielding effectiveness using new exotic carbon: Polymer composites. *Journal of Alloys and Compounds*, 688, 399-403.
- [20] Lu, L., Xing, D., Teh, K. S., Liu, H., Xie, Y., Liu, X., & Tang, Y. (2017). Structural effects in a composite nonwoven fabric on EMI shielding. *Materials & Design*, 120, 354-362.
- [21] Li, Y., Shen, B., Yi, D., Zhang, L., Zhai, W., Wei, X., & Zheng, W. (2017). The influence of gradient and sandwich configurations on the electromagnetic interference shielding

- performance of multilayered thermoplastic polyurethane/graphene composite foams. *Composites Science and Technology*, 138, 209-216.
- [22] Zhao, B., & Park, C. B. (2017). Tunable electromagnetic shielding properties of conductive poly (vinylidene fluoride)/Ni chain composite films with negative permittivity. *Journal of Materials Chemistry C*, 5(28), 6954-6961.
- [23] Lee, S. H., Yu, S., Shahzad, F., Kim, W. N., Park, C., Hong, S. M., & Koo, C. M. (2017). Density-tunable lightweight polymer composites with dual-functional ability of efficient EMI shielding and heat dissipation. *Nanoscale*, 9(36), 13432-13440.
- [24] Shen, B., Li, Y., Yi, D., Zhai, W., Wei, X., & Zheng, W. (2017). Strong flexible polymer/graphene composite films with 3D saw-tooth folding for enhanced and tunable electromagnetic shielding. *Carbon*, 113, 55-62.
- [25] Wang, Y., Cheng, X. D., Song, W. L., Ma, C. J., Bian, X. M., & Chen, M. (2018). Hydro-sensitive sandwich structures for self-tunable smart electromagnetic shielding. *Chemical Engineering Journal*, 344, 342-352.
- [26] Chen, Z., Yi, D., Shen, B., Zhang, L., Ma, X., Pang, Y., ... & Zheng, W. (2018). Semi-transparent biomass-derived macroscopic carbon grids for efficient and tunable electromagnetic shielding. *Carbon*, 139, 271-278.
- [27] Dong, Y., Zhu, Y., Zhao, Y., Liu, F., Wang, E., & Fu, Y. (2017). Enhance interfacial properties of glass fiber/epoxy composites with environment-friendly water-based hybrid sizing agent. *Composites Part A: Applied Science and Manufacturing*, 102, 357-367.
- [28] Hu, J., Zhu, Y., Huang, H., & Lu, J. (2012). Recent advances in shape-memory polymers: Structure, mechanism, functionality, modeling and applications. *Progress in Polymer*

- Science, 37(12), 1720-1763.
- [29] Zhao, Q., Qi, H. J., & Xie, T. (2015). Recent progress in shape memory polymer: New behavior, enabling materials, and mechanistic understanding. *Progress in Polymer Science*, 49, 79-120.
- [30] Wang, E., Dong, Y., Islam, M. Z., Yu, L., Liu, F., Chen, S., ... & Hu, N. (2019). Effect of graphene oxide-carbon nanotube hybrid filler on the mechanical property and thermal response speed of shape memory epoxy composites. *Composites Science and Technology*, 169, 209-216.
- [31] Hager, M. D., Bode, S., Weber, C., & Schubert, U. S. (2015). Shape memory polymers: past, present and future developments. *Progress in Polymer Science*, 49, 3-33.
- [32] Sun, L., Huang, W. M., Ding, Z., Zhao, Y., Wang, C. C., Purnawali, H., & Tang, C. (2012). Stimulus-responsive shape memory materials: a review. *Materials & Design*, 33, 577-640.
- [33] Yao, Y., Zhou, T., Xu, Y., Liu, Y., & Leng, J. (2018). Preparation and characterization of shape memory composite foams based on solid foaming method. *Journal of Applied Polymer Science*, 135(46), 46767.
- [34] Jin, B., Song, H., Jiang, R., Song, J., Zhao, Q., & Xie, T. (2018). Programming a crystalline shape memory polymer network with thermo-and photo-reversible bonds toward a single-component soft robot. *Science advances*, 4(1), eaao3865.
- [35] Yan, Y., Xia, H., Qiu, Y., Xu, Z., & Ni, Q. Q. (2019). Multi-layer graphene oxide coated shape memory polyurethane for adjustable smart switches. *Composites Science and Technology*, 172, 108-116.
- [36] Huang, Y., Zhu, M., Pei, Z., Xue, Q., Huang, Y., & Zhi, C. (2016). A shape memory

- supercapacitor and its application in smart energy storage textiles. *Journal of Materials Chemistry A*, 4(4), 1290-1297.
- [37] Zarek, M., Mansour, N., Shapira, S., & Cohn, D. (2017). 4D Printing of Shape Memory - Based Personalized Endoluminal Medical Devices. *Macromolecular rapid communications*, 38(2), 1600628.
- [38] Wong, Y. S., Salvekar, A. V., Da Zhuang, K., Liu, H., Birch, W. R., Tay, K. H., ... & Venkatraman, S. S. (2016). Bioabsorbable radiopaque water-responsive shape memory embolization plug for temporary vascular occlusion. *Biomaterials*, 102, 98-106.
- [39] Zhao, W., Liu, L., Lan, X., Su, B., Leng, J., & Liu, Y. (2017). Adaptive repair device concept with shape memory polymer. *Smart Materials and Structures*, 26(2), 025027.
- [40] Wei, H., Zhang, Q., Yao, Y., Liu, L., Liu, Y., & Leng, J. (2016). Direct-write fabrication of 4D active shape-changing structures based on a shape memory polymer and its nanocomposite. *ACS applied materials & interfaces*, 9(1), 876-883.
- [41] Chen, H., Xia, H., Qiu, Y., & Ni, Q. Q. (2018). Analyzing effects of interfaces on recovery rates of shape memory composites from the perspective of molecular motions. *Composites Science and Technology*, 163, 105-115.
- [42] Chen, H., Xia, H., & Ni, Q. Q. (2018). Study on material performances of lead zirconate titanate/shape memory polyurethane composites combining shape memory and piezoelectric effect. *Composites Part A: Applied Science and Manufacturing*, 110, 183-189.
- [43] Choi, Y. K., Sugimoto, K. I., Song, S. M., Gotoh, Y., Ohkoshi, Y., & Endo, M. (2005). Mechanical and physical properties of epoxy composites reinforced by vapor grown carbon nanofibers. *Carbon*, 43(10), 2199-2208.

-
- [44] Al-Saleh, M. H., & Sundararaj, U. (2011). Review of the mechanical properties of carbon nanofiber/polymer composites. *Composites Part A: Applied Science and Manufacturing*, 42(12), 2126-2142.
- [45] Baji, A., Mai, Y. W., Wong, S. C., Abtahi, M., & Du, X. (2010). Mechanical behavior of self-assembled carbon nanotube reinforced nylon 6, 6 fibers. *Composites Science and Technology*, 70(9), 1401-1409.
- [46] Rahmanian, S., Suraya, A. R., Shazed, M. A., Zahari, R., & Zainudin, E. S. (2014). Mechanical characterization of epoxy composite with multiscale reinforcements: carbon nanotubes and short carbon fibers. *Materials & Design*, 60, 34-40.
- [47] Li, F., Scarpa, F., Lan, X., Liu, L., Liu, Y., & Leng, J. (2019). Bending shape recovery of unidirectional carbon fiber reinforced epoxy-based shape memory polymer composites. *Composites Part A: Applied Science and Manufacturing*, 116, 169-179.
- [48] Fejős, M., Romhány, G., & Karger-Kocsis, J. (2012). Shape memory characteristics of woven glass fibre fabric reinforced epoxy composite in flexure. *Journal of Reinforced Plastics and Composites*, 31(22), 1532-1537.
- [49] Fejős, M. (2013). Shape memory performance of asymmetrically reinforced epoxy/carbon fibre fabric composites in flexure. *eXPRESS Polymer Letters*, 7(6), 528-534.

Chapter 6

**Aligned nonwoven vapor grown carbon fiber
based polyurethane fibrous membrane for
direction-dependent microwave shielding**

6 Aligned nonwoven vapor grown carbon fiber based polyurethane fibrous membrane for direction-dependent microwave shielding

6.1 Introduction

Over past decades, many carbon based nano/micro-composites, such as graphene, carbon nanotube (CNT), carbon black (CB), porous carbon, have been broadly investigated for electromagnetic (EM) shielding due to their good electrical conductivity (σ), low density, high specific surface area, and unique one/two/three dimensional structures [1-4]. Among those, there are different forms of shielding composites including film [5], foam [6], textile [7], and nonwoven fabric [8]. However, it is noted that, almost all relevant research was so far focused on isotropic carbon composites.

Recently, with rapid development of advanced electronic devices, elimination of EM noise, remove of interferential EM wave, and precise filtration for desired EM wave turn more and more important particularly in radar detection, and signal analysis and identification fields [9-11]. This possibly promotes the development of anisotropic carbon composites, which have different properties with varying direction such as electrical conductivity and mechanical strength. Carbon nanofibre (CNF) is a one-dimensional (1D) cylindrical nanostructure with graphene layers arranged orderly along fibre direction, and has light weight, low cost, and good electrical conductivity [12, 13]. Its 1D structure makes it a good representative for fabrication of anisotropic composites [14-16].

In this chapter, we developed a novel rotation spinning approach based on DMF-H₂O exchange to fabricate unidirectional vapor grown carbon fibre (VGCF) based polyurethane (PU) fibrous membrane (VGCF@PUFM) for direction-dependent microwave shielding. This approach

could also apply to the fabrication of high content of carbon composite fibre. The obtained VGCF@PUFM showed obviously different electrical conductivity and mechanical strength in parallel and perpendicular directions. Changing microwave shielding effect was achieved by adjusting the rotation angle of VGCF@PUFM.

6.2 Experimental

6.2.1 Materials

Polyurethane (MM 6520, SMP Technologies Inc, Japan), Vapor grown carbon fiber (VGCF, Showa Denko K.K., Japan), *N,N*-dimethyl formamide (DMF, Wako Pure Chemical Industries, Ltd), DL water (Wako Pure Chemical Industries, Ltd), and all other reagents were used as received without further purification.

6.2.2 Fabrication of VGCF@PUFM

This unidirectional VGCF@PUFM was fabricated by rotation spinning in H₂O flow to form striped VGCF@PU fibre bundles, followed by assembly of which to be membrane, as illustrated in **Fig 6.1**. For details, 4.0 g VGCF (SOWA DENKO K.K., Japan) was added in 80 ml 0.2 g/ml PU (MS5520, SMP Technologies Inc, Japan) included DMF solution, and uniformly dispersed by magnetic stirring and sonication treatment. Then, the solution was injected in a pendular way onto a rotating plate at the injection rate of approximately 4.2 ml/min. The plate rotated at the speed of 200 rpm with the linear velocity at the injection spot being approximately 1.68 m/s. Flowing H₂O was used for immersion of unstable VGCF@PU fibres to avoid their fusion. After that, the obtained VGCF@PU fibre bundle was wrapped onto a tube and then spread flat by cutting. Finally, the VGCF@PUFM was obtained by hot pressing under mild conditions of 45 °C and 3.0 MPa for 1 h, and subsequent drying at 90 °C for 5 days.

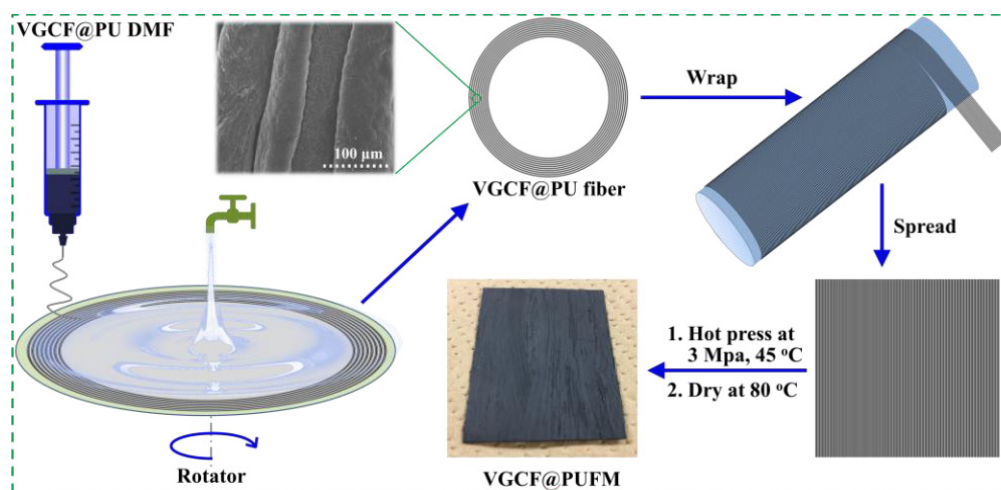


Fig. 6.1 Fabrication schematic of unidirectional VGCF@PUFM

6.2.3 Characterization

Chemical structures of VGCF and PU were characterized separately by roman spectrometer with 532 nm laser excitation (HoloLab series 5000, Kaiser Optical Systems), and Nicolet 5700 attenuated total reflection Fourier Transform Infrared (ATR-FTIR) instrument (Thermo Electron Corp., USA). Morphologies were observed by field emission scanning electron microscopy (FE-SEM, Hitachi S-5000, 20 kV). Electrical conductivity was measured by MCP-HT450 conductivity meter (Dia Instruments Co.) using standard four-probe method. The mechanical property was characterized by tensilon tensile tester (RTC1250A, A&D Co.) at a tensile speed of 1.0 mm/min. The samples for tensile testing all had dumb-bell shapes with the measurement part of the samples being 12.0 * 2.0 * 0.98 mm (length * width * thickness). Microwave shielding was evaluated in 4-16 GHz using transmission attenuation measurement system (KEYCOM Corp.), which connects with a vector network analyzer (37247D, Anritsu Co. Ltd.) for calculating shielding effectiveness (SE). Polarized wave with consistent vibration direction was used as incident EM wave source.

6.3 Results and discussion

6.3.1 Morphology and structure

The VGCF, having the diameter of ~ 150 nm and the length of a few microns, showed the presence of typical D and G feature peaks in roman spectrum (**Fig. 6.2a, 2c**). The PU (T_g : ~ 55 °C, T_m : ~ 175 °C) was obtained by polyaddition of linear chain diisocyanate and polyol. The amino (-NH-) and ketone (-CO-) groups in its feature structure, carbamate (-NH-CO-O-), were detected by FTIR, as shown in **Fig. 6.2b**. Due to short-range collection and high-speed drafting of rotation plate for ejected spinning solution (VGCF@PU DMF), the proposed approach, rotation spinning, could also apply to low-viscosity spinning and fabrication of high content of carbon composite fibre. The VGCF@PU fibres obtained by this approach exhibited the diameters mainly distributing within tens of microns (**Fig. 6.2d, 6.2e, 6.2g**). In **Fig. 6.2d-f**, lots of VGCFs randomly disperse inside the fibre, and are inter-connected by PU phase. Because of the flush and immersion of H₂O flow during spinning, no obvious fusion between fibres was observable. After hot pressing for VGCF@PUFM, the fibres revealed more compacted stacking (**Fig. 6.2g**). However, at the same time, some fusion between fibres happened to VGCF@PUFM. Also, more inter-connection of PU phase could be seen in **Fig. 6.2h**. These would enhance the mechanical strength of VGCF@PUFM both in parallel and perpendicular directions.

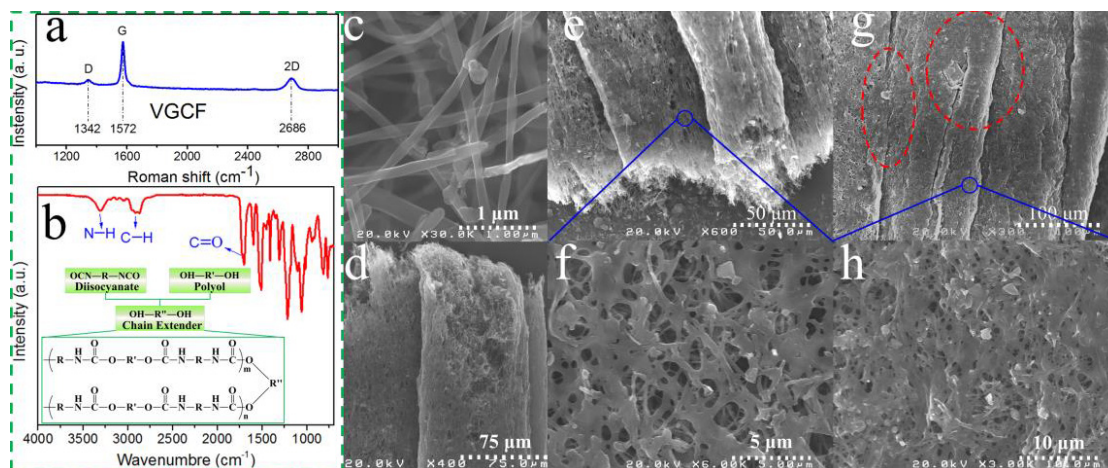


Fig. 6.2 (a, c) Roman spectrum and morphology of VGCF; (b) FTIR and chemical structure of PU; (d-f) internal and surface morphologies of VGCF@PU fibres; (g, h) surface morphologies of VGCF@PUFM.

6.3.2 Microwave shielding, conductive and mechanical properties

Microwave shielding of this unidirectional VGCF@PUFM with 0.98 mm thickness was evaluated by varying the rotation angles of internal aligned fibres with wave vibration direction (**Fig. 6.3a**). The result indicated this VGCF@PUFM showed decreasing shielding effectiveness (SE) in 4-16 GHz with aligned fibres gradually deviated from EM vibration direction (**Fig. 6.3b**). The VGCF@PUFM in parallel direction (0°) gave a maximal SE value mostly above 20 dB, namely, a shielding efficiency of 99%. While perpendicular (90°) to EM vibration direction, the SE decreased below 8 dB. This shielding difference was mainly attributed to different electrical conductivities (σ) in parallel and perpendicular directions. As shown in **Fig. 6.3c**, the electrical conductivity parallel to fibre direction reached 0.17 S/cm, ~ 3.4 times larger than that perpendicular to fibre direction. Besides, this VGCF@PUFM indicated obviously different mechanical strength in the two directions (**Fig. 6.3d**). After hot pressing, compacting and partial fusion between the fibres of the VGCF@PUFM made the strength perpendicular to fibre direction reach up to approximately 4.2 MPa. This has well guaranteed the integrity of the unidirectional VGCF@PUFM in spite of lower strength than that parallel to fibre direction.

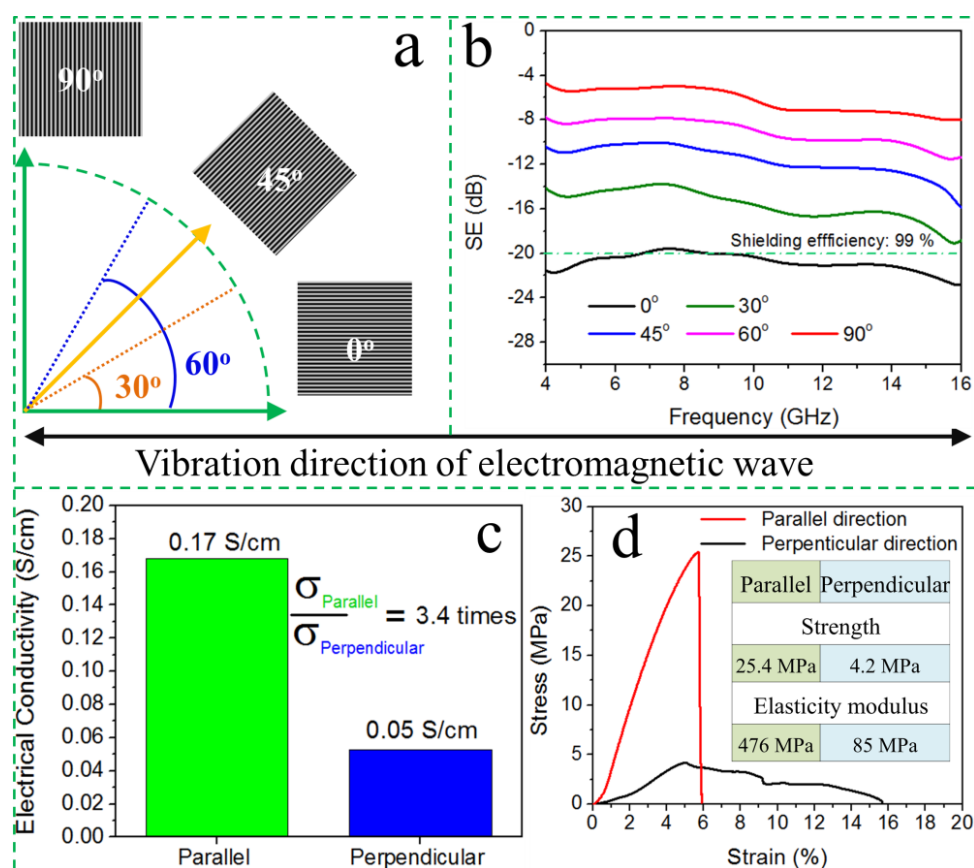


Fig. 6.3 (a) angular difference between alignment direction of VGCF@PU fibres and vibration direction of EM wave; (b) varying shielding effectiveness of VGCF@PUFMs with different angles; (c) electrical conductivity and (d) strain stress curves of parallel and perpendicular directions of VGCF@PUFMs.

6.3.3 Microwave shielding variation with different anisotropy

Shielding difference in parallel and perpendicular directions of VGCF@PUFMs was then investigated by different fusion extent of its internal fibres, which was achieved by adjusting hot-press temperatures from 120 °C to 200 °C at constant 3.0 MPa pressure. As hot-pressing temperature went up, the obtained VGCF@PUFMs showed an increased SE value both in parallel and perpendicular directions (**Fig. 6.4a**). This is due to improved electrical conductivity that the compacting of VGCF brought on. Moreover, shielding difference in parallel and perpendicular directions also increased with elevated temperature. It can be observed that, the shielding

difference at 10 GHz reduced from the 11.9 dB of initial status to the 0.5 dB after 200 °C hot-pressing. This great reduction was attributed to the gradual disappearance of anisotropy of the VGCF@PUFM. Under fixed pressure, increased temperature promoted the fusion between the fibres in the VGCF@PUFM, thus gradually transforming to isotropic membrane.

Therefore, for this VGCF@PUFM, greater shielding difference can be expected by further enhancing its anisotropy, namely, the difference of electrical conductivity in parallel and perpendicular directions. As demonstrated by carbon fibre reinforced polymer (CFRP), the electrical conductivity in parallel and perpendicular directions showed a big difference of ~ 11.8 times (**Fig. 6.4b, 6.4c**). This difference led to a great shielding difference exceeding 20 dB (>25 dB, < 2.5 dB) in 0° and 90° , as presented in **Fig. 6.4d**. In addition, more obvious anisotropy for this VGCF@PUFM can also be expected by fabricating oriented VGCF array inside fibre. This structure of array is predictable for improving electrical conductivity of VGCF@PU fibre and enhancing the anisotropy of VGCF@PUFM. As presented in **Fig. 6.4e-g**, appropriate drafting during spinning, to some extent, achieved ordered arrangement of VGCF in fibre direction. However, for fabrication of highly oriented VGCF array, further research is required.

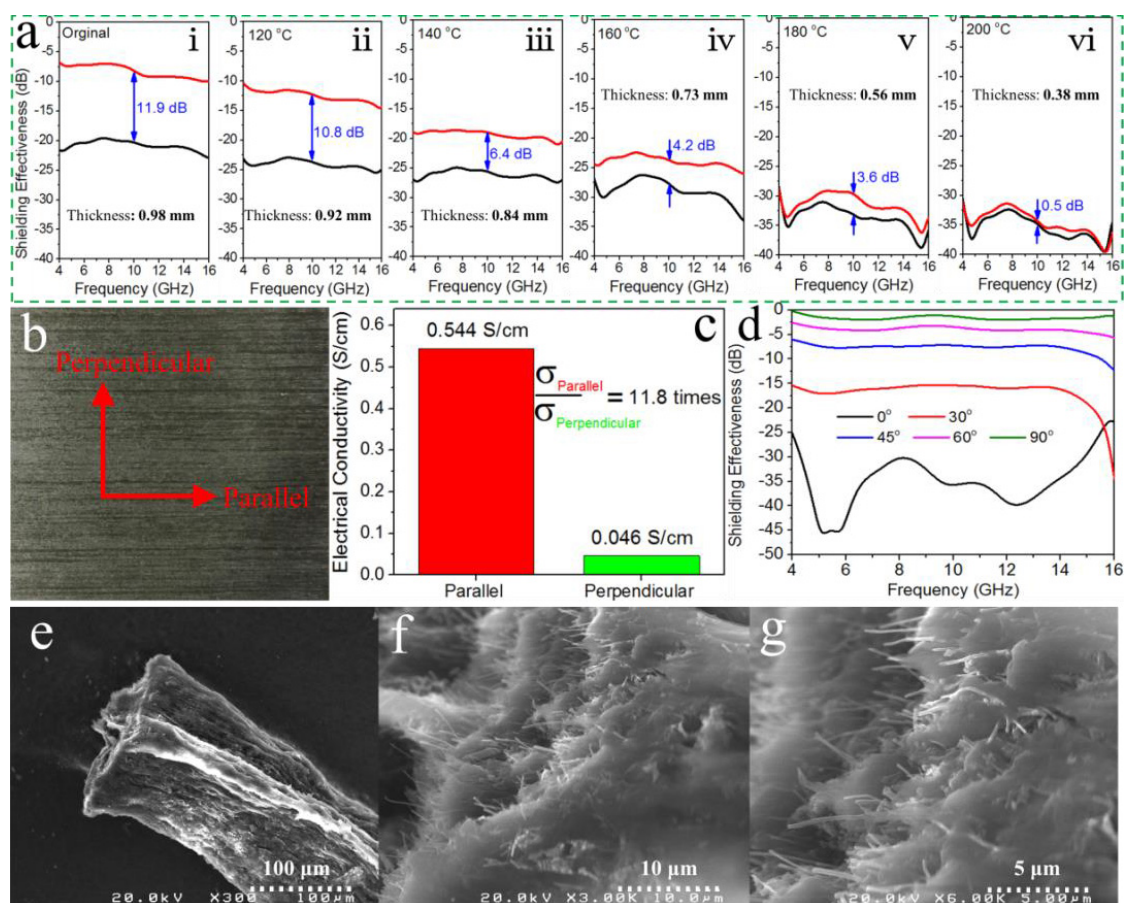


Fig. 6.4 (a) shielding effectiveness of parallel and perpendicular directions of VGCF@PUFM after hot pressing under different temperature at 3.0 MPa; (b) surface of CFRP; (c) electrical conductivities of parallel and perpendicular directions of CFRP; (d) varying shielding effectiveness of CFRP with different angles; (e-g) oriented VGCF arrangement in PU fibre.

6.4 Conclusions

In conclusion, unidirectional VGCF@PUFM was fabricated by rotation spinning in flowing water for directional microwave shielding. This VGCF@PUFM showed obvious anisotropy both in electrical conductivity and mechanical strength. Different microwave shielding effect was observed by changing the rotation angle of the VGCF@PUFM with electromagnetic vibrational direction. There is a shielding difference over 10 dB between 0° and 90°. Larger shielding difference can be achieved by increasing the difference of electrical conductivity of parallel and

perpendicular directions. This VGCF@PUFM is expected to be applied in removing interferential, and filtrating desired EM wave.

References

- [1] Y. Wu, Z. Wang, X. Liu, X. Shen, Q. Zheng, et al., *ACS Appl. Mater. Interface* 9 (2017) 9059-9069.
- [2] B. Shen, Y. Li, D. Yi, W. Zhai, X. Wei, W. Zheng, *Carbon* 113 (2017) 55-62.
- [3] Z. Zeng, C. Wang, Y. Zhang, P. Wang, et al., *ACS Appl. Mater. Interface* 10 (2018) 8205-8213.
- [4] Y.J. Wan, P.L. Zhu, S.H. Yu, R. Sun, C.P. Wong, W.H. Liao, *Carbon* 115 (2017) 629-639.
- [5] S.H. Lee, D. Kang, I.K. Oh, *Carbon* 111 (2017) 248-257. [6]
- [6] Y. Sun, S. Luo, H. Sun, W. Zeng, C. Ling, D. Chen, et al., *Carbon* 136 (2018) 299-308.
- [7] S. Ghosh, S. Remanan, S. Mondal, S. Ganguly, P. Das, et al., *Chem. Eng. J.* 344 (2018) 138-154.
- [8] L. Lu, D. Xing, K.S. Teh, H. Liu, Y. Xie, X. Liu, et al., *Mater. Design* 120 (2017) 354-362.
- [9] Y. Song, S. Liu, E. Solodovnik, K.J. Karimi, U.S. Patent No. 15/605, 649, 2017.
- [10] T.L. Wu, C.Y. Hsiao, C.H. Hung, U.S. Patent No. U.S. Patent No. 9,655,230, 2017.
- [11] S.E.O. Minah, S. Lee, W.O.O. Deokha, J. Kim, T. Lee, et al., U.S. Patent No. 15/808,066, 2018.
- [12] S.C. Li, B.C. Hu, Y.W. Ding, H.W. Liang, C. Li, et al., *Angew. Chem.* 130 (2018) 7203-7208.
- [13] M.H. Al-Saleh, U. Sundararaj, *Carbon* 47 (2009) 2-22.
- [14] H. Ko, Z. Zhang, J.C. Ho, K. Takei, R. Kapadia, Y.L. Chueh, *Small* 6 (2010) 22-26.
- [15] T. Prasse, J.Y. Cavaille, W. Bauhofer, *Compos. Sci. Technol.* 63 (2003) 1835-1841.
- [16] G.G. Tibbetts, M.L. Lake, K.L. Strong, B.P. Rice, *Compos. Sci. Technol.* 67 (2007) 1709-1718.

Chapter 7

Conclusions

7 Conclusions

This dissertation focused on the structural fabrication of various micro/nano-carbon based functional electromagnetic shielding composites in which there are mainly foamy, gradient, and unidirectional structures. Electromagnetic shielding ability could be adjusted by varying thickness. Shape memory effect was mainly utilized for driving in thickness variation of those functional shielding composites. These functional shielding composites include thickness-adjustable graphite micro-flakes@SMPU sponge (G@SMPU), vapor grown carbon fiber (VGCF) based polyurethane foam (VGCF@PUF), gradient VGCF based shape memory polyurethane foam (VGCF@SMPUF), and unidirectional nonwoven VGCF based polyurethane fibrous membrane (VGCF@PUFM).

In chapter 1, general introduction of conventional electromagnetic shielding materials and interesting shape memory materials were presented. The advantages of carbon nanomaterials in electromagnetic shielding field were expected. Aiming to the advent of advanced electromagnetic devices, carbon nanomaterials based structure design are considered to be promising in fabricating varieties of smart electromagnetic shielding materials.

In chapter 2, shape memory polyurethane (SMPU) coated with multi-layer graphene oxide (MLGO@SMPU) was fabricated by multiple dipping in GO aqueous solution for adjustable shape memory switch. The actuation effect of SMPU was investigated by adjusting graphene oxide layer. Morphology observation showed that multi-layer graphene oxide was evenly covered onto the surface of the SMPU substrate. Strain stress curves indicated that the increase of GO layers improved the mechanical strength of these MLGO@SMPU composites in the initial stretching stage. Water resistance testing suggested that the MLGO@SMPU could maintain integrity in water within 24 h, but the GO layer would fall off after being subjected to sonication treatment.

Adhesive force testing showed that the first GO layer attached well onto the SMPU surface. However, more GO layers were more easily peeled off from the SMPU substrate. This was attributed to weak intermolecular forces between GO layers. Finally, the shape memory performances for these MLGO@SMPU composites were evaluated using homemade evaluation apparatus. It was concluded that with the increase of GO layers, the MLGO@SMPU showed a decreased angle recovery ratio, slower recovery time, larger recovery force, and decreased angle fixity ratio. It is expected that this novel approach of dipping coating of shape memory materials for adjustable recovery ratio, time, and force, could be applied in the field of smart switching devices.

In chapter 3, we fabricated a novel shape memory-driving thickness-adjustable graphite (G) micro-flakes@shape memory polyurethane (G@SMPU) foam by two-step dipping for microwave shielding. Dipping coating of SMPU onto the G filled sponge gave a good shape memory recovery effect above 90 %. G-9@SMPU and G-18@SMPU sponges achieved the shielding percentages more than 99.0 % and 99.9 %, respectively. Moreover, the shielding of this G@SMPU sponge would not weaken obviously when varying thickness or increasing compression time. This indicates the steady distribution and adhesion of G inside the sponge due to the fixing of SMPU.

In chapter 4, A H₂O-DMF solvent exchange approach was developed for preparation of nano/micro composite foam. By this approach, vapor grown carbon fiber based polyurethane foam (VGCF@PUF) was fabricated for compression-adjusted microwave shielding. The results showed that the hot compression under 120 °C for VGCF@PUF made discrete PUF stripes, which formed due to the presence of VGCF, fuse together. Therefore, the mechanical performance of the VGCF@PUF was improved, such as the strength and elongation. At the same time, the hot

compression drastically enhanced the electrical conductivity for orders of magnitude. For microwave shielding, in the frequency range from 0.5 GHz to 18 GHz, hot-compressing the VGCF@PUF from original 1.96 mm to 0.45 mm made the shielding effectiveness increase from 10-15 dB to be above 35 dB. This suggests that the structure optimization of carbon filled shielding materials, such as the compacting approach in this research, could promote effective electrical inter-connection of carbon fillers, and thus achieve high-performance microwave shielding.

In chapter 5, by using abovementioned H₂O-DMF solvent exchange approach, gradient vapor grown carbon fiber-based shape memory polyurethane foam (VGCF@SMPUF) was fabricated by alternative dipping in a VGCF containing SMPU/DMF solution of decreasing concentration and distilled water to form shape memory driven adjustable microwave shielding. Different electrical conductivities and VGCF contents on two sides of this gradient VGCF@SMPUF were obtained. The adjustability of the shielding effectiveness was achieved by different degrees of angle recovery. Hot compression could not only decrease the recovery time, and gave a higher recovery ratio, but also clearly improve the shielding performance of this gradient VGCF@SMPUF. Moreover, the VGCF@SMPUF recovery from the side with a higher VGCF content exhibited a faster recovery time and higher recovery ratio than that recovering from the side with a lower VGCF content owing to different mechanical strengths at either side.

In chapter 6, unidirectional VGCF based polyurethane fibrous membrane (VGCF@PUFM) was fabricated by rotation spinning in flowing water for directional microwave shielding. This VGCF@PUFM showed obvious anisotropy both in electrical conductivity and mechanical strength. Different microwave shielding effect was observed by changing the rotation angle of the

VGCF@PUFM with electromagnetic vibrational direction. There is a shielding difference over 10 dB between 0° and 90° . Larger shielding difference can be achieved by increasing the difference of electrical conductivity of parallel and perpendicular directions. This VGCF@PUFM is expected to be applied in removing interferences, and filtering desired EM waves.

In conclusion, three types of carbon based composite structures, foam structure, gradient structure, and anisotropic structure were successfully designed by using graphite micro-flakes or VGCF as fillers, and SMPU as filling matrix. Shape memory effect played the role of thickness fixing and bending actuation. By varying thickness or angles, the composites showed adjustable EM shielding in the decibel range of 0-40 dB. These functional EM shielding composites with unique structures opened up a new insight for development of smart EM shielding devices.

Accomplishments

Journal Publications

- (1) **Yongjie Yan**, Hong Xia, Yiping Qiu, Zhenzhen Xu, Qing-Qing Ni*. Multi-layer graphene oxide coated shape memory polyurethane for adjustable smart switches. *Composites Science and Technology*, 2019, 172, 108-116.
- (2) **Yongjie Yan**, Hong Xia, Yiping Qiu, Zhenzhen Xu, Qing-Qing Ni*. Highly aligned nonwoven vapor grown carbon fibre based polyurethane fibrous membrane for direction-dependent microwave shielding. *Materials Letters*, 2019, 245, 98-102.
- (3) **Yongjie Yan**, Hong Xia, Yiping Qiu, Zhenzhen Xu, Qing-Qing Ni*. Shape memory driving thickness-adjustable G@SMPU sponge with ultrahigh carbon loading ratio for excellent microwave shielding performance. *Materials Letters*, 2019, 236, 116-119.
- (4) **Yongjie Yan**, Hong Xia, Yiping Qiu, Zhenzhen Xu, Qing-Qing Ni*. Fabrication of gradient vapor grown carbon fiber based polyurethane foam for shape memory driven microwave shielding. *RSC Advances*, 2019, 9, 9401-9409.

Academic Conferences

- (1) **Yongjie Yan**, and Qing-Qing Ni. Development of carbon nanofiber nanocomposites and their application for electromagnetic wave shielding, Japan Society for Composites Materials (JCCM-10), Nihon University (Tokyo), 2019, Mar, 6-8.
- (2) **Yongjie Yan**, and Qing-Qing Ni. Fabrication of BaTiO₃ nanoparticles with different nanosizes by hydrothermal synthesis for microwave absorption. *World Engineering and Applied Sciences Community*, Athens, Greece, 2019, Feb, 23-24.

-
- (3) **Yongjie Yan**, and Qing-Qing Ni. Embedding of shape memory function in porous materials. 2019 3rd European Conference on Materials, Mechatronics and Manufacturing (ECMMM 2019), Amsterdam, Netherlands 2019, Feb, 16-18.
 - (4) **Yongjie Yan**, and Qing-Qing Ni. A novel carbon@shape memory foam for high-performance electromagnetic shielding. 7th International Conference on Nano and Materials Science (ICNMS 2019), San Francisco, USA, 2019, Jan, 4-7.
 - (5) **Yongjie Yan**, and Qing-Qing Ni. Development of Co@PANI@PU nanocomposites and their application in microwave absorption, Japan Society for Composites Materials (JCCM-9), Nihon University (Tokyo), Doshisha University (Kyoto), 2018, Feb, 28-Mar, 2.
 - (6) **Yongjie Yan**, and Qing-Qing Ni. Preparation of BTO@GO@PU composite membrane and its application in microwave absorption field. 2017 2nd International Conference on Frontiers of Composite Materials (ICFCM 2017), Melbourne, Australia, 2017, Nov, 15-17.
 - (7) **Yongjie Yan**, and Qing-Qing Ni. Development of graphene in functional composite field. Workshop of Advanced Composites (WAC 2017), Ueda, Japan, 2017, Nov, 10-12. (Poster presentation).
 - (8) **Yongjie Yan**, Juhong Yu, Hisaaki Morikawa, and Qingqing Ni. Development of Ag@BaSO₄@BTO@PANI nanocomposites and their application in microwave absorption. Japan Society for Composites Materials (JCCM-8), Tokyo University, 2017, Mar, 16-18.
 - (9) **Yongjie Yan**, and Qingqing Ni. Preparation and characteristics of BTO@GO@PU composite membrane for electromagnetic radiation absorption. The 4th International Symposium on Advanced Textile Science and Technology, Hangzhou, China, 2016, Oct, 12-15. (Poster presentation).

- (10) **Yongjie Yan**, Kyoubi Horiki, and Qingqing Ni. Electrospinning preparation of oxidized GO/PUF for electromagnetic wave shielding. The 8th International Symposium on High-Tech Fiber Engineering for Young Researcher, Seoul National University, Korea, 2016, Sep. 25-Oct. 02

Acknowledgements

Most importantly, I would like to express my sincere gratitude to my advisor, Prof. Ni Qing-Qing, for his countless guidance and support on both research and living aspects in Japan over past five years. Without his support, I wouldn't have the opportunity to come to Japan as a Japanese Government Scholarship student for overseas study and research. His countless explanation made me know the way how to think of research. His skillful guidance made me know how to be a qualified and charming researcher. His smartness on guiding and teaching students made me realize there is still a long way to be a good research guider. At the same time, I also want to thanks him for his support and allowance on my research activities such as study abroad, international conferences, and Japanese life. Without him, for sure I couldn't have such fulfilling student life. Words can't express my appreciation to his support on all aspects.

Then, I want to thanks the Ministry of Education, Culture, Sports, Science and Technology (MEXT) for providing me Japanese Government Scholarship. With this, I didn't have to do part time job and could have a steady research life. Also, I more want to thanks Shinshu University for providing me Chinomori Special Scholarship as well as the exemption of all tuition fees during doctoral period. Moreover, Shinshu University also provided lots of opportunities for applying funding support for domestic and international conference, overseas study exchange, and modification and publication fees of academic papers. With these opportunities, I could have a fulfilling life during past five years. Herein, I would like to specially thank administrative staff of Shinshu University Sano Sumika for her lots of assistance on those applications.

Also, I want to express my deep thanks to researcher Xia Hong for her patient guidance and support on my research. She always shows her best to provide some help even when she is busy

with something.

Meanwhile, lots of thanks are also given to Nisida technician, Nakamura technician, and Antatsu technician for their patient teaching in using varieties of characterization equipments.

Besides, I want to thanks all research members in this research group mainly including Hairong Chen, Xiaoyu Guan, Holibe, Jun Hong, Xiaojuan Li, Chongchao Li, Yajun Liu, Ji Hun, Lina Cui, Canyi Huang, Yinan Liu, and Si Chen. Thanks for their assistance and information provision. I also want to thanks those who helped me, played with me and think of me as a friend. They made me feel warm in heart over this long-term research career.

At last, I want to express my deepest appreciation and love to my parents and girlfriend. My parents are always my strong support whenever I suffered from body or spiritual problems. They respect my decision and always back me up. My girlfriend made me feel not lonely and created lots of fun. She gave me lots of spiritual support on my everyday life. Thanks them, they are my rock sticking to now and striving on for future. They are always my most important persons during my whole my life.

Thank you

Yan Yongjie